Flow-Through Membrane Microreactor for Intensified Heterogeneous Catalysis

Von der Fakultät für Maschinenwesen der
Rheinisch-Westfälischen Technischen Hochschule Aachen
zur Erlangung des akademischen Grades eines Doktors der
Ingenieurwissenschaften genehmigte Dissertation

vorgelegt von
Thomas Westermann
aus
Issum, Deutschland

Berichter:

Univ.-Prof. Dr.-Ing. Thomas Melin
Univ.-Prof. Dr.rer.nat. Marcel Liauw

Tag der mündlichen Prüfung: 10. Februar 2009

Diese Dissertation ist auf den Internetseiten der
Hochschulbibliothek online verfügbar.

Danksagung

Die vorliegende Arbeit ist während meiner Zeit als wissenschaftlicher Mitarbeiter der Aachener Verfahrenstechnik entstanden. Ich möchte diese Gelegenheit nutzen, mich nicht nur bei den Menschen zu bedanken, die direkt zum Gelingen der Dissertation beigetragen haben, sondern auch bei den vielen anderen, durch die der Lebensabschnitt in Aachen für mich zu etwas Besonderem wurde.

Zuallererst danke ich meinem Doktorvater Professor Thomas Melin für sein reges Interesse, seine zahlreichen Einfälle und das große Vertrauen, das er seinen Mitarbeitern entgegenbringt. Ich danke Professor Marcel Liauw für die bereitwillige Übernahme des Koreferats und die langjährige gute Zusammenarbeit, sowie dem Prüfungsvorsitzenden Professor Wolfgang Marquardt und dem Beisitzer Professor Reinhold Kneer.

Ein besonders großes Dankeschön an die vielen Studenten, die bei der Untersuchung des Membranmikroreaktors als Studien-, Diplom- und Masterarbeiter sowie als HiWis durch ihre Motivation und Initiative immer wieder für frische Ideen und neuen Schwung gesorgt haben. Im Einzelnen sind das in chronologischer Reihenfolge Christiana Weber, Can Aran, Arthur Refinius, Shweta Holani, Luis Tsuchida, Fee Pitsch, Nicole Kopriwa, Carsten Hufnagel, Alexander Schröder, Eva Kretzschmar und Ying Yuan.

Durch das Anfertigen von Bauteilen und Analysen aktiv zum Erfolg beigetragen haben Werkstatt, Elektrowerkstatt und Labor der AVT sowie weitere Institutionen der RWTH Aachen (GFE, IME, IBAC, TCHK), deren unkomplizierte Zusammenarbeit ich an dieser Stelle besonders hervorheben möchte.

Meinen Kollegen der Aachener Verfahrenstechnik danke ich für zahlreiche Diskussionen, viele gemeinsame Unternehmungen und die schöne Zeit. Für die kritische und konstruktive Durchsicht des Manuskripts danke ich insbesondere Florian Krull.

Für alles andere danke ich meiner Familie und meiner Frau Kira, in der Hoffnung, sie würden auch ohne spezielle Nennung wissen, wie viel sie mir bedeuten.

Abstract

Under the common headline of process intensification several innovative reactor types for heterogeneous catalysis are discussed, including membrane reactors, microreactors and monolithic reactors. A novel reactor concept called flow-through catalytic membrane microchannel reactor contains aspects of each of the three reactor types: The catalyst is immobilized in a ceramic membrane, the geometric structures are in the scale of micrometers and below and the reactants flow convectively through uniform catalytic channels.

Anodized alumina membranes comprise regular cylindrical channels with a narrow pore size distribution. Impregnated with palladium, they promise high catalytic activity combined with very short contact times and a narrow residence time distribution, calling for application in performing fast and selective reactions.

Whereas the reactor geometry impedes direct measurement of the residence time distribution, a fluid dynamic reactor model, taking into account pore size distribution and axial dispersion, allows to quantify deviations from ideal plug flow behavior. Both influences are combined in a single parameter effective dispersion model. For low axial dispersion caused by high axial velocities and absolute pressures, the pore size distribution limits the minimum achievable effective dispersion.

Due to the small characteristic lengths, heat convection is always small compared to the internal heat transfer, leading to isothermal reactor behavior with identical gas phase and membrane temperature and a temperature jump at the pore entrance. The isothermal operation even of highly exothermic reactions is beneficial for kinetic studies.

The predicted high catalytic activity of the investigated catalytic membrane microchannel reactor compared to catalytic fixed beds is proven experimentally. Although the flat and thin geometry of membranes is advantageous in terms of high throughput at minimum contact time, it is unfavorable regarding axial dispersion. This prevents application in consecutive low pressure gas phase reactions, where a fixed bed reactor might reach higher selectivities due to increased reactor length. At high pressures or in liquid phase this limitation is negligible and ideal reactor behavior can be assumed.

Keywords:
membrane, microstrucure, catalyst support, reaction engineering

Zusammenfassung

Das Schlagwort Prozessintensivierung umfasst zahlreiche innovative Reaktortypen für heterogen katalysierte Reaktionen, wie z.B. Membranreaktoren, Mikroreaktoren und Monolithreaktoren. Der vorgestellte durchströmte katalytische Membranmikrokanalreaktor vereint Aspekte dieser drei Reaktortypen: Die Reaktanden strömen konvektiv durch die gleichförmigen katalytischen Kanäle einer keramischen Membran, deren Abmessungen im Bereich von Mikrometern und darunter liegen.

Anodisierte Aluminiumoxidmembranen verfügen über gleichmäßige zylindrische Mikrokanäle mit sehr enger Porengrößenverteilung. Durch Einbringen von Palladium in die Membranporen entsteht ein Reaktor mit hoher katalytischer Aktivität, kombiniert mit extrem kurzen Kontaktzeiten und einer engen Verweilzeitverteilung.

Eine direkte Messung der Verweilzeitverteilung ist aufgrund der Reaktorgeometrie nicht möglich, Abweichungen vom idealen Reaktorverhalten lassen sich aber mit Hilfe eines effektiven Dispersionsmodells quantifizieren, welches die Einflüsse von Porengrößenverteilung und axialer Dispersion in einem einzelnen Parameter berücksichtigt. Im Falle geringer axialer Dispersion, beispielsweise durch hohe Durchströmungsgeschwindigkeiten und Drücke, begrenzt die Porengrößenverteilung die minimal erreichbare effektive Dispersion.

Aufgrund der geringen Reaktordimensionen ist in den Membranporen Konvektion immer klein gegenüber innerem Wärmeübergang zwischen Gas und Wand. Dies führt zu isothermem Reaktorverhalten mit identischer Gas- und Membrantemperatur selbst bei stark exothermen Reaktionen und einem Temperatursprung am Reaktoreingang.

Reaktionsversuche bestätigen die hohe katalytische Aktivität des Membranmikrokanalreaktors verglichen mit einem katalytischen Festbett. Während die flache und dünne Membrangeometrie hohe Durchsätze bei minimaler Kontaktzeit ermöglicht, erweist sie sich als nachteilig bezüglich axialer Dispersion und verhindert einen Einsatz für selektive Folgereaktionen bei niedrigen Drücken. Bei hohen Drücken und in der Flüssigphase gilt diese Einschränkung nicht und das Reaktorverhalten kann als ideal bezeichnet werden.

Schlagwörter:
Membran, Mikrostruktur, Katalysatorsupport, Reaktionstechnik

Contents

1 Introduction **1**

2 Process Intensification Reactors **3**
2.1 Microreactors 5
2.2 Membrane Reactors 7
2.2.1 Extractor Membrane Reactors 11
2.2.2 Distributor Membrane Reactors 13
2.2.3 Contactor Membrane Reactors 15
2.3 Flow-Through Catalytic Membrane Reactors 18
2.3.1 Complete Conversion Integral FTCMR 20
2.3.2 Selective Integral FTCMR 24
2.3.3 Selective Differential FTCMR 36
2.4 Conclusions 41

3 Experiments and Methods **45**
3.1 Ceramic Membrane Microstructures 45
3.1.1 Microstructure Generation 46
3.1.2 Microstructure Characterization Methods 48
3.1.3 Results 51
3.2 Catalytic Activation 56
3.2.1 Catalyst Deposition on Ceramic Supports 57
3.2.2 Characterization of Catalyst Loading 61
3.2.3 Results 64
3.3 Reaction Experiments 69
3.3.1 Model Reactions 69
3.3.2 Reactor Module and Membrane Configurations 72
3.3.3 Test Rig and Analytics 74
3.3.4 Catalyst Loading and Catalytic Activity 77
3.4 Conclusions 79

4 Reactor Fluid Dynamics **81**
4.1 Residence Time Distribution 81
4.1.1 Pore Size Distribution and Plug Flow 83
4.1.2 Isoporous Membrane with Dispersion 87
4.1.3 Combined Pore Size Distribution and Axial Dispersion 91
4.2 Pressure Drop and Microeffects 97
4.2.1 Flow Regimes in Microchannels 97
4.2.2 Pressure Drop in Catalytic Membrane Reactors 99
4.2.3 Dispersion in Transition Regime 103
4.3 Conclusions 106

5 Reactor Performance **109**
5.1 Reaction Kinetics 109
5.1.1 Ethene Hydrogenation 110
5.1.2 Ethyne Hydrogenation 113
5.2 Heat Transfer in Catalytic Membrane 117
5.2.1 Isoporous PFTR Model with Heat Transfer 118
5.2.2 Parameter Study for Heat Transfer Model 124
5.2.3 Experimental Validation 133
5.3 Reaction Selectivity 135
5.3.1 Isothermal Reactor with Effective Dispersion 136
5.3.2 Parameter Study 138
5.3.3 Experimental Validation 140
5.4 Impact of Catalytic Microstructure 142
5.5 Conclusions 145

6 Conclusions **149**

Bibliography **155**

Symbols and Abbreviations **169**

Curriculum Vitae **173**

Chapter 1

Introduction

Heterogeneous catalysis is one of the central topics in reaction engineering. About 80 % of chemical products in the world market are manufactured via heterogeneous catalytic processes (Stankiewicz, 2001). Most common reactors for catalyzed gas and liquid reactions contain the catalyst in form of particles of diverse shapes and sizes, either in a fixed or moving bed. The well known drawbacks of fixed bed reactors include mass and heat transfer limitations, low specific surface area and high pressure drops. For moving bed or slurry reactors, catalyst attrition, equipment erosion and catalyst separation are of major concern.

Under the common headline of "process intensification" several innovative concepts to overcome the known limitations are under discussion, including membrane reactors, microreactors and monolithic reactors. The reactor concept discussed in the work at hand, called "flow-through catalytic membrane microchannel reactor" contains aspects of each of the three reactor types: As the catalyst is immobilized in a ceramic membrane, it can be included in the category of membrane reactors. The geometric structures are in the scale of micrometers and even below, thus it can be considered a microreactor. Finally the reactants flow convectively through uniform catalytic channels, which is the main characteristic of monolithic reactors.

The applied catalytic microstructure is made up of anodized alumina membranes, which comprise regular cylindrical channels with a narrow pore

size distribution. The motivation of my investigations is to improve the knowledge of the micro-scale processes inside the catalytic membrane and to assess experimentally and theoretically in which cases the application of these regularly structured membranes as catalytic membrane reactors is beneficial compared to other reactor concepts. The anticipated advantages of the reactor concept are high catalytic activity, very short contact times and a narrow residence time distribution, calling for application in performing fast and selective reactions, such as gas phase hydrogenations of alkenes and alkynes.

In contrast to fixed bed reactors or macroscopic monolithic reactors, in flow-through catalytic membrane reactors diffusion limitation decreases for higher flow-through velocities. Compared with unstructured membrane reactors, the structured membrane promises reduced pressure drop due to minimum tortuosity and improved pore size distribution without pinholes.

After classifying the reactor concept within the families of process intensification, microreactors and membrane reactors and an extensive review on FTCMR (Chapter 2), the experimental part will be elucidated, including preparation and characterization of the catalytic membranes, as well as the setup of reactor module and analytics (Chapter 3). The reactor fluid dynamics will be analyzed in Chapter 4, generating correlations for pressure drop and residence time distribution, in order to determine optimum operating conditions. Special attention will be paid to microeffects such as Knudsen and molecular diffusion, which affect macroscopic parameters like pressure drop and dispersion. A reactor model will be developed, allowing for assessment of conversion, selectivity and temperature profiles (Chapter 5), taking into account axial dispersion, heat transfer and pore size distribution. The models are validated experimentally using ethyne and ethene hydrogenation catalyzed by palladium as model reactions. The reactor performance of structured membranes is experimentally compared to that of unstructured membranes and of equivalent catalytic fixed beds.

Chapter 2

Process Intensification Reactors

Process intensification (PI) is a very general term that calls for further definition. Ramshaw (1999) dates the origin of the concept back to the late 1970s and describes PI as a strategy of dramatically reducing the plant size (100-1000 fold) in order to meet a given production objective. Stankiewicz and Moulijn (2000) broaden the field of PI by including the development of novel innovative apparatuses and techniques that are expected to bring substantial improvements in manufacturing and processing compared to those commonly used today. According to this definition PI is not limited to decreasing the ratio between equipment size and production capacity, but also includes the reduction of energy consumption or waste production ultimately resulting in cheaper, sustainable technologies. The provocative number of 100 fold decrease is replaced by the factor 2. DECHEMA (2006) uses a somewhat different understanding of PI: It contains several different methods aimed at drastically increasing the economic and ecological efficiency of chemical processes and the generation of novel products and product qualities based on an in-depth knowledge of the process steps and the interdisciplinary application of effects on nano-, micro- and macroscale.

A further classification and a few examples might clarify, what is commonly understood as PI: Process-intensifying equipment includes several novel reactors and devices, whereas process-intensifying methods and techniques form a separate category, although the differentiation is sometimes

diffuse. Several concepts are currently discussed:

- Novel reactors as well as intensive mixing, heat-transfer and mass-transfer devices (static mixers, monolithic catalysts, microreactors, rotating devices),
- Integration of reaction and one or more unit operations (separation, heat exchange, or phase transition) into so-called multifunctional reactors (reverse-flow reactor, reactive distillation, membrane reactors, reactive extrusion, fuel cells),
- Development of new or hybrid separations (membrane absorption and stripping, membrane distillation, adsorptive distillation),
- Use of alternative forms and sources of energy for processing (centrifugal fields, ultrasound, solar energy, microwaves, electric fields, gliding arc),
- New process-control methods (like intentional unsteady-state operation).

The motivation for developing and applying process intensifying equipment and methods is finally not only given by the prospect of dramatic cost reductions, but also by increasing the sustainability of chemical production (Stankiewicz and Moulijn, 2000).

The reactor concept investigated in the work at hand is called flow-through catalytic membrane reactor. It can be regarded a part of the process intensification family, closely related to microreactors and monolithic catalysts and of course it is a certain kind of membrane reactor. A clear explanation of the concept and potential benefits of microchannel membrane reactors requires an outline of the similarities and differences to the other named reactor concepts. To begin with, the general concepts of both microreactors and membrane reactors are explained, before giving a comprehensive review on current research results in the field of flow-through catalytic membrane reactors.

2.1 Microreactors

Microreactors are usually defined as miniaturized reaction systems fabricated by applying, at least partially, methods of microtechnology and precision engineering. The characteristic dimensions of the internal structures of microreactors, like fluid channels, typically range from the sub-micrometer to the sub-millimeter scale (Ehrfeld et al., 2000). The increase of specific properties, such as the surface to volume ratio, is a direct consequence of reducing the characteristic dimensions. The second potential benefit is given by the reduced total size of the system. Resulting characteristics of microreactors are:

- Virtually always laminar flow pattern,
- High heat transfer rates, allowing for isothermal or periodic operation,
- Improved mass transport due to fast diffusive mixing,
- Inherently safe operation of potentially dangerous reactions,
- Exact reaction control due to narrow residence time distributions,
- High pressure stability,
- Reduced time-to-market by numbering up instead of scale up.

The given characteristics are responsible for observed higher conversions and selectivities in micro-structured reactors in comparison to conventional ones. Advantages can especially be expected for fast, highly exothermic or endothermic reactions (Wörz et al., 2001). The reaction times are shorter as compared to conventional reactors allowing for less degradation and side products (Gokhale et al., 2005). The small hold-up in the microstructures significantly reduces the hazard of highly exothermic and explosive reactions.

Microreactor types can be distinguished by their main function, which can be improved heat exchange, mixing or catalyst support. Potential benefits are pure products, increased yields, reduced resource consumption and innovative process management.

Several materials and microstructuring methods are applied to produce microreactors. Materials range from metals to plastics, ceramics, glasses and

silicon. Production processes include machining, spark erosion, laser processes, lithography and etching methods. Surface treatment methods such as coating, surface increase or catalyst insertion are often applied. Standardized modular concepts with compact overall dimensions are available. Due to their potential mobile application and a reduction of development time, they are especially attractive for lab research.

Frequently quoted disadvantages of microreactors are the high fabrication cost, low throughput, incompatibility with solids and the omission of cost reduction by scale up effects which lead to still poor industrial acceptance. Distribution and fouling problems often prevent the industrial application of completely miniaturized reaction systems. Instead it seems that multiscale approaches (Bayer et al., 2004) are increasingly successful regarding application on pilot or plant scale. This means that the appropriate scale is selected for the respective purpose, and size reduction is often limited according to the policy "as small as necessary" (Jähnisch et al., 2004).

Heterogeneously catalyzed gas-phase reactions in microreactors

Although the specific surface of microreactors is extremely high, compared to conventional vessels, it is still relatively low compared to the porous materials applied in heterogeneous catalysis. Thus, if heterogeneously catalyzed gas-phase reactions are to be performed in microreactors, the number of catalytically active sites states the limiting factor, unless further actions are taken to drastically increase the available surface.

The inner surfaces of microchannels can either be increased by chemical modification of the wall material, for example by means of anodic oxidation (Wießmeier and Hönicke, 1996) or by introducing additional high-surface materials, for example wash-coating with powder suspensions (Bravo et al., 2004). A further approach is the incorporation of microscale catalyst pellets in a microstructured reactor. The channel dimensions in such fixed-bed microreactors cannot be scaled down beyond a certain limit without generating unreasonable pressure drops. Karim et al. (2005) compare the performance of a fixed-bed and a wall-coated microreactor for methanol steam reforming.

In the fixed-bed microreactor (channel dimension 4.1 mm down to 1 mm) the reaction is heat transfer limited and noticeable temperature gradients are observed, whereas the wall-coated reactor is free from any mass or heat transfer limitations (channel dimension 4.1 mm down to 0.2 mm) and achieves lower pressure drops. The volumetric productivity increases with thicker catalyst wall-coatings. Ajmera et al. (2002) propose a cross-flow design to take advantage of using commercially available catalyst pellets in microreactors, in which the flow is distributed along a wide but short catalyst bed. This design reduces pressure drop and yields an isobaric catalyst bed that utilizes practical quantities of catalyst and flow rates.

A reactor concept that is not a classical microreactor in terms of improved heat transfer, but nevertheless worth mentioning in terms of process intensification, is the millisecond reactor investigated by the group of Schmidt for partial oxidations of hydrocarbons (Hickman and Schmidt, 1993; Huff and Schmidt, 1993). They apply rhodium coated ceramic monoliths with a length of 10 mm and channel dimensions in the micrometer scale, resulting in contact times around one millisecond, realizing high conversions and syngas concentrations.

2.2 Membrane Reactors

Process integration by combining reaction and membrane separation in a single unit promises numerous benefits compared to conventional processes. In the recent years a multitude of concepts has been proposed how membranes can be applied in combination with a chemical or biochemical reaction in order to intensify the process as a whole. All these approaches will be categorized into the three main concepts called extractor, distributor and contactor, which will be illustrated by a few examples. Membranes are generally referred to as structures, which are permeable for at least one component of the surrounding fluid but impermeable for other components. They can be made from different materials such as metals, ceramics and polymers (Melin and Rautenbach, 2007). Different definitions exist for membrane reactors (MR), including or excluding different border cases. The International

Union of Pure and Applied Chemistry (IUPAC) defines a membrane reactor as a device for simultaneously carrying out a reaction and membrane-based separation in the same physical enclosure (Koros et al., 1996). According to a wider definition any reactor in which a chemical reaction is performed in presence of a membrane is called membrane reactor (Saracco and Specchia, 1994). When the reactants pass a membrane unit downstream the reactor vessel and are recycled to the reactor, the behavior of the system is often equivalent to that of a membrane in the reactor (Sirkar et al., 1999). Including these cases, the following definition can be concluded (Sanchez Marcano and Tsotsis, 2002):

A membrane reactor is a combination of a chemical reaction with a membrane process, in which membrane and reaction are integrally coupled creating synergies. Frequently both functions are housed in a single unit.

In a membrane reactor the membrane can fulfill different functions (Julbe et al., 2001):

- Selectively remove the products from the reaction mixture (Extractor),
- Control the addition of reactants to the reaction mixture (Distributor),
- Intensify the contact between reactants and catalyst (Contactor).

A variety of combinations of these functions is possible, but the classification demonstrates the diverse applications of combining membranes and reactions. The combination of biological reactions with membrane separations is state of the art technology and applied industrially since the 1950s. Due to the low temperature and pressure range commercial organic membranes can be used for most applications. The basic principles selective product removal, retention of biocatalyst and selective substrate addition correspond to those mentioned for chemical reactions. That is why membrane bioreactors will not be further discussed in this work. A comprehensive review on applications and perspectives of membrane bioreactors is given for example by Giorno and Drioli (2000).

Fundamentals of membrane processes

A module is a membrane arrangement with at least one fluid connection on either side of the membrane. On the upstream side the stream entering the module is called "feed", a stream leaving on this side contains the retained components and is therefore called "retentate". On the downstream side the stream leaving the module contains the components that have passed the membrane and is called "permeate", a stream entering the module on the downstream side is called "sweep".

Two parameters are important for the assessment of membrane separations: Permselectivity describes the ability of the membrane to discriminate between two components of a mixture, permeability quantifies the permeate flow per membrane area. For the selection of an appropriate membrane additionally the investment cost for membrane material and production as well as the chemical, thermal and long-term stability have to be considered (Melin and Rautenbach, 2007).

Membrane separations are kinetically driven. That is why a desired increase of permeability is often connected with a reduced selectivity. The driving force is usually a pressure or partial pressure gradient, respectively. Porous membranes retain particles or molecules that are larger than the pore size. For gas separations the ratio between mean free path of the molecules and the pore size is important for the transport mechanism. In dense (i.e. non-porous) membranes the permeation rate of different components and thus the permselectivity is primarily defined by the solubility and mobility of the components in the homogeneous membrane phase.

Organic polymer membranes are established for low temperature applications, especially in membrane bioreactors. Porous organic membranes are usually made of polysulfone, polyacrylnitrile or polypropylene; dense organic membranes of silicone, perfluorpolymers, polyimide or polyamide.

Inorganic membranes generally have the advantage of an increased range of applications concerning temperature and chemical stability. That is why for catalytic reactions almost exclusively anorganic membranes are used. Disadvantageous are the costly fabrication and the difficult sealing which mostly

imply considerably higher investment costs. Dense inorganic membranes are either composed of noble metals (Pd, Pt, Ag and alloys) or of conductive ceramics (perovskites, modified zirconia). They feature high selectivities and almost exclusive permeation for hydrogen or oxygen.

The most important H_2 permselective membrane material is palladium. Hydrogen molecules adsorb dissociatively on the membrane surface, H-atoms are incorporated in the metal lattice and diffuse through the lattice until they desorb on the surface recombining to molecular H_2. During sorption of the atomic hydrogen the Pd-lattice expands, leading to embrittlement and crack formation. Addition of alloy metals such as Ag, Cu or Ni strongly reduces this problem (Gryaznov and Orekhova, 1998). Mixed conductive perovskite membranes are dense inorganic membranes from crystalline mixed metal oxide, which allow an extremely selective permeation of oxygen in the temperature range between 600 °C and 1000 °C. Silver membranes are also very permselective for oxygen (Saracco and Specchia, 1994).

Porous inorganic membranes are made from a variety of materials: Noble metals, alloys and stainless steel, ceramics such as aluminum oxide, silicon oxide, titanium oxide, zirconium oxide, zeolites, carbon or diverse glasses. Concerning membrane reactors the most interesting question is if the membrane material itself is catalytically active or if catalytically active material can be incorporated into the pore structure. Reviews on the application of porous ceramic membranes in catalytic reactors have been published by Julbe et al. (2001) and Coronas and Santamaria (1999).

Composite membranes are supposed to combine the permselectivities of dense or microporous membranes with the permeabilities of macroporous membranes. They are usually composed of different materials forming an asymmetrical structure. A thin separation layer is responsible for the permselectivity, whereas a porous support layer made of ceramics, glass or metal accounts for stability and allows relatively high permeability.

Saracco and Specchia (1994) and Zaman and Chakma (1994) give comprehensive reviews on the applications of the different membrane types as membrane reactors.

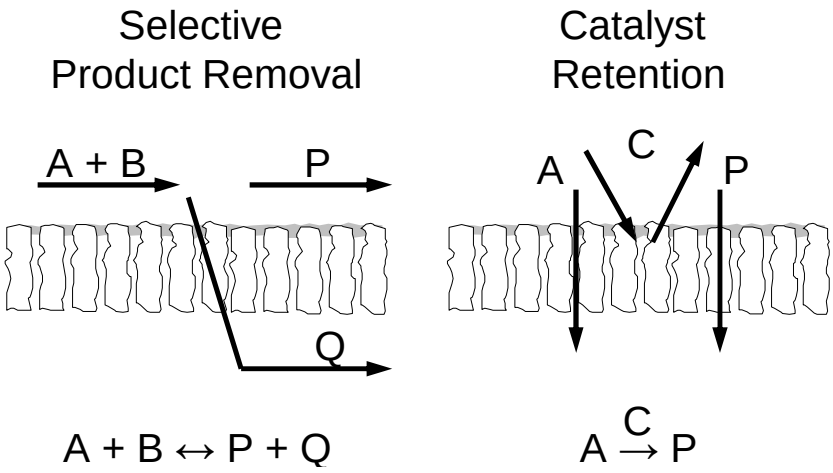

Figure 2.1: Principles of extractor membrane reactors

2.2.1 Extractor Membrane Reactors

The most common type of membrane reactor works according to the extractor principle. This can be further differentiated into "selective product removal", which means that only the product permeates through the membrane and "catalyst retention", describing that all components except the catalyst permeate (Fig. 2.1).

Selective product removal

One component that is generated in the chemical reaction is continuously and selectively removed from the reaction mixture. If the reaction is limited by the thermodynamic equilibrium, the hypothetic equilibrium conversion, that can be reached in a closed system, can be outperformed by reducing the activity of the removed component (Dixon, 2003).

In addition to the equilibrium shift, this mode of operation can reduce undesired side or sequential reactions. If the reaction rate of the undesired secondary reaction is higher than that of the primary reaction, the reaction selectivity can be significantly increased by removing the desired intermediate species. If one of the products acts as inhibitor, as in some fermentations, removing this product strongly improves the reactor productivity. Furthermore MR allow much higher substrate concentrations (Sirkar et al., 1999).

A further advantage of selectively removing the valuable product lies in avoiding further separation steps or at least in reducing the separation effort by increased product concentrations.

To generate a driving force for permeation, the partial pressure of a component on the permeate side has to be smaller than that on the feed side. This can be accomplished by a difference in absolute pressure, by dilution of the permeate side with an inert component or by applying a reactive sweep gas.

The most frequent applications of extractor membrane reactors are catalytic dehydrogenations of light alkanes or reactions for hydrogen generation, such as steam reforming or water-gas-shift, applying H_2-permselective membranes. Dittmeyer et al. (2001) give an extensive overview on the application of different Pd-based membranes for dehydrogenation reactions. Water-permeable membranes, such as zeolite or pervaporation membranes can be applied for esterification reactions (Lipnizki et al., 1999) or Fischer-Tropsch synthesis (Espinoza et al., 2000).

Catalyst retention

The main function of the membrane can also be the retention of a homogeneous or heterogeneous catalyst or of precious smaller ligands, allowing the permeation of the residual reaction mixture. This concept is especially popular in biocatalytic applications (Giorno and Drioli, 2000) and can be either realized by immobilizing the catalyst on the membrane surface or by a membrane filtration with a solved or dispersed catalyst. In case of homogeneous catalysts, the alternative process of thermal recovery is often uneconomic due to low concentrations and can lead to deactivation of the catalyst.

The concept of immobilizing a catalyst of small molecule size on an easily retainable soluble polymer is well-known for enzymes (Rios et al., 2004) but can also be transferred to chemical reactions (Wöltinger et al., 2001).

Immobilization is often difficult and usually reduces the catalytic activity. In this case catalyst retention by nanofiltration (NF) can be a reasonable alternative, when chemical and physical stability of the membrane can be

guaranteed. A field of application is the chiral catalysis, where expensive metal complexes are used as homogeneous catalysts with high reactivity and enantioselectivity, which are not allowed to appear in the product (Kragl and Dwars, 2001).

2.2.2 Distributor Membrane Reactors

The distributor principle is the second field of application for permselective membranes in chemical reactors. One reactant is specifically added to the reaction mixture across a membrane. Within this concept, a membrane can fulfill two completely different functions: Even distribution of the limiting reactant along the reactor can prevent hot spots and side reactions. On the other hand, the membrane can be used as upstream separation unit, selectively dosing one component from a mixture (e.g. O_2 from air). In the latter case the coupling of separation and reaction lies in an increased driving force for permeation as the permeating component reacts directly after permeation. Both functions can of course be combined. Fig. 2.2 shows a sequential reaction with the desired product P and the undesired product Q performed in a distributor membrane reactor. Selective addition of component B leads to a continuously low concentration of B. Assuming power law kinetics, a MR can reach a higher selectivity to product P than a conventional reactor, if the reaction order of component B in the desired reaction is smaller than in the undesired reaction. As component A is consumed along the reactor length, one remaining problem is the reduction of the ratio of A to B along the reactor, if B is constantly added. This phenomenon is aggravated by the influence of the pressure drop along the catalyst bed on the permeate side of the membrane, which leads to an increasing pressure gradient and therefore to an increasing permeation rate towards the reactor end (Armor, 1995). An additional problem for the application of porous membranes is backdiffusion of component A across the membrane.

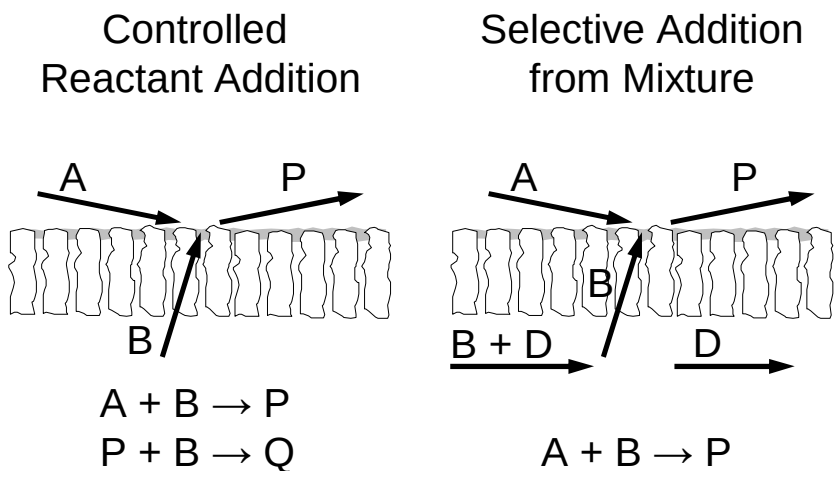

Figure 2.2: Principles of distributor membrane reactors

Partial oxidation reactions

Gas phase partial oxidation of hydrocarbons is a typical example for systems with competing reactions. Usually the intermediate products react more intensively with oxygen than the reactants, thus a controlled addition of O_2 can prevent total oxidation. In most applications of the distributor principle, the membrane is used to control the oxygen concentration along a fixed bed catalytic reactor within certain boundaries (Sanchez Marcano and Tsotsis, 2002). In some cases it is more suitable to permeate the other component across the membrane as Peña et al. (1998) report for the epoxidation of ethylene.

Due to the high permselectivity of certain dense membranes towards oxygen, the use of air on the feed side of the MR is possible. For satisfactory permeability these membranes need temperatures above 700 °C. As almost exclusively reactions with methane are performed in this temperature range, the main applications of dense membranes in distributor membrane reactors are the oxidative coupling of methane (OCM) and the partial oxidation of methane to syngas (GTL = gas to liquid).

Coupling of reactions

A sweep gas on the permeate side dilutes the permeating component and thereby reduces its chemical potential. By means of a reactive sweep gas the chemical reaction on the permeate side further increases the gradient of the chemical potential and thus the driving force for permeation. For example if the dehydrogenation of cyclohexanol is performed with synthetic air as reactive sweep gas instead of nitrogen, the conversion can be increased (Schramm and Seidel-Morgenstern, 1999).

The potential of combining extractor and distributor principle by simultaneously performing a catalytic dehydrogenation reaction on the feed side of a membrane and a hydrogenation reaction on the permeate side has been investigated early. The reaction on the permeate side maintains the chemical potential gradient. Energetic coupling of two reactions also allows for autothermal operation, when an exothermic reaction provides the energy for an endothermic reaction. For instance the endothermic steam reforming of methane can be combined with an exothermic partial oxidation (Sanchez Marcano and Tsotsis, 2002).

2.2.3 Contactor Membrane Reactors

The two-sided geometry of membranes allows for different options to bring reactants into contact. Especially interesting are the concepts interfacial contactor, which can separate either different phases or different reactants of the same phase, and forced flow-through, where the reactants are fed from the same side of the membrane (fig. 2.3).

Gas-liquid contactor

In a multi-phase contactor the membrane controls the contact between different phases of a reaction mixture. The membrane can spatially separate gas-liquid or aqueous-organic systems and is often catalytically active.

A membrane reactor with a gas and a liquid flowing on different sides of the membrane is also called "catalytic diffuser" (Dittmeyer et al., 2001).

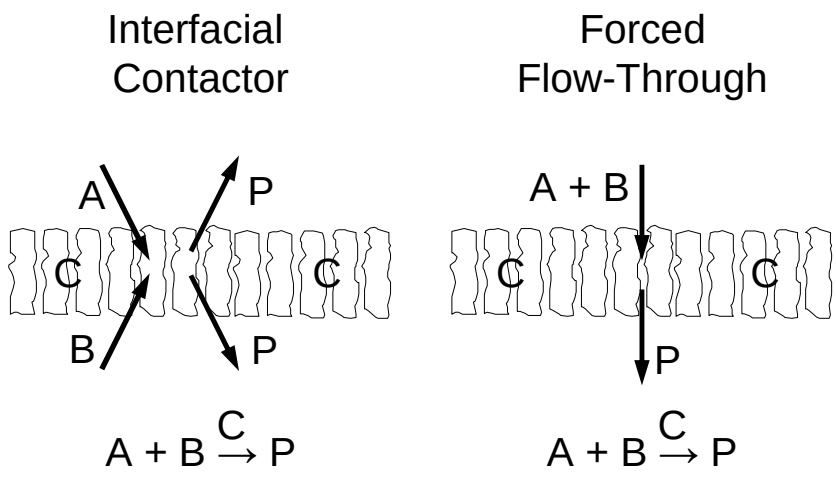

Figure 2.3: Principles of Contactor Membrane Reactors

The catalytically active layer faces the liquid side, capillary forces suck the liquid into the pores as far as the transmembrane pressure allows. The gas diffuses through the macroporous support layer and dissolves in the liquid at the interface. The solute further diffuses through the liquid filled pores and reacts at the catalytically active centers at the pore walls. Due to the pressure gradient, the reaction products preferentially diffuse in direction of the liquid side.

The addition of reactants from different sides of a membrane allows independent tuning of the streams. The gas pressure can be varied between the wetting pressure of the support layer and that of the active layer. Additional substances can be targeted to the catalytic region without mass transport resistances. Even for low solubilities high pressures are not required, because the gas is supplied directly where it is consumed.

An exemplary application is the selective oxidation of light alkanes under mild conditions by means of super acidic catalytic membranes (Sanchez Marcano and Tsotsis, 2002). The concept is also interesting for liquid phase hydrogenations as hydrogen is poorly soluble in organic liquids.

Aqueous-organic contactor

The selective oxidation of hydrocarbons by phase transfer catalysis is commonly performed in stirred tank reactors with subsequent product separation. The oxidant is located in the aqueous phase, the hydrocarbons form the organic phase. Important parameters are a large interface for intensive phase contact but also preferably low emulsification for simple phase separation. If a microporous membrane is used as contactor supplying the oxidant, aqueous and organic phase stay separated and no solvent is required (Dixon, 2003).

Unselective interfacial contactor

Two different reactants of the same phase are separated by a porous membrane, forming an interface inside the membrane. The reactants remain separated until they reach the catalytically active centers on the pore surface, where a controlled reaction front is formed. In this arrangement a permselectivity is not required, the membrane only supplies the reaction zone. The partial pressure difference forces the reactants to diffuse towards each other until they meet in the catalytic zone. If the reaction is faster than the mass transport in the membrane, a reaction front is formed which prevents the permeation of unreacted components. Due to automatic adjustment of the reaction front, the concept is especially interesting for systems with fluctuating concentrations.

An exemplary application is the controlled catalytic combustion for energy recovery. The conversion can easily be controlled by varying the pressure difference. The separation of reactants prevents runaway (Dixon, 2003). This reactor type can also be used for the complete conversion of pollutants, as proven by Zaspalis et al. (1991) with the selective catalytic reduction of nitric oxide with ammonia to nitrogen and water.

The unselective interfacial contactor is the concept most closely related to the flow-through catalytic membrane reactor. Both use unselective catalytic membranes and in both concepts the membrane provides the reaction space. Consequently the applications are somewhat similar. The difference is, that in the interfacial contactor mode the reactants are fed from different sides of

the membrane, whereas in forced flow-through mode the premixed reactants are supplied from the same side in dead-end mode, creating a completely different reactor behavior.

Forced flow-through

In this concept an unselective porous catalytic membrane is applied in dead-end mode, forcing the reactants to flow through the membrane. The function of the membrane is to provide a reaction space with short controlled residence time and high catalytic activity. In classical fixed bed reactors the conversion is limited by pore diffusion. If the catalyst is placed inside the membrane pores and the reactants flow convectively through the pores, the resulting intensive contact between reactants and catalyst leads to high catalytic activity. As this concept is the main topic of this work, an extensive review on applications of membrane reactors in forced flow-through configuration is given in the separate chapter 2.3.

2.3 Flow-Through Catalytic Membrane Reactors

Catalytic membranes without separative function have successfully been applied as microstructured reactors (Dixon, 2003). If the reactant mixture is forced to flow through the pores of a membrane, which have been impregnated with catalyst, the intensive contact allows for high catalytic activity with negligible mass transport resistances (Zaspalis et al., 1991). Several review articles mention this topic as a special type of membrane reactors (Saracco and Specchia, 1994, 1998; Saracco et al., 1999; Dixon, 1999, 2003; Sirkar et al., 1999; Julbe et al., 2001; Sanchez Marcano and Tsotsis, 2002; Dittmeyer et al., 2004; Schomäcker et al., 2005; Westermann and Melin, 2005).

In the early 1990s this setup was still regarded a less investigated concept (Saracco and Specchia, 1994). Dixon (1999) identified the control of contact time as a promising area for membrane reactor research. In 2003 the same

author already observed increased use of membranes to control the contact time of reactants and catalysts, particularly in the flow-through configuration and forecasted it to become a strong third area of catalytic membrane reactor research amongst the permselective extractor and distributor membrane reactors (Dixon, 2003). Schomäcker et al. (2005) first published a review dealing exclusively with flow-through catalytic membrane reactors (FTCMR), differentiating between gas phase integral reactors with stoichiometric feed of reactants and liquid phase differential reactors consisting of a loop of a membrane module and saturation tank.

The work at hand intends to give an exhaustive overview on the research results obtained with this reactor configuration as published in the recent 20 years. The works known to the author feature a variety of subconcepts. The motivation for applying a FTCMR is either the aim to reach complete conversion in minimum time or space, taking advantage of the high catalytic efficiency, or to reach maximum selectivity for a given reaction due to the narrow contact time distribution. As an attempt to give a systematic overview, the publications are structured into three concepts:

- Complete conversion integral FTCMR are designed to reach complete conversion in a single pass. They are mostly applied to gas phase reactions, with a few exemptions of multi-phase reactions (Subsection 2.3.1).
- Selective integral FTCMR try to achieve optimum selectivity in a single pass through the catalytic membrane. They are also preferably used for fast gas phase reactions, mainly partial hydrogenations and oxidations (Subsection 2.3.2).
- Selective differential FTCMR are operated in a semi-batch mode in a loop of membrane module and a saturation tank, causing only small conversions per pass, with the aim of reaching high selectivities. They have exclusively been investigated for partial hydrogenations in liquid phase, which are limited by the low solubility of hydrogen (Subsection 2.3.3).

2.3.1 Complete Conversion Integral FTCMR

In this mode of operation the premixed reactants flow through the catalytic membrane in a single pass with the aim of reaching complete conversion, taking advantage of the high catalytic efficiency caused by the intensive contact between the reactants and the catalyst. This mode has been applied to several gas phase reactions, such as isomerization of 1-butene or conversion of CO. The most applications are in the area of decomposition of volatile organic compounds (VOC), including photocatalytic oxidations. An overview of the applied catalytic membranes and the performed reactions is given in Table 2.1.

Gas phase reactions

The first application of a catalytic membrane as flow-through reactor is reported by Yamada et al. (1988). By means of anodic oxidation of aluminum plates and subsequent removal of the membranes from the substrate, catalytic membranes are prepared with a thickness of 5 to 50 µm for single-sided oxidation and 50 to 100 µm for double-sided oxidation respectively. In the reactor setup the fluid permeates from one side to the other through the catalytic membrane. For the model reaction isomerization of 1-butene the membrane reactor shows similar or sometimes higher catalytic activity compared to powder of anodized alumina film.

For the preprocessing of gas mixtures in gas analyzing systems, Splinter et al. (2002) design a micro membrane reactor as flow-through system. In order to increase the sensor selectivity, CO is converted to CO_2 while passing through the catalytic membrane. The reactor is fabricated by a combination of anisotropic silicon etching to create the membrane and porous silicon technology to perforate the membrane. The advantage of porous silicon as a flow-through system is the adjustable pore diameter (here: 4 to 8 µm) with a high open porosity, a large reactive surface and a ramified structure, which is supposed to enable gas turbulence. The membrane area is smaller than a square millimeter resulting in porous silicon surfaces between 8.6 cm^2 and 39.4 cm^2. The applied gas molecule retention times are around 1 ms. The

Table 2.1: Integral Flow-through Catalyic Membrane Reactors for complete conversion (d_{pore} = Mean pore diameter; t_{cat} = Thickness of catalytic layer)

Authors	Reaction	Membrane	Catalyst	d_{pore} [nm]	t_{cat} [µm]
Yamada et al. (1988)	1-butene isomerization	Anodized alumina	none	~ 100	5-100
Splinter et al. (2002)	CO oxidation	Porous silicon	Pd, wet impregnation	4 000-8 000	70
Saracco and Specchia (1995)	VOC decomposition	Porous ceramic	γ-Al_2O_3, urea method	1 000-15 000	1 500
Pina et al. (1996)	VOC decomposition	γ-Al_2O_3 on MF	Pt, wet impregnation	3.5	$\approx 1\,700$
Zalamea et al. (1999)	VOC decomposition	γ-Al_2O_3 MF	Pt, wet impregnation	2 000-10 000	1 000
Maira et al. (2003)	TCE photocat. oxidation	Zeolite on porous steel plate	TiO_2	~ 1	5
Tsuru et al. (2003)	Methanol photocatalytic oxidation	α-Al_2O_3-MF	TiO_2, colloidal sol	6.5	n/a

silicon substrate is simmered into $Pd(acac)_2$ dissolved in toluene in order to cover the pore walls. The complete porous silicon surface area of approx. $100\,m^2/cm^3$ is thus covered with a Pd-layer of 700 nm. In comparison to an overflowed porous surface or a micro reaction chamber the "flow-through" membrane shows an optimized conversion factor, a low dead volume and small dimensions. The time of reaction depends on the membrane thickness. Active area and retention time can be adjusted to convert nearly 100 % of the specified gas.

VOC decomposition

For potential application in flue gas cleaning, Saracco and Specchia (1995) and Saracco and Montanaro (1995) catalytically activate ceramic porous filters by applying a γ-alumina layer. While the filter mechanically removes the particles, the catalytically active membrane decomposes the chemical pollutants such as NO_x and VOC that are forced to flow through it. The capability of the filters is assessed by performing the dehydration of isopropanol which is catalytically promoted by the γ-alumina itself. Nearly complete conversion can be achieved for superficial velocities of industrial interest ($1\,m_N^3/m^2s$) .

The concept of a FTCMR working in the Knudsen-Diffusion range is investigated for complete combustion of VOC by Pina et al. (1996). In a commercial MF-membrane with a γ-Al_2O_3 separation layer and pore diameters of 200 nm a further γ-Al_2O_3 phase is deposited by the sol-gel method and catalyst is introduced by wet impregnation. The catalyst is activated with H_2 at 400 °C for two hours. The Pt loading on the membranes is determined as 0.13 wt% by UV-vis of the impregnation solution. A lean VOC-containing stream (100 to 5100 ppm toluene) is forced to permeate through a Pt/Al_2O_3 catalytic membrane operating in Knudsen diffusion regime to provide intimate contact between the VOC molecules and the combustion sites, minimizing the diffusion resistances present in other systems and providing highly efficient use of the catalyst. A total gas flow of 0.4 to 1.0 L/min results in superficial velocities of 3 to 7.5 m/h with considerable pressure drops of 0.18 to 0.35 bar. Laminar and Knudsen contributions to the total flux are

evaluated from permeation experiments with oxygen at room temperature. If the permeation flux is plotted against the average pressure, the slope represents the viscous contribution and the intercept the Knudsen contribution. The minimum temperatures to achieve complete conversion are reported to be considerably low.

While the investigations of Pina et al. are limited to the Knudsen regime, Zalamea et al. (1999) apply mixed-regime catalytic membranes to the combustion of volatile organic compounds. Identifying the considerable pressure drop as the major drawback of the Knudsen diffusion system, the application of membranes with wider pores is an obvious alternative. The increased pore size results in significant Knudsen and laminar contributions. On the support membranes with a homogeneous tubular structure, 2 to 3 wt% of γ-Al_2O_3 is deposited as well as 0.15 % of Pt catalyst by wet impregnation. The catalytic membranes show a BET surface of $5.9\,m^2/g$, while most of the pore volume is contributed by large pores (2 to 10 µm). The relative contributions of the Knudsen and laminar terms to the permeation flux are again determined by performing permeation experiments. The temperatures required for complete conversion in the mixed regime membranes with higher laminar contribution are compared with those of the asymmetric membranes with high Knudsen contribution. As expected the temperatures required in the Knudsen regime are lower at the expense of a much higher pressure drop. Taking into account the operating costs, a mixed permeation regime may be preferred in spite of an increase in combustion temperature by 15 to 50 °C.

Photocatalytic oxidation

Maira et al. (2003) investigate the effect of the flow configuration on the gas phase photocatalytic oxidation of trichloroethylene, applying two different catalytic membranes and a catalytic stainless steel plate. While both the catalytic stainless steel plate and the hybrid zeolite-TiO_2 membrane-catalyst show catalytic activity in parallel flow mode, the conversion can be radically increased by switching to flow-through mode or a mixed flow mode respectively. Regarding selectivity, the membrane-catalyst outperforms the

catalytic plate, which is explained with a possible retention of larger pollutant molecules by the membrane.

The gas-phase oxidation of methanol as a model volatile organic component in a photocatalytic membrane reactor is studied by Tsuru et al. (2003). After fabricating TiO_2 membranes with pore sizes of several nanometers on cylindrical α-alumina microfiltration membranes, the decomposition rate of methanol is investigated. An air stream with a methanol load of 1000 ppm is fed to the shell side of the membrane tube, which is irradiated with blacklight lamps to catalyze the generation of OH radicals on the TiO_2 surface. Two different flow patterns are applied: In the first mode without permeation, the product stream is also taken from the shell side, allowing the reactants to contact the catalytic surface by diffusion only. In the second mode with permeation, the reactants leave the reactor on the tube side of the membrane, forcing them to flow convectively to the surface and through the membrane pores and thus providing for more efficient contact between the reactants and the catalytically active TiO_2 surface. A higher decomposition rate is observed for the reactor mode with membrane permeation. This is contributed to two factors: the enhanced transport to the surface by forced convection in addition to the transport by diffusion as well as to the utilization of a larger surface area. For a single pass through the membrane, the authors conclude a uniform residence time for the reaction.

2.3.2 Selective Integral FTCMR

This mode of operation is very similar to the one described in the previous section, as the premixed reactants flow through the catalytic membrane in a single pass. The subdivision into two separate sections is chosen, because the application to sequential reactions implies an additional motivation and therefore additional requirements towards the membrane. In addition to the high catalytic efficiency of FTCMR, the concept takes advantage of a narrow residence time distribution, limiting sequential reactions towards undesired byproducts. Thus a regular pin-hole free microstructure is essential to prevent maldistribution effects. Intrinsic maldistribution effects are well known

for monolithic reactors (Kreutzer et al., 2005), but can hardly be directly measured for membrane reactors due to the smaller scale and lack of distinction between separate channels. Thus, sequential reactions with desired intermediate products are commonly performed as indirect proof of the narrow residence time distribution compared to competing reactor concepts.

The integral membrane reactor setup has been applied to several sequential reactions, mainly in the gas phase, such as partial oxidation, partial hydrogenation, oligomerization or coupling reactions of hydrocarbons. Only in a few cases a liquid phase is present during the reaction, allowing for the term "three-phase reactor". The applied membranes, reactions and catalysts are summarized in Table 2.2.

Partial oxidation reactions

The first application of the FTCMR concept for selective reactions dates back to the early 1990s, when Zaspalis et al. (1991) use non-separative catalytically active alumina membranes for the dehydrogenation of methanol to formaldehyde. Two different configurations are investigated: In mode A both reactants enter from the same side but the products are allowed to leave on both sides of the membrane, in mode B all the feed is forced to diffuse through the membrane. In both configurations the membranes exhibit a high catalytic activity for the dehydrogenation of methanol, but the reactant configuration and the mode of operation are regarded as important parameters for the performance of a catalytic membrane reactor. In mode A a preferential distribution of the products on opposite sides of the membrane is observed due to different diffusion paths resulting in different contact times with the catalyst. High purging rates on the permeate side increase the activity of the membrane by preventing backdiffusion. The flow-through mode B leads to maximum conversions but minimum selectivities due to comparatively high residence time of methanol in the catalytically active layer. The observed activity per gram of material is up to ten times higher than in a comparable tubular reactor with a catalytic bed of the same material. This is attributed to the higher effective surface area accessible to the reactants.

Table 2.2: Integral Flow-through catalyic membrane reactors for selective sequential reactions (d_{pore} = Mean pore diameter; t_{cat} = Thickness of catalytic layer)

Authors	Reaction	Membrane	Catalyst	d_{pore} [nm]	t_{cat} [µm]
Zaspalis et al. (1991)	CH_3OH sel. dehyd.	α-Al_2O_3	γ-Al_2O_3	3-4	7-8
Kobayashi et al. (2003)	Propane selective epoxidation	Microporous glass	Cs-Ag, Re-Ag, Ag_2O	220-480	1 000
Zhu et al. (2003)	Propane sel. oxid.	α-Al_2O_3 support	AgBiVMo oxide	2-20	5-10
Pellin et al. (2005)	Cyclohexane oxidat. dehydr.	Anodized Al_2O_3	VO, atomic layer deposition	10-38	70
Mucherie et al. (2007)	Propane oxidat. dehydrogenation	Anodized Al_2O_3	VO, atomic layer deposition	40	70
Alfonso et al. (2001)	Butane oxidat. and non-ox. dehydr.	α-Al_2O_3; Layer 1 α-Al_2O_3; Layer 2	V/MgO Pt-Sn/γ-Al_2O_3	200 / 12 000 < 200	30 / 1 000 30
Schuessler et al. (2001)	Methanol reform.	Mixed-matrix Cu	Cu/ZnO	≈ 10 000	≈ 800
Lange et al. (1998)	Hexadiene sel. hyd.	Asym. ceramic	Pt	5	0.2-0.4
Lambert and Gonzalez (1999)	C_2H_2/butadiene part. hydr.	Asym. γ-Al_2O_3	Pt/γ-Al_2O_3 by sol-gel	3.6	11
Vincent and Gonzalez (2002)	Acetylene partial hydrogenation	Asym. γ-Al_2O_3	Pd/γ-Al_2O_3	3.6	5
Gröschel et al. (2005)	Propyne prt. hydr.	Porous polymer	Pd particles	3 600	1 000
Ma et al. (1998)	Methane ox. coupl.	Asym. α-Al_2O_3	Sm_2O_3	20-5 000	30
Torres et al. (2003)	Isobutene dimeriz.	Porous ceramic	Zeolite layer	1.4-5.0	3.5
Fritsch et al. (2004)	Isobutene dimeriz.	Porous polymer	Sol. acid copol.	410-610	3.8-150
Khassin et al. (2005b)	Fischer-Tropsch	Porous metal	Co-Al co-precip.	500-3 000	5 000

The heterogeneously catalyzed selective epoxidation of propylene in a flow-through membrane reactor is studied by Kobayashi et al. (2003). Three different catalysts (Cs-Ag, Re-Ag and Ag_2O) are immobilized in the pores of a micro-porous glass membrane and applied to three different reactor systems: A convection-flow reactor, a diffusion flow reactor and a packed-bed-flow reactor. Reaction rates are determined for CO_2 and propylene oxide, keeping the total conversion of propylene below 10 %. Comparing the three immobilized catalysts, the selectivity towards propylene oxide increases with the amount of intermediate formed on the catalyst, which strongly depends on the types of catalyst and the reactor system. The highest selectivity towards propylene oxide is achieved with the convection-flow reactor and Re-Ag catalyst, demonstrating hysteresis kinetics depending on the increase or decrease in the propylene concentration. The convective flow through the membrane pores effectively enhances the selectivity towards propylene oxide.

After attempts to improve reaction yield and selectivity by means of inert membrane reactors in distributor or extractor mode, Zhu et al. (2003) apply a catalytic membrane reactor in flow-through mode to the selective oxidation of propane to acrolein. Benefits are expected from the high contact surface combined with a short and controlled contact time in the 5 to 10 µm thin catalytic layer in order to prevent total oxidation. A tubular mesoporous mixed oxide catalytic membrane with a length of 6 cm is generated by means of a modified sol-gel-method. The catalytic reaction is carried out at 400 °C at atmospheric pressure. The FTCMR, operated with reactants flowing from shell to tube side, is compared with a fixed bed reactor (FBR), the liquid products are collected in a cooling trap. For the FTCMR the catalyst loading is 50 to 100 mg, whereas the FBR is loaded with 2 g of catalyst. The experimental results are limited to a comparison of the selectivities without giving numbers for conversion or yield. In the FTCMR selectivities towards acrolein higher than 50 % are reached, compared to less than 10 % for the FBR, which produces mainly methanol and acetic acid in the liquid phase product.

Pellin et al. synthesize mesoporous ultra-uniform inorganic catalytic membranes by a combination of anodic alumina oxidation and atomic layer de-

position (Pellin et al., 2005; Stair et al., 2006). Pore diameter and pore wall composition can be controlled along the entire pore length. The pores of anodic alumina membranes (thickness 70 µm) with initial pore diameters of 40 nm are coated with a thin alumina layer of 1 nm or 15 nm respectively, resulting in pore diameters of either 38 or 10 nm. The catalytic performance of the membranes is compared to that of an uncoated alumina membrane, after adding one monolayer of vanadium oxide each. Additionally, the membranes are compared to a conventional high surface area γ-alumina powder catalyst with vanadium oxide impregnation. As a test reaction, the oxidative dehydrogenation of cyclohexane is studied at temperatures of 450 °C, yielding higher selectivities for the partial oxidation product cyclohexene for all three catalytic membranes compared to that of the catalytic powder. The observed reduction of secondary reactions is attributed to a decrease of contact time by a factor of 1 000 - 10 000 compared to the conventional catalyst bed. For higher temperatures the specificity of the membrane is reported to decrease, but in all cases the membranes outperform conventional supported alumina catalysts. While the conversion of O_2 and C_6H_{12} is lower for the 10 nm membrane than for those with larger pores, the conversion per mole vanadate is significantly higher. With the same approach the oxidative dehydrogenation of propane is examined (Mucherie et al., 2007). Catalytic layers composed of vanadium species supported on different metal oxides (Al_2O_3, Nb_2O_5, TiO_2) are compared. Highest reactivity is observed for TiO_2, which is attributed to the highest dispersion, whereas the selectivity at 3 % conversion is highest for the Al_2O_3 based catalyst.

In order to develop a model capable of predicting the transport and kinetic behavior inside these nanostructured catalytic membrane reactors fabricated by anodic oxidation and atomic layer deposition, a computational study is performed by Albo et al. (2006). The selective oxidation of hydrocarbons is chosen as model reaction to assess the prevention of over-oxidation taking advantage of the short contact time. Starting from detailed atomistic molecular dynamics simulations in pores with diameters between 10 and 150 nm, Knudsen diffusion is identified as the dominant mass transfer mechanism, accentuated in the smaller pores and at lower pressures, whereas surface

diffusion is only present at temperatures below 700 K. Based on these results, the number and location of hits between the particles and the wall are calculated as well as the residence time of the particles and the transport diffusivity. Regarding the distribution of hits along the pore length, the trajectories that reach the opposite end of the pore concentrate the maximum number of hits at the center of the pore and the minimum at the extremes. On the other hand, the trajectories that return to the initial point have the maximum amount of hits near the entrance of the pore and the fraction of the total hits drastically decreases with the distance from the entrance. As atomic layer deposition allows for the generation of cylindrical pores with multiple sections of different diameters, the calculations are later extended to account this modified geometry (Albo et al., 2007).

The geometry of membranes allows the creation of distinct catalytic layers. These can be used to thermally and chemically couple reactions. Alfonso et al. (2001) apply such a multilayered flow-through catalytic membrane to consecutively carry out the oxidative and non-oxidative dehydrogenation of butane. The oxidative dehydrogenation layer is prepared by sequential impregnation with V supported on MgO. The second layer is prepared by sol-gel procedures with Pt-Sn on γ-Al_2O_3. A premixed butane/oxygen/inert feed with an excess of butane enters the membrane and takes part in two consecutive reactions at the two different catalytic layers. The oxidative dehydrogenation of butane takes place in the first layer, which contains a V/MgO catalyst, consuming most or all of the oxygen in the feed. The product stream of the first reaction subsequently enters the second catalytic layer (Pt-Sn/γ-Al_2O_3), where the non-oxidative dehydrogenation takes place. The endothermic non-oxidative dehydrogenation step consumes the heat generated in the first reaction (thermal coupling), and dehydrogenate both the unreacted butane and the formed butene. Additionally, the byproducts of the first step, CO_2 and steam, are expected to act effectively as inhibitors of coking in the second catalytic layer. If the catalytic materials in both layers can be segregated and the reaction is operated such that complete oxygen consumption is obtained within the oxidative layer, the two-layer membrane reactor allows for stable operation with high conversion and selectivity.

Schuessler et al. (2001) develop a reactor design for the autothermal reforming of methanol for mobile applications. The concept is based on flowing through a stack of thin porous catalytic disks. Although this setup is not explicitly called a membrane reactor it features all the aspects of an FTCMR. Autothermal reactors usually have high temperature gradients in the catalytic zone, which in case of the reforming reaction leads to the formation of the undesired by-products carbon monoxide and methane. To reach nearly isothermal conditions, the heat conduction in the catalytic bed must be improved and the length of the passage limited to a few millimeters. To achieve these requirements the Cu/ZnO catalyst particles (5 to 20 µm) are mixed with copper powder and pressed to porous disks, which are subsequently sintered at moderate temperatures. The resulting mixed-matrix metal membranes are catalytically active, efficiently transport heat and provide an open structure for mass transport. This allows for an operation at optimum temperature, resulting in high reaction rates and selectivities. Additionally the uniform flow distribution is beneficial for the dynamic behavior of the reactor, resulting in negligible fluctuation of stack temperature and product concentration even for feed rate steps with a factor of 20.

A concept that can erroneously be considered a FTCMR is presented by Liu et al. (1996), who perform the partial oxidation of methane to methanol in a non-isothermal reactor, which contains a non-permselective membrane with a pore diameter of 5 nm in the active layer. In this case the task of the membrane is to provide a uniform flow distribution and to separate the hot reactor wall from the inner cooling tube with temperature differences around 450 K. After passing through the membrane the reaction products are quenched in the cold region preventing further reactions. The selectivity for CH_3OH formation at 4.6 % conversion increases from 34 to 52 % when quenching is used. Although initially designed as catalytic membrane reactor, it turns out that the reaction is equally fast in absence of catalyst and thus the catalyst is omitted. Thus the membrane controls the residence time in the hot zone and evenly distributes the reactants to the cooling zone by providing a uniform flow resistance, but the reaction does not take place inside the membrane pores.

Partial hydrogenation reactions

Lange et al. (1998) introduce the concept of single-file diffusion to catalytic membrane reactors. In the idealized case of single-file diffusion through a thin membrane with very narrow pores the molecules cannot pass each other, resulting in an effective prevention of secondary reactions. The result is a one-dimensional movement through the membrane brought about by a pressure gradient. The required microporosity is only available with zeolites or sol-gel materials. An asymmetric ceramic support with pore sizes of 5 nm in the active top layer (thickness 0.2 to 0.4 µm) is applied to the selective hydrogenation of hexenes. Pt is chosen as catalyst in spite of its rather poor selectivity for selective hydrogenation reactions in order to emphasize the influence of the mass transfer resistance. In a special disc membrane reactor, the membrane is situated on a perforated supporting metal plate ($d_h = 1\,\mathrm{mm}$) with carbon gaskets on top of the membrane and below the supporting plate. The observed hydrogenation activity is significantly higher than with comparable batch catalysts, while the prevention of back-mixing increases the selectivity. The observed selectivities for 10^{-7}mol of catalyst in the membrane and a flow rate of 10 to 15 mL/min are reported to be the highest observed with an unmodified Pt catalyst. The extremely low permeability of the membrane represents the major drawback of the reactor.

Lambert and Gonzalez (1999) investigate the activity and selectivity of the partial hydrogenation of the hydrocarbons (HC) acetylene and 1,3-butadiene in a catalytic membrane reactor. The active Pd/γ-Al_2O_3 membrane layer is prepared by the sol-gel method on a macroporous γ-Al_2O_3 tube used as support. The measured pore diameter of 3.6 nm allows for gas separation by Knudsen diffusion. The reactions with 10 % HC/Ar mixtures and different HC/H_2 ratios are performed both with separated feed of reactants and in premixed mode, where H_2 is added to the reactant stream and fed from the tube side. The hydrogenation reactions performed in premixed mode result in the highest selectivity to the partially hydrogenated products while maintaining high conversion without any loss of hydrocarbon species. For the acetylene reaction a high selectivity of ethylene (85 %) at reasonably

high conversions (76 %) is obtained with an excess of H_2 ($H_2/C_2H_2 = 8$) and a temperature of 200 °C at a total flow rate of 18 mL/min. The increased selectivity is explained with the decreased contact time between acetylene and the catalyst.

The term "short contact time reactor" is used by Vincent and Gonzalez (2002) for their FTCMR, pointing out the major advantage compared to other reactor concepts. The selective hydrogenation of acetylene is performed by forcing a dilute $C_2H_2/H_2/Ar$ mixture through a thin Pd/γ-Al_2O_3 catalytic membrane (thickness 5 µm). The membranes are prepared by dipping a porous γ-Al_2O_3 tube substrate into a boehmite sol and subsequent calcination at 400 °C. The tubular membrane is connected to glass tubing with a high-temperature ceramic adhesive. The flow is forced radially through the membrane into the shell. High conversions coupled with a high selectivity are observed, the latter increasing with temperature. The analysis aims at determining whether the membrane can be considered a thin film, if Knudsen diffusion is contributing and if a critical membrane thickness exists for ethylene selectivity and conversion. A one-parameter dispersion equation is chosen to model the successive chemical reaction through a thin catalytic layer. Whereas the dispersion model accurately describes flow within the thin catalyst layer, Knudsen diffusion is found to be negligible. A critical membrane thickness of 2.5 µm is determined for maximum ethylene conversion at the given conditions, corresponding to a tailoring of the residence time.

Porous polymer membranes based on polyacrylic acid networks containing catalytically active palladium nanoparticles are synthesized by Gröschel et al. (Gröschel et al., 2005; Schomäcker et al., 2005). The effects of porosity, catalyst loading and flow rate on the catalytic behavior of the membrane are examined using the gas-phase partial hydrogenation of propyne to propylene as a model reaction. The resulting membrane porosity is varied between 34 % and 72 % with a Pd content of 2 mg. The applied flow rates correspond to residence times of 1 to 4 s, assuming steady state conditions after 5 min. Larger pores lead to longer residence times but worse catalyst distribution, resulting in an optimum porosity as a compromise between residence

time and catalyst distribution. After variation of the catalyst content in the membrane all measured selectivities fall on the same trajectory when plotted against the conversion, indicating that the kinetics are not limited by mass-transfer effects. The activity and selectivity obtained in the membrane reactor is compared with those achieved in a fixed bed reactor filled with porous or egg-shell catalysts. For equal catalyst load and residence times the porous catalysts shows low conversion and poor selectivity, whereas both membrane catalyst and egg-shell catalyst gave equally high conversions and selectivities around 85 %, corresponding to an optimized utilization of the Pd. Simulations of the reaction in membranes are performed to distinguish between kinetic and mass-transfer control. A simplified first-order rate law is fit to the experimental data. As the same rate law is obtained for different membranes with varying porosities, conversion and selectivity only depend on the residence time in the catalytic membrane and not on the pore structure.

Coupling and Oligomerization reactions

Oxidative coupling of methane in different membrane reactor configurations is investigated by Ma et al. (1998), one of them being a radial flow catalytic membrane reactor. Using a vacuum solution technique samarium nitrate is impregnated into the top layer of tubular α-alumina membranes. The premixed reaction mixture of oxygen, methane and helium diluent is fed to the tube side of the membrane reactor, forcing it to flow through the pores. This increases the linear velocity of reactant gases over the catalyst reducing the external mass transfer limitations. Porous catalytic membranes with different pore diameters (5 µm to 0.02 µm) are applied in the temperature range of 750 °C to 900 °C under variation of the flow rates. The performance of all investigated membrane reactors is superior to that of a packed bed reactor made from crushed catalytic membranes. The membranes with the smallest pores show the best results for both conversion and selectivity, confirming the benefits of the Knudsen regime. The location of catalyst inside the membrane is regarded as an important parameter for the reactor performance.

A composite zeolite membrane on a porous ceramic tubular support is

applied to the catalytic oligomerization of isobutene to isooctene by Torres et al. (2003). The reactants are forced to permeate through the membrane, which acts as a thin catalytic layer with a zeolite film thickness in the range of only a few micrometers. In contrast to a fixed-bed reactor no deactivation due to coking and long-chain species is observed, although the obtained conversions are comparable. This is explained with the short and controlled residence time in the membrane pores achieved by the flow-through mode, which prevents further oligomerization. After obtaining yields of the desired C_8 components close to 60 %, the authors assume that the selectivity towards these intermediate products can be further increased by controlling the residence time.

The dimerization of isobutene in an FTCMR is studied by Fritsch et al. (2004) applying polymer based composite catalytic membranes based on Nafion and other solid acid catalysts. The membranes are generated by deposition of a porous reactive layer on top of a porous polymeric tubular membrane with a diameter of 20 mm. The reactive layer with a membrane area of $2.54\,\mathrm{cm}^2$ is generated by mixing the catalysts in solution with a polymeric binder. The resulting catalyst mass is varied between 8.7 and 38.3 mg. The influence of different catalysts and different binders on conversion and selectivity are investigated concluding that all the parameters structure, porosity, catalyst partition and catalyst accessibility determine the final reactivity of the membrane. The experiments are performed in steady state by adjusting the reactant mass flows and flowing against normal pressure at the outlet, resulting in an inlet pressure around 4 bar depending on the structure of and thus the pressure drop across the membrane. The conversion of isobutene increases with the flow rate and thus with the built-up pressure up to values of 90 % without a significant change of selectivity to the dimer, which reaches around 14 %. It is assumed that the liquid products fill the membrane pores and require a certain flow to purge the pores from products and oligomers. For all catalysts the conversion improves by increasing the temperature in a range from 30 to 50 °C, whereas in most cases the selectivity decreases. The most suitable membrane is identified by plotting the conversion against the selectivity for all catalyst and binder combinations. High selectivities of

86 % are achieved for feasible conversions of 22 %. The authors discuss the difficulty of properly comparing the performance of membrane reactors with that of conventional reactors regarding parameters such as space time yield.

Three phase Fischer-Tropsch synthesis (CO hydrogenation to liquid hydrocarbons) in catalytic membrane reactors is investigated by Khassin et al. (Khassin, 2005; Khassin et al., 2005a,b). The most important requirements for this synthesis are stated to be an isothermal catalyst bed, high concentration of catalyst, high gas-liquid interface, small catalyst grains, low pressure drop and low water backmixing in the reactor. For traditionally used slurry bed reactors and circulating fluidized bed reactors the catalyst concentration is too low. In a fixed catalyst bed there is a conflict between hydraulic resistance and diffusion limitation, whereas for egg-shell catalysts the catalyst concentration in respect to the particle volume is rather low. Thus the authors suggest heat-conductive "plug-through contactor membranes" as a solution. The membrane is made up of a Co-Al co-precipitated catalyst. The pores with effective radius above 2 to 3 µm are gas-filled and referred to as transport pores, while the smaller pores are flooded with liquid products and not permeable. The space-time-yield achieved with the synthesized membranes ($200\,\mathrm{kg_{HC}/m^3h}$) is much higher than in traditional reactor designs for Fischer-Tropsch synthesis. To estimate the pore size distribution of the membranes the bubble-point method is applied, using a simplified model, which considers the pores as cylindrical holes. As a liquid phase fills the smaller pores and leaves only the larger pores permeable for gas flow, the capillary pressure compared to the pressure drop across the membrane is an important parameter for the membrane performance, which is sensitive for the gas flow direction. The width of the pore size distribution is responsible for the extent of gas flow bypass and the selectivity towards higher hydrocarbons decreases with the average pore distance. The latter observation is explained with internal diffusion constraints, which appear when the diffusion length between two adjacent transport pores is larger than 30 µm. The observed catalytic activity is up to three times higher than in a comparable slurry reactor. The produced cylindrical membranes with a diameter of 42 mm combine high permeability with high mechanical strength.

2.3.3 Selective Differential FTCMR

Partial hydrogenations of liquid reactants or in liquid phase are a reaction class of industrial interest. The reaction rate is often limited by the low solubility of hydrogen in the liquid. Thus low conversions argue against performing these reactions in a single pass integral reactor. An alternative that takes advantage of the intensive contact between reactants and catalyst caused by convective flow through the pores but also allows for higher total conversions is a discontinuous operation with a recycling and resaturation loop, forming a differential reactor. The continuously low concentration of hydrogen can reduce the rate of undesired side reactions, resulting in increased selectivities. This concept has been applied to the hydrogenation of nitrate in water and to the partial hydrogenation of several unsaturated liquid hydrocarbons.

Hydrogenation of nitrate in water

Ilinitch et al. (2000) perform the reduction of nitrate ions by hydrogen in water in three different reactor configurations. In a bed of Al_2O_3 supported Pd-Cu catalyst pronounced internal diffusion limitations are observed. Operating a catalytic membrane in absence of forced flow, the observed catalytic activity is also low. Forcing the flow of the reaction solution through the catalytic membrane with liquid recycling finally manages to minimize diffusion limitations and causes a multiple increase in catalytic activity. The membranes made of SiO_2/Al_2O_3-ceramics show a uniform macroporous structure with a pore diameter around 1 µm, a pore volume of 0.2 cm^3/g and a thickness of 4.8 mm. The active metals Pd and Cu are introduced by impregnation with aqueous metal salt solutions, followed by drying, calcination and reduction, resulting in a palladium content of 1.6 wt% and a copper content of 1.2 wt%. When comparing the specific catalytic activity of the membrane to the one of the conventional powder catalyst, the latter shows a higher value, evoking the assumption that the active material inside the membrane in the above discussed experiment is not fully utilized (Dittmeyer et al., 2004).

Catalytic macroporous polymeric membranes are applied to water denitrification in a flow-through operation mode to elucidate the reaction mech-

Table 2.3: Differential Flow-through Catalyic Membrane Reactors with liquid recycling for selective reactions (d_{pore} = Mean pore diameter; t_{cat} = Thickness of catalytic layer)

Authors	Reaction	Membrane	Catalyst	d_{pore} [nm]	t_{cat} [µm]
Ilinitch et al. (2000)	Water denitrification	SiO_2/Al_2O_3	Pd-Cu/γ-Al_2O_3	1 000	4 800
Ilinich et al. (2003)	Water denitrification	Macroporous PA MF	Pd / Cu / Pd-Cu	400	100
Reif (2004)	Water denitrification	Symmetric ceramic	Pd	3 000	1 500
Lüdtke et al. (1998)	Water denitrification	Microporous PEI	Pd-Cu/γ-Al_2O_3 incorporated	2	50-150
Schmidt et al. (2005)	Cyclooctadiene; 1-octyne; phenyl acetylene; geraniol part. hydrogenation	Porous PAA	Pd	130-380	1 000
Purnama et al. (2006)	α-methylstyrene part. hydrogenation	α-Al_2O_3	Pd, wet impregnation	1 900	1 000
Schmidt et al. (2008)	Cyclooctadiene part. hydrogenation	α-Al_2O_3	Pd, wet impregnation	600-3 000	500
Fritsch and Bengtson (2006a)	Sunflower oil partial hydrogenation	Porous polymer (PES, PAI)	Pt / Pd, impregn. / casting	3 900-9 000	130-230
Schmidt and Schomäcker (2007)	Sunflower oil partial hydrogenation	Porous α-Al_2O_3	Pd / Pt, wet impreg.	3 000	500

anism on bimetallic catalysts (Ilinich et al., 2003). Different catalytic membranes are prepared with either copper or palladium or both catalysts and their catalytic activity for the nitrate hydrogenation is compared. The reaction is performed in a batch process in a stirred reactor module with the catalytic flat sheet membrane and hydrogen feed as well as a buffer vessel with recirculation of the liquid reactants. The advantage of using a membrane reactor setup in comparison to a slurry reactor is the easy separation of two different catalytically active components, which is necessary for analytical purposes. The monometallic membranes show poor activity, whereas bimetallic membranes and stacks with both types of catalyst show the highest catalytic activity, supporting a hypothesis on a decisive role of hydrogen spillover in the reaction mechanism. The reaction rate is very low as long as no forced flow through the catalytic membrane takes place.

Reif and Dittmeyer compare the FTCMR concept for aqueous nitrate and nitrite reduction with the catalytic diffuser concept, in which the reactants are delivered from different sides of the membrane (Reif and Dittmeyer, 2003; Reif, 2004). Both setups induce active contact between the reactants and the catalysts, while only the FTCMR concept allows for the elimination of pore diffusion and very short contact times. Due to high pressure drops in the FTCMR mode conventional ceramic membranes with pore diameters of 100 nm in the active layer are found to be unsuitable. Consequently symmetric supports with pore diameters around 3 µm are coated with Pd. Flowing from the outside to the inside reduces plugging of the membrane. For the nitrite hydrogenation in FTCMR mode a significantly higher activity and a lower formation of ammonium is observed, both depending on the transmembrane flux (Dittmeyer et al., 2004; Schomäcker et al., 2005).

A similar but inherently different reactor setup is reported by Lüdtke et al. (1998). Nitrate in water is hydrogenated flowing through a catalytic membrane, while the water is saturated with hydrogen in a pressurized tank within a recycling loop. In contrast to the previous concepts, the catalytic membrane is operated in the cross-flow mode, such that the treated water is continuously removed after only a single pass through the membrane. Catalytic membranes with catalyst content up to 33 wt% are prepared by incor-

porating a powder-type Pd-Cu/γ-Al_2O_3 catalyst into polymeric ultrafiltration membranes. For relatively low transmembrane fluxes of 5 to 25 L/m^2h a more or less constant selectivity towards nitrogen of 80 % is observed during all experiments. The activities per unit area of the membrane up to 0.012 mol/m^2h are rather low. The moderate performance might be explained by assuming that a certain fraction of the catalyst particles is not accessible for the liquid travelling through the pores, being completely surrounded by the polymer matrix. Moreover the fluxes might still be too low to exploit the full kinetic potential of the catalyst.

Partial hydrogenation of hydrocarbons

For the partial hydrogenation of several unsaturated hydrocarbons Schmidt et al. (2005) use the differential FTCMR concept, naming it "pore-through-flow catalytic membrane reactor" and compare it to a slurry reactor and a fixed bed reactor. The FTCMR is constructed as a loop of a saturation vessel and a porous membrane made from cross-linked polyacrylic acid with palladium nanoparticles integrated as catalyst. Four different unsaturated reactants are investigated: Cyclooctadiene, 1-octyne, phenyl acetylene and geraniol. The liquid reaction mixture is resaturated with hydrogen up to 100 times. With the applied flow velocity of $2 \cdot 10^{-4}$ m/s the convection of the reactant stream is at least one order of magnitude faster than diffusion displacement, which is reported to be in the order of 10^{-5} m within 1 s. The prepared membranes with a thickness of 1 mm show pore sizes between 130 and 380 nm, porosities between 35 and 70 % and a Pd content of 15 mg which equals 1 wt%. The membranes are placed on a porous support plate in the reactor module. For the hydrogenation of octyne the desired reaction is much faster than the undesired reaction, such that little influence of mass transfer is observed. For phenyl acetylene and cyclooctadiene the desired reaction is still faster than the undesired one, but mass transfer is more significant, which can be seen in the increased selectivity obtained in membrane reactor and slurry reactor compared to the fixed bed reactor. For geraniol the reaction rates are nearly equal. For this reaction the membrane reactor reaches even

higher selectivities than the slurry reactor, whereas the activity is lower due to the strong decrease of hydrogen concentration during each pass through the membrane, such that the average hydrogen concentration is substantially lower than the saturation concentration.

Purnama et al. (2006) perform the partial hydrogenation of α-methyl–styrene to cumene in a catalytic membrane reactor impregnated with Pd. The measured productivity, defined as conversion per time and catalyst mass, in the flow-through reactor exceeds that of other types of membrane reactors as well as other conventional reactors, such as slurry, trickle-bed and bubble-column reactor. The tubular microporous α-Al_2O_3 membrane has a thickness of 1 mm and a pore size of 1.9 µm and is soaked in a solution of palladium acetate in toluene, reaching catalyst concentrations of 0.03 to 0.08 wt%. The optimum flow rate must be adjusted to the catalyst mass, such that the hydrogen conversion reaches 100 % exactly when the reactants leave the membrane.

The same reactor approach is applied to the hydrogenation of cyclooctadiene, reaching the same selectivities as in slurry experiments and outperforming the comparable fixed bed reactor (Schmidt, 2007). With the same Pd amount the membranes with smaller pores (0.6 µm) are more active than the membranes with bigger pores (1.9 or 3.0 µm). In an industrial cooperation the reactor is transferred from laboratory scale to pilot scale applying a 27-capillary catalytic membrane module. The obtained space time yields are much higher than those reported for conventional fixed-bed or trickle-bed pellet catalysts or slurry catalysts in bubble columns (Schmidt et al., 2008). Due to encouraging scale-up results this flow-through reactor setup is referred to as one of the most promising candidates for the first industrial application of catalytic membrane reactors (Caro et al., 2007).

Fritsch and Bengtson (2006a,b) develop catalytically active porous membranes for the selective hydrogenation of viscous liquids such as sunflower oil in a membrane reactor. The high viscosity and the low hydrogen solubility induce severe mass transfer limitations. Industrially vegetable oil hydrogenation takes place in stirred tank reactors with finely dispersed catalyst at temperatures between 170 and 200 °C at 2 to 5 bar of H_2 pressure. In

this process up to 50 % of the undesired trans-isomerized fatty acids are generated. By applying the FTCMR concept, the content of trans-isomers can be reduced while at the same time the immobilization of the catalyst inside the membrane pores avoids expensive filtration steps. Porous polymer membranes are prepared from polyethersulfone and polyamideimide with and without inorganic alumina filler. These membranes show high water fluxes of about 30 000 L/(m^2 h bar) and oil fluxes of 900 to 2 000 L/(m^2 h bar) at 60 °C. Catalyst is introduced by two different methods, either by wet impregnation of the membrane in a catalyst precursor solution followed by calcination and chemical reduction or by addition of ready-made supported catalysts to the membrane casting solutions. The catalytically activated membranes with Pt-contents between 0.1 and 1 g/m^2 are applied to hydrogenate refined sunflower oil. Within 6 hours about a half of the linoleic acid is hydrogenated, which is the major compound in sunflower oil triglycerides. Pt shows a similar activity to Pd catalysts and generates less trans-isomers. The membrane activity is stated to be sufficiently high to suggest the industrial use of FTCMR for the hydrogenation of viscous liquids.

Schmidt and Schomäcker (2007) also use a differential FTCMR for partial hydrogenation of sunflower oil in n-heptane as solvent and compare the reactor performance with that of a slurry reactor with powder catalyst. A porous α-Al_2O_3 membrane is impregnated with Pd or Pt as active catalyst. The membrane reactor reaches significantly lower contents of the fully hydrogenated stearic acid and higher contents of undesired trans-isomers.

2.4 Conclusions

The increasing number of publications dealing with catalytic membrane reactors in flow-through mode underlines the potential of this relatively new concept for performing heterogeneous reactions in both gas and liquid phase.

The parallels to microreactors are obvious: Small characteristic dimensions lead to improved heat and mass transfer. In catalytic membrane reactors the characteristic dimensions are even smaller than in microreactors, resulting in excellent heat transfer between fluid and membrane. However, in

contrast to microreactors, heat removal from the membrane is limited, such that isothermal operation in terms of equal feed and permeate temperature can hardly be realized for strongly exothermic reactions.

The mean pore size of the applied membranes varies by several orders of magnitude. The choice of the appropriate pore size always represents a trade-off between intensive contact and low pressure drop. Especially for gas phase reactions in pore structures below the micrometer scale improved understanding of the flow processes and microeffects in Knudsen and transition regime is required.

Integral reactors are almost exclusively applied for gas phase reactions. For the decomposition of volatile organic compounds the intensive contact accounts for complete conversion. Partial hydrogenation or partial oxidation reactions are performed in flow-through mode in order to benefit from the narrow residence time distribution in combination with the short contact time, allowing for high selectivities. It should be emphasized that in contrast to other membrane reactor concepts, using permselective membranes, the selectivities in FTCMR cannot exceed those of an ideal plug flow reactor.

Applications in liquid phase are still limited to hydrogenation reactions in differential reactor mode. Nevertheless in this field they have proven to be valuable and might be closer to industrial operation than their integral counterparts for gas phase reactions.

A comparison between the different investigated catalytic membrane reactors lacks sufficient data, as the operation parameters of the performed model reactions are tailored to the applied membranes and catalyst preparation methods. Several authors observe improved performance regarding catalytic activity and/or selectivity compared to conventional fixed bed reactors. Nevertheless the reactor concept requires more or less sophisticated catalytic preparation methods, frequently suffers from limited membrane stability and competes with other novel concepts such as microreactors or monolithic reactors. Furthermore the choice of the appropriate pore dimensions strongly depends on the intended application and the allowable pressure drop, preventing the establishment of general guidelines.

The investigations presented in the work at hand aim at the modelling and

application of anodized alumina membranes with very uniform pore channels for selective gas phase hydrogenations. These unique microstructures promise a very narrow pore size distribution and are also applied by Yamada et al. (1988), Pellin et al. (2005) and Mucherie et al. (2007). The pore structure made up of separate cylindrical channels calls for a more detailed investigation of flow regimes and temperature distribution inside the membrane and allows for comparing experimental results with reactor simulations.

Chapter 3

Experiments and Methods

This chapter discusses the three main factors determining the performance of a catalytic membrane reactor, namely membrane structure, catalyst and reactor setup. Section 3.1 describes the particular microstructures of the investigated ceramic membranes and quantifies the relevant geometric parameters. The subsequent Section 3.2 treats the deposition of catalytically active components in the pores of the ceramic membranes and correlates the amount and dispersion of catalyst to the deposition procedure. Finally Section 3.3 deals with the reaction experiments, explaining the applied model reactions as well as the experimental setup and analytics.

3.1 Ceramic Membrane Microstructures

Recently, inorganic materials gain importance for membrane production due to improved temperature and chemical resistance, as well as theoretically precise control of pore size and selectivity, compared to organic membranes (Melin and Rautenbach, 2007). Ceramics, mostly aluminium oxide, are the dominating material for inorganic membranes, other materials used are precious metals and alloys, various glasses and carbon. Limitations are mainly given by the brittle nature of the material, which calls for special module constructions. If operated at high temperatures, sealing between membrane and module is especially difficult due to different thermal expansion coeffi-

cients. Elaborate preparation methods of the membranes themselves, which are often produced in several steps, result in higher membrane costs.

3.1.1 Microstructure Generation

Preparation of ceramic membranes is possible by several methods. The most common methods are based on sintering small ceramic particles at high pressures and temperatures. A different microstructure can be achieved by controlled anodization of thin aluminium sheets. The characteristics of the resulting microstructures are shortly presented in the following, with a focus on the anodization procedure.

Sintered Ceramic Membranes

Sintering of fine metal or ceramic powders results in a solid porous symmetric structure, resembling a packed bed of microparticles. The main geometric characteristics pore size distribution, porosity and tortuosity strongly depend on the properties of the powder used. Pore size distributions are often rather wide and tortuosities in the range of 2 to 2.5 are reported (Melin and Rautenbach, 2007). Symmetric porous membranes are either used for microfiltration applications or as support for microporous layers. The resulting asymmetric porous membranes are designed to allow for a pin-hole free separation layer combined with low hydraulic resistance and mechanical stability.

For the experiments performed with sintered ceramic membranes, two different types of alumina membranes supplied by Kerafol are employed. One of them is symmetric, consisting only of a support layer, whereas the other type is asymmetric, featuring an additional layer on top of the support. The main characteristics of the two membranes and the identifiers applied in the work at hand are summarized in Table 3.1.

Anodized Alumina Membranes

In the 1920s Bengough and Sutton (1926) discover that aluminium and its alloys can be protected from corrosion by means of anodic oxidation. In this electrochemical process, aluminium is turned into an anode by immersing it

Table 3.1: Membrane specifications according to supplier

Identifier	W01	W02	K02	K20
Supplier	Whatman	Whatman	Kerafol	Kerafol
Pore size active layer / µm	0.1	0.2	0.2	2.0
Pore size support / µm	0.2	0.2	2.0	2.0
Membrane thickness / µm	60	60	2 000	2 000
Membrane diameter / mm[a]	43	43	47	47
Approx. membrane mass / g	0.1	0.1	7.6	7.6

[a]Diameter of Whatman membranes incl. supporting PP-ring 47 mm

in a chromic acid bath and applying electric current between the aluminium and a carbon cathode. After a while, the aluminium becomes coated with a semi-opaque gray film. Keller et al. (1953) investigate aluminium oxide layers generated by anodic oxidation and find close-packed hexagonal cells of oxide, containing a single pore each. The pore size can be manipulated by the choice of electrolyte, whereas wall thickness and barrier thickness are primarily a function of the forming voltage. A model for describing the self-regulating pore growth, based on the distribution of the electric field in the pore tips, is given in the 1970s, explaining why the pores grow and why their size distribution is so narrow (Jessensky et al., 1998). Smith (1973) develops a process for removing the thin barrier layer, generating uniform porous membranes from aluminium foils. The best results for removing the unanodized aluminium are achieved by etching from the opposite side. These membranes are commercially produced for laboratory filtration since 1986 by Anotec Separations (Bhave, 1991), currently available as Whatman Anodisc. Rigby et al. (1990) compare the preparation by sulfuric, oxalic, phosphoric and chromic acid and predict a significant growth of applications of the produced membranes.

The process of anodic oxidation allows for precisely controlled narrow pore size distributions. The resulting structure is formed by cylindrical slightly conical pores perpendicular to the macroscopic membrane surface. The method only produces unsupported membrane foils with low mechanic stability. For most applications a support is required (Bhave, 1991). The

preparation procedures are further improved by adding a pretexturing treatment, allowing for generation of completely isoporous membranes for sophisticated applications (Masuda et al., 1997; Li et al., 1998).

Wießmeier and Hönicke (1996) apply the process of anodic oxidation to increase the specific surface of microstructured devices for catalytic applications, creating a flow-through microreactor with dead-end pores on the channel walls.

The experiments performed in the work at hand employ two types of the commercially available membranes Whatman Anodisc 47. Their main characteristics and the applied identifiers are summarized in Table 3.1.

3.1.2 Microstructure Characterization Methods

Several analytic methods are applied to gather information about the membrane microstructure, such as pore sizes distributions, porosities and specific surface. The methods are described in the following.

Scanning Electron Microscopy

Scanning electron microscopy (SEM) produces images with high magnification and can resolve details down to the scale of the wavelength of visible light. Analyses are performed at the Central Facility for Electron Microscopy, RWTH Aachen University (GFE) by means of a ZEISS DSM 982 Gemini with field emission gun. The method is suitable for measuring the membrane layer thickness as well as the shape and size of the straight single macropores ($d_\mathrm{p} > 0.05\,\mu\mathrm{m}$). Due to the regular pore structure, image processing can be used to calculate a pore size distribution from a top view of the membrane.

The pore size distribution is determined by applying the image processing tool OZELLA, developed at the Institut für Kunststoffverarbeitung an der RWTH Aachen (IKV) (Peters, 2004), to the top view SEM image of the membrane. OZELLA identifies connected dark pixels and interprets them as cells. The respective cell size is calculated from the number of connected pixels. Figure 3.1 shows a detail of the upper-left corner of an SEM image processed with OZELLA, highlighting the determined cell sizes in shape of

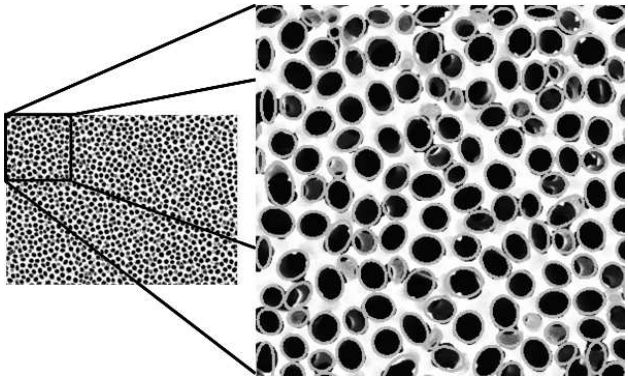

Figure 3.1: Detail of pore size characterization performed with image processing tool OZELLA

ellipses. As can be seen, errors occur at the image edges and in regions of low contrast. These are corrected manually by duplicating the sizes of the edge cells and partitioning misinterpreted large cells into two half-sized single cells. The membrane porosity is calculated simply by dividing the number of cell pixels by the total number of pixels.

Mercury Porosimetry

Mercury porosimetry is the most frequently applied method for determining the open pore volume of porous materials. Due to its high surface tension, mercury does not intrude into the pores if no pressure is applied and does not interact with the pore surface. For cylindrical pores, the size of the intruded pores is correlated to the applied pressure according to the Young-Laplace equation:

$$d = -\frac{4\sigma \cos(\alpha)}{p}, \tag{3.1}$$

with a surface tension of 0.485 N/m and a contact angle of $\alpha = 130°$. The analysis is performed at the Institut für Bauforschung der RWTH Aachen (ibac) with the mercury porosimeter AutoPore IV 9220, using a maximum pressure of 413 MPa, corresponding to a minimum pore diameter of 3 nm.

BET Surface Measurement

The specific surface of the Whatman Anodisc membranes is calculated applying the method of Brunauer et al. (1938), based on a measurement of the adsorption isotherm, commonly known as BET method. The analysis is performed at the Lehrstuhl für Technische Chemie und heterogene Katalyse der RWTH Aachen (TCHK), applying a Micromeritics ASAP 2000 (Accelerated Surface Area and Porosimetry analyzer) to five differently prepared samples of W02 membranes, both coated with catalyst and uncoated.

Permeance Measurements

Correlating the pressure drop across the membrane with the corresponding flux or flow rate allows for determination of geometric parameters. The permeance method applied in the work at hand is based on the pressure drop across the membrane caused by convective flow through the pores and produces mean pore size and porosity rather than a pore size distribution. It is nondestructive and can be performed immediately before reaction experiments with the same setup. Plotting the measured membrane permeance P_{tot} under variation of the average absolute pressure in the pore p_{av} yields a straight line (Figure 3.2), which can be characterized by the following equation:

$$P_{\text{tot}} = \alpha + \beta \cdot p_{\text{av}} \tag{3.2}$$

$$\alpha = 1.06 \frac{\epsilon \cdot r}{\tau L \sqrt{MRT}} \tag{3.3}$$

$$\beta = 0.125 \frac{\epsilon \cdot r^2}{\tau L \eta RT} \tag{3.4}$$

The axis intercept α at $p = 0$ represents the pressure independent contribution of Knudsen diffusion to the total permeance, whereas the region above this value represents the convective contribution, which is proportional to pressure p_{av} and slope β (Lin and Burggraaf, 1991; Pina et al., 1996; Zalamea et al., 1999). The geometric parameters mean pore size and porosity can be calculated by means of a flow model according to Equations 3.3 and

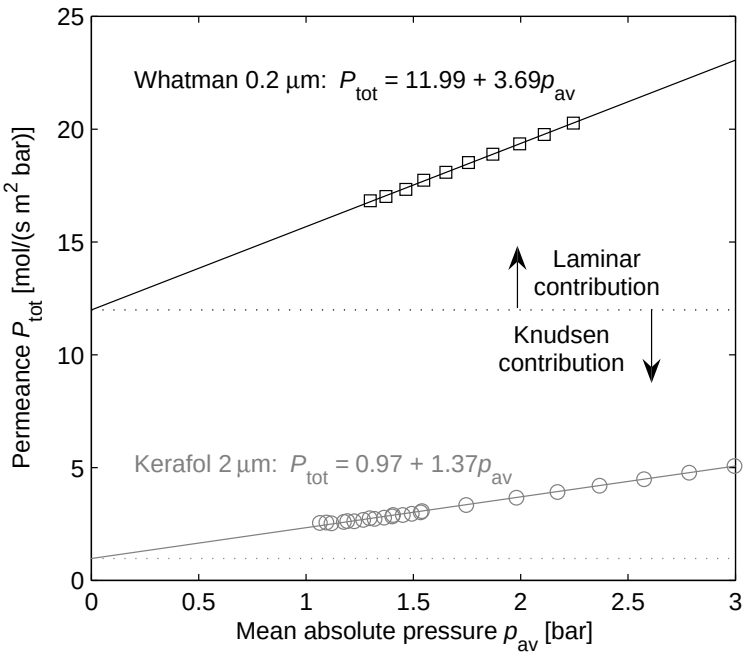

Figure 3.2: Membrane permeance as function of mean pressure for W02 membrane and K20 membrane: Pressure independent Knudsen contribution and pressure dependent laminar contribution

3.4. For details on the theory of gas microflows and the derivation of these equations, please refer to Subsection 4.2.1.

3.1.3 Results

The microstructure of the investigated membranes is characterized by means of SEM imaging, pore size distribution and the overall parameters mean pore size, specific surface and porosity.

SEM images of Whatman Anodisc membranes are given in Figure 3.3. The top view image of a W02 membrane with a nominal pore diameter of 0.2 µm at a magnification of 10 000 (Fig. 3.3(a)) illustrates the regular arrangement of open pore channels and the rather narrow size distribution. The cross section of a W01 membrane with a nominal pore diameter of 0.1 µm at a magnification of 1 000 (Fig. 3.3(b)) demonstrates different structural aspects: The nominal diameter can only be found in the thin active layer at

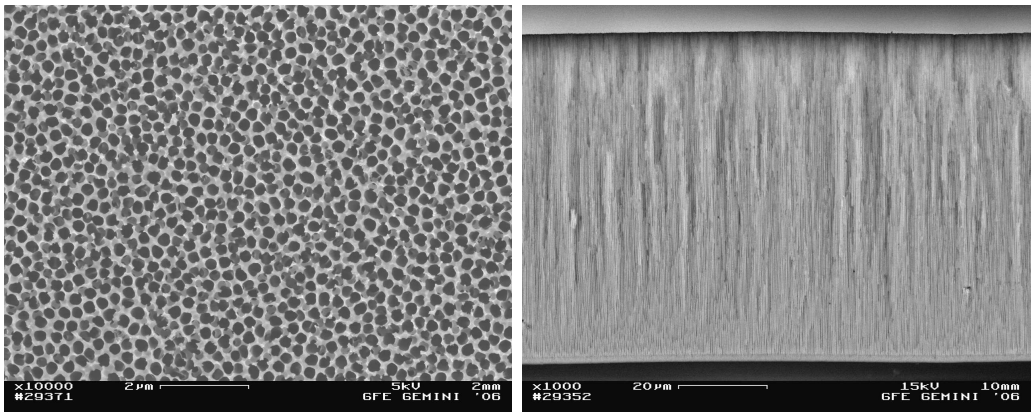

(a) Top view of W02 membrane, 10 000x magnification

(b) Cross section of W01 membrane with active layer at the bottom, 1 000x magnification

Figure 3.3: SEM images of Whatman Anodisc membranes

the bottom, whereas the main part is made up of channels with diameters around 0.2 µm. The pores are straight and arranged perpendicular to the surface without bifurcations. Moreover, they are slightly cone-shaped rather than exactly cylindrical. The thickness of the commercially available membranes varies. The illustrated sample shows a thickness of 80 µm rather than 60 µm as given in the specifications by the supplier.

Mercury porosimetry is performed with a sample of 16 finely ground W01 membranes (Figure 3.4). As more than 90 % of the total mercury volume intrudes into the sample, the measurement does not allow for determination of a valid pore size distribution. 60 % of the mercury volume is needed to fill the gaps between the ground membrane particles with corresponding diameters larger than 90 µm. A plateau is reached in the pressure range between 0.7 and 3.5 MPa with an intrusion volume around 75 %, signifying that no pores with diameters between 3.15 and 0.35 µm are present in the sample. The full volume of mercury is depleted at a pressure of 5.5 MPa, corresponding to a pore diameter of 0.23 µm. Smaller pores are not detected due to lack of mercury. Thus the only valid result is the maximum pore size of about 0.35 µm.

The pore size distribution obtained by the image processing tool OZELLA

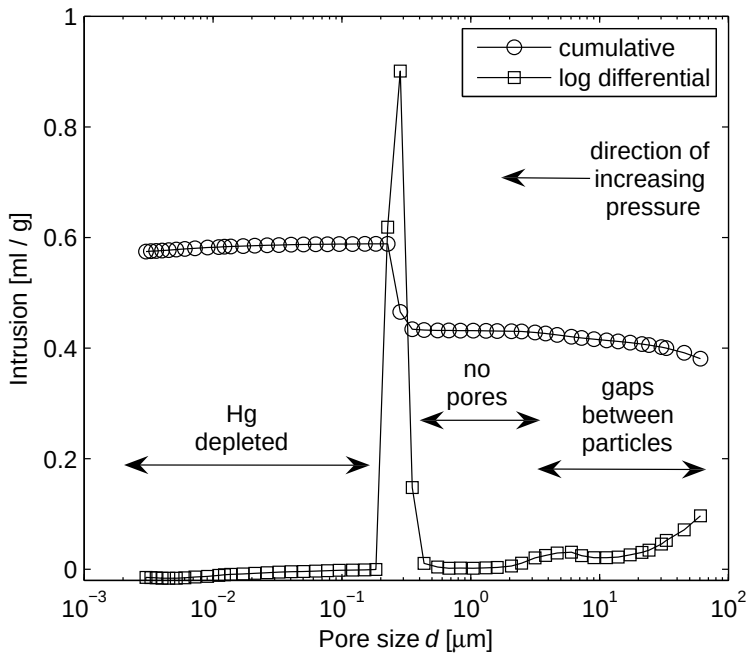

Figure 3.4: Measured mercury porosimetry intrusion curve for W01 membranes

is illustrated in Figure 3.5. The resolution of the density function is arbitrarily chosen to steps of 10 µm resulting in 17 pore size classes. The pore sizes range from 0.15 to 0.32 µm with a mean pore size of 0.235 µm and a porosity of $\epsilon = 0.53$. Regarding the maximum detected pore size, the agreement with the mercury porosimetry measurement is good.

The volume-specific surface S_V of a membrane consisting of N cylindrical channels with a surface of πdL each, can be calculated from mean pore size d and porosity ϵ according to

$$S_\mathrm{V} = \frac{N \cdot \pi dL}{V_\mathrm{mem}} = \frac{4\,\epsilon}{d}. \tag{3.5}$$

Division by the bulk density yields the mass-specific surface. The resulting characteristic parameters of a W02 membrane, calculated from mean pore size and porosity as determined by OZELLA assuming isoporous cylindrical geometry, are summarized in Table 3.2.

The BET measurements of different anodized membranes are given in

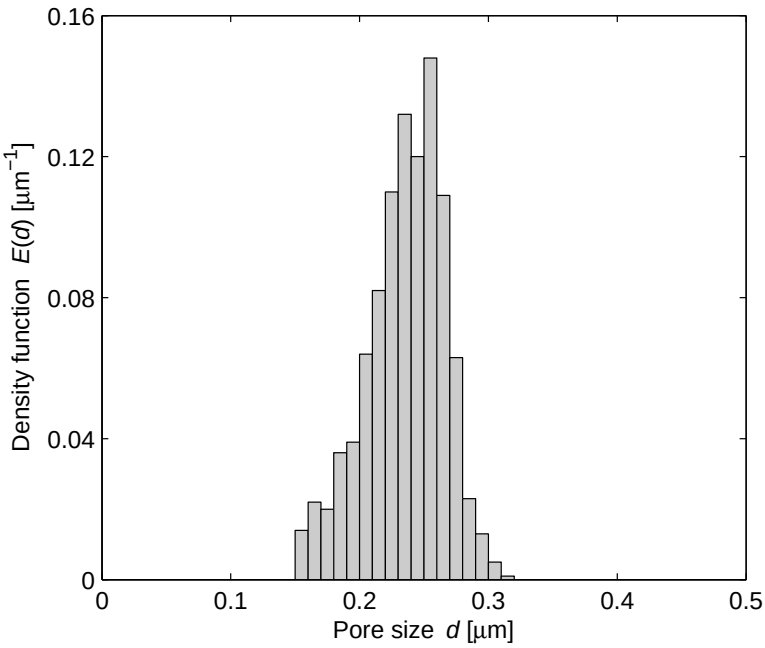

Figure 3.5: Pore size distribution of W02 membrane as determined by the image processing tool OZELLA from SEM top view image

Table 3.2: Summary of geometric parameters of a W02 membrane determined from SEM image processing data

Parameter	Value	Unit
Mean pore size	0.235	μm
Minimum pore size	0.15	μm
Maximum pore size	0.32	μm
Porosity	0.53	-
Membrane mass	0.108	g
Membrane bulk volume	$8.71 \cdot 10^{-8}$	m^3
Bulk density	1 239	kg/m^3
Volume-specific surface	$9.13 \cdot 10^{6}$	m^2/m^3
Mass-specific surface	7 368	m^2/kg
Pores per membrane	$1.79 \cdot 10^{10}$	-

Table 3.3: BET surfaces of Whatman Anodisc membranes with and without deposited catalyst

Sample	BET-surface m^2/kg
W01-6[a]-1[b]	7 450
W01-6-10	7 410
W02	7 630
W02-6-10	7 510

[a]concentration of precursor solution 6 $g_{Pd(acac)_2}/l$
[b]impregnation time 1 min

Table 3.3. The four measurements all show BET surfaces around 7 500 m^2/kg which is in excellent agreement with the mass-specific surface of 7 368 m^2/kg calculated by means of Equation 3.5. Neither an influence of the nominal pore size can be detected, nor of the amount of catalyst in the pores. The first observation can be explained by the geometric structure of the different membrane types. Both W01 and W02 membranes consist of straight channels with pore sizes around 0.2 µm. The nominal pore size of 0.1 µm for the W01 membranes only describes a very thin separation layer on top of the straight channels with negligible influence on the specific surface. Catalyst deposition does not significantly increase the specific surface of the membranes. The adsorption isotherms prove the absence of micropores below 10 nm.

The employed ceramic Kerafol membranes are illustrated in Figure 3.6. At a magnification of 40 (Fig. 3.6(a)), the orderless homogeneous structure of the support material is visible. At higher magnifications of 3 000 (Fig. 3.6(b)), the active layer with a continuous thickness of about 20 µm already illustrates that the particle size distribution of the precursor material results in an inordinate structure with remarkable tortuosity compared to the straight channels of the anodized membrane. In the support layer the same effect is even more pronounced.

Permeance measurements are performed for the three different membrane types W02, K20 and K02 before catalyst deposition. The parameters d (mean pore size) and ϵ/τ (porosity/tortuosity) calculated from the permeance experiments according to Equation 3.2 are summarized in Table 3.4.

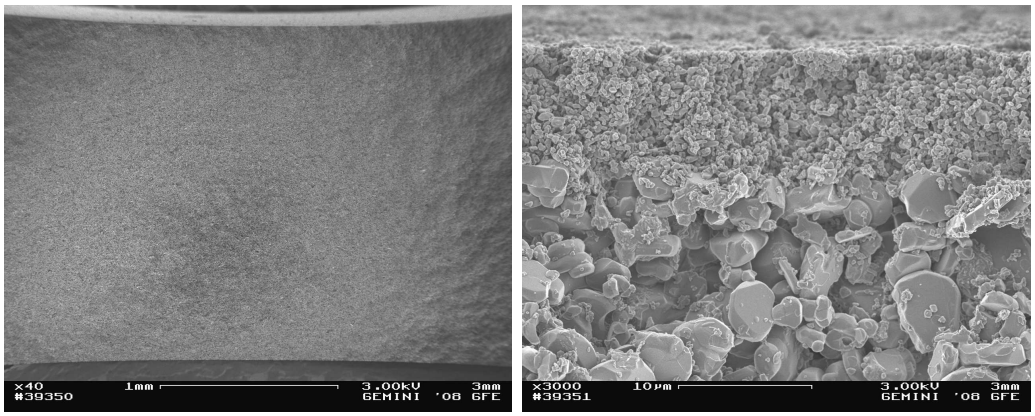

(a) Cross section with active layer at the top, 40x magnification

(b) Close-up of active layer, 3 000x magnification

Figure 3.6: SEM images of a K02 membrane

The permeance method produces consistent membrane parameters with low variation between different samples of the same membrane type. For the W02 membrane, the tortuosity τ should be equal to 1 due to the straight channel geometry. The resulting porosities around $\epsilon = 0.4$ are somewhat smaller than the one calculated from the SEM image $\epsilon = 0.53$. The mean pore size of around $d = 0.27\,\mu\text{m}$ on the other hand slightly exceeds the SEM value of $d = 0.235\,\mu\text{m}$. The sintered K20 membranes show lower values of ϵ/τ. The porosity calculated from a measured bulk density of $2\,200\,\text{kg/m}^3$ amounts to $\epsilon = 0.44$. In combination with the calculated values of ϵ/τ the resulting tortuosity is in the range between 1.8 and 2. The K02 membranes show apparently higher porosities and lower mean pore sizes than the K20 membranes. This can be explained by the fact that the calculation is based on a symmetric membrane. The thin active layer is not accounted for in the membrane thickness, resulting in a mean pore size and porosity for an equivalent symmetric membrane.

3.2 Catalytic Activation

Before the ceramic membranes can be employed for hydrogenation reactions, catalytically active material needs to be deposited in the membrane pores.

Table 3.4: Permeance parameters α and β and resulting membrane parameters ϵ/τ and d for non-catalytic membranes

Membrane	α^a	β	ϵ/τ	$d/$ µm
K20	0.99	1.38	0.24	1.261
	0.95	1.38	0.23	1.308
	0.97	1.37	0.24	1.273
K02	1.03	1.30	0.28	1.139
	1.06	1.30	0.30	1.109
	1.00	1.30	0.27	1.165
	0.91	1.13	0.25	1.123
	0.93	1.14	0.26	1.102
W02	11.99	3.69	0.40	0.277
	10.94	3.17	0.39	0.261
	12.05	3.73	0.40	0.279

[a]Compare Equation 3.2 and Figure 3.2

In this section the applied deposition procedure is described, the amount of catalyst deposited in the membrane is quantified and the catalytic activity is correlated to the deposition procedure.

3.2.1 Catalyst Deposition on Ceramic Supports

The preparation of supported catalysts usually involves three steps (Lee and Aris, 1985):

- Deposition of active components on the support (wet or dry impregnation),
- Evaporation of the liquid solvent (drying),
- Calcination and reduction of the catalyst (thermotreatment).

Catalyst precursors are compounds, such as organic salts, which contain noble metals. The support is submerged into a solution of precursor in water or organic solvents. In the case of wet impregnation, the support is prewetted by the liquid solvent before addition of the catalyst precursor. Thus, the catalyst distribution in the support is controlled by diffusion and adsorption. During dry impregnation, the dry support is directly immersed in the

precursor solution with the result that solvent and metal penetrate into the pores mainly due to capillary forces. (Neimark et al., 1981)

The resulting catalyst profile in the support is influenced by a combination of both impregnation and drying step . For weak and moderate adsorption, the impregnation time required for dry impregnation is much shorter than for wet impregnation and the final metal profiles are mainly determined by the drying step (Liu et al., 2008). For strong adsorption on the other hand, dry and wet impregnation are both determined by diffusion, resulting in similar behavior, and the effect of impregnation on the final metal distribution is pronounced.

After impregnation, the support is removed from the solution and solvent remaining in the pores is evaporated. In this drying step, the solvent is transported towards the external surface of the support due to capillary flow, while the dissolved catalyst precursor is transported by diffusion and liquid convection (Lekhal et al., 2001). Uniform profiles can be obtained by increasing metal diffusion.

In the final step the catalyst is calcined and activated, usually by reducing the metal oxide in hydrogen atmosphere, to obtain the noble metal in elemental state. This process does not affect the metal distribution, unless excessive heating causes agglomeration and sintering of the fine metal particles.

Boitiaux et al. (1983) describe the preparation of highly dispersed Pd catalysts on low surface area α-alumina as well as high surface γ-alumina by wet impregnation, using palladium acetylacetonate $Pd(acac)_2$ as precursor. The size of the metal particles is determined to be smaller than 1 nm. Variable parameters for preparation are precursor concentration and impregnation time. The precursor concentration is limited by the solubility of the precursor in the solvent. Boitiaux et al. (1983) apply benzene as solvent but report identical results for methylene chloride and carbon tetrachloride. Goetz et al. (1995) use the same solution but different ceramic supports and increase the impregnation time from 48 to 72 hours. Maximum dispersion of catalyst particles is achieved by calcination in air at 300 °C, at higher temperatures the particle size increases due to sintering (Boitiaux et al., 1983). Both authors

Table 3.5: Catalyst loading achieved by wet impregnation of aluminium oxides using $Pd(acac)_2$ as precursor as function of specific surface of support and concentration of precursor solution

		Solution g_{Pd}/l		
		0.70	1.45	3.33
Author	Support m^2/g	Loading g_{Pd}/g_{mem}		
Boitiaux et al. (1983)[a]	9	0.12	0.15	0.23
Goetz et al. (1995)[b]	10	0.09	0.20	0.30
Boitiaux et al. (1983)	69	0.39	0.43	0.50

[a]impregnation time 48 h, catalyst loading interpolated
[b]impregnation time 72 h

agree that increasing the precursor concentration in the catalyst solution increases the catalyst load in the support. Analogously the catalyst load is a strong function of the specific surface of the ceramic support (Table 3.5).

Reif (2004) observes problems during the wet impregnation of chemically inert ceramic membranes. During the drying process agglomeration can lead to formation of larger crystals. In experiments with palladium-salt-solutions ($Pd(NO_3)_2$, $PdCl_2$) precipitation of the catalyst is non-uniform and insufficient fixation results in low catalytic activity. Control of the deposition position in an asymmetric membrane is not possible with the impregnation method, leading to a waste of catalyst in the macroporous support layer.

Alternative preparation methods are generally more sophisticated. Coating with metal nanoparticles is not suitable as the available particles are already larger than 0.1 µm, leading to large metal clusters with inappropriately small specific surfaces (Reif, 2004). Chemical vapor deposition of metals represents an established method for depositing thin films. Reif (2004) develops a procedure for catalytic preparation of ceramic supports starting with a pretreatment of the support using white vaseline as organic solubilizer. The metal-organic precursor palladium(II)-hexafluoracetylacetonate and the pretreated support are introduced in a glass pipe which is subsequently evacuated to 500 mbar and heated to 80 °C, sublimating on the pretreated support

surface. This method allows for deposition efficiencies of 60 to 90 % and directed deposition limited to the pretreated surfaces.

Applied Catalyst Deposition Procedure

In the work at hand, satisfying results are achieved with the dry impregnation method. Thus, no investigation of further preparation methods is required. The following procedure is applied in for the catalytic activation of the ceramic membranes.

Palladium acetylacetonate $Pd(acac)_2$ (Merck-Schuchardt) solved in toluene is used as precursor solution. $Pd(acac)_2$ is a fine crystalline yellow powder which thermally degrades at a temperature of 190 °C (Merck-Schuchardt, 2006). At room temperature it is insoluble in water, but soluble in chloroform or toluene. Toluene evaporates at a temperature of 111 °C. The solubility of $Pd(acac)_2$ in toluene is determined to 6 g/l which corresponds to 2.1 g_{Pd}/l.

The catalyst is deposited in the ceramic membranes according to the following procedure:

1. Removal of supporting polypropylene ring by complete oxidation in air at 450 °C for 2 h (only applicable for Whatman membranes).
2. Preparation of a solution with desired concentration of $Pd(acac)_2$ in toluene.
3. Filtration of catalyst solution with a syringe filter to remove unsolved catalyst precursor.
4. Measurement of catalyst concentration in the solution by UV-vis.
5. Measurement of the mass of catalyst solution applying an analytical balance (accuracy 0.1 mg).
6. Impregnation of ceramic membrane in catalyst solution for desired impregnation time, using a closed recipient to reduce solvent evaporation.
7. Repeated measurement of the mass of catalyst solution to account for evaporation loss.
8. Repeated measurement of catalyst concentration in the solution to calculate amount of deposited catalyst.
9. Evaporation of solvent from prepared membrane at 120 °C for 30 min.

10. Calcination of prepared membrane in air at 300 °C for 2 h.
11. Installation of calcined membrane in reactor module.
12. Catalyst activation by reduction in hydrogen flow at 100 °C for 20 min.

The sample names are constituted of the membrane identifier K20, K02 or W20, followed by a hyphen and the concentration of the precursor solution in $g_{Pd(acac)_2}/l$ with applied values of 2, 4 or 6. After the second hyphen a numerical value specifies which of three tested impregnation times is applied with values of 1 corresponding to 1 min, 10 corresponding to 10 min and 24 corresponding to 24 h.

3.2.2 Characterization of Catalyst Loading

Several analytic methods are applied to determine the amount of catalyst deposited in the membrane pores directly or indirectly. The change of the catalyst concentration in the precursor solution during wet impregnation is monitored by means of UV-vis spectrometry and an analytical balance, allowing for indirect determination of the catalyst loading. X-ray diffractometry (XRD) and inductively coupled plasma optical emission spectrometry (ICP-OES) of catalytic membrane samples are performed to directly quantify the amount of catalyst in the membrane. Energy dispersive X-ray analysis (EDX) allows for the spatially resolved detection of elements in different regions of the membrane. Flow-through reaction experiments are performed to characterize the catalyst loading by correlating it with achieved conversions.

UV-vis Spectrometry of Precursor Solution

The precursor solution of $Pd(acac)_2$ in toluene shows an intensive yellow color. This allows for concentration measurement by means of UV-vis spectrometry. Light absorption at a wavelength of 420 nm is measured by means of a Cary 50 Bio UV-Visible spectrophotometer. Calibration with four solutions of different concentrations yields a linear correlation between concentration and absorption signal. Samples of the precursor solution are analyzed before and after each impregnation step, measuring also the mass of the

residual solution. The total mass of catalyst deposited on the membrane is calculated by balancing mass and concentration of the precursor solution, accounting for loss of solvent by impregnation and evaporation.

X-ray Diffractometry

X-ray diffractometry (XRD) allows for the identification of elements in crystalline state and determination of the crystallite sizes, provided that the quantity fraction in the sample is sufficient. Five samples with different amounts of catalyst are investigated at the Department of Chemical Technology and Heterogeneous Catalysis at the RWTH Aachen University (TCHK) with a Siemens D5000 diffractometer. The obtained diffractograms show no distinguishable maxima, not allowing for any characterization. Neither aluminium nor oxygen or even palladium reflexes can be determined. A detection limit of $2\,\mathrm{wt} - \%$ prevents the application of this method for characterizing the catalyst content of ceramic membranes.

Energy Dispersive X-ray Analysis

Energy dispersive X-ray analysis (EDX) detects local concentrations of single elements on or in a sample, allowing for determination of a spatial catalyst distribution. The EDX analyses are performed at the Central Facility for Electron Microscopy of the RWTH Aachen University (GFE) using an Oxford Link ISIS system with High Purity Germanium-Detector integrated in the SEM setup described earlier. Samples for SEM analyses are commonly prepared by sputtering the surface with palladium. If the amount of the palladium in the catalytic membrane is to be quantified, the sample needs to be prepared with carbon instead of palladium, reducing the depth of sharpness of the resulting SEM image.

In initial analyses, at the top and bottom of a catalytic membrane higher signals than in the center were obtained, concluding non-uniform catalyst distribution along the pores. Further measurements prove that these signals were caused by clearly visible larger catalyst particles that settle on top of the membrane during a temporarily applied impregnation procedure, which

uses a saturated catalyst solution with dispersed particles. EDX signals close to the edges always include signals from the top or bottom of the membrane. In repeated experiments with the improved catalyst deposition procedure with both Anodisc and Kerafol membranes, the palladium concentration is below the detection limit in all locations. Lacking contrary proofs, a uniform catalyst distribution is assumed for the symmetric membranes.

Inductively Coupled Plasma

The elemental analysis of catalytic membrane samples performed by inductively coupled plasma optical emission spectrometry (ICP-OES) determines the catalyst loading of the membranes. ICP-OES measurements are performed at the Department of Chemical Technology and Heterogeneous Catalysis at the RWTH Aachen University (TCHK) and at the Institute for Process Metallurgy and Metal Recycling at the RWTH Aachen University (IME).

As the elemental analysis is performed in liquid phase, a complete dissolution of the sample is crucial. Two different digestion procedures are performed, followed by a repeated determination of the palladium concentration. In the digestion procedure performed at the TCHK, 30 mg of sample are solved in 8 ml water, 2 ml concentrated sulfuric acid and 40 ml of hydrofluoric acid. At the IME a high pressure microwave digestion is performed using 2 ml water, 4 ml concentrated sulfuric acid and 4 ml hydrofluoric acid for 50 mg samples of the Anodisc membranes. For the Kerafol membranes 1 g of sample is dissolved in 5 ml sulfuric acid and 5 ml hydrofluoric acid, as low catalyst concentrations are anticipated. The dissolved samples are topped up to 50 ml using deionized water.

Both procedures are compared for two samples of the same catalytic Anodisc membrane, yielding 0.093 % Pd with the IME method compared to 0.048 % with the TCHK method. It can be concluded that complete dissolution is not achieved without high pressure microwave digestion.

Table 3.6: Permeance parameters α and β and resulting membrane parameters ϵ/τ and d for catalytic membranes.

Membrane	α^a	β	ϵ/τ	$d/\,\mu\text{m}$
K20[b]	0.97	1.38	0.24	1.281
K20-2[c]-10[d]	0.81	1.24	0.18	1.385
K20-6-10	0.80	1.25	0.18	1.402
K20-6-10	0.78	1.24	0.17	1.428
K02	0.98	1.23	0.27	1.128
K02-2-10	0.85	1.24	0.20	1.314
K02-6-10	0.78	1.12	0.19	1.287
W02	11.66	3.53	0.40	0.272
W02-2-10	10.76	3.66	0.33	0.306
W02-2-24	8.17	2.68	0.26	0.296
W02-4-10	8.91	3.19	0.26	0.322
W02-4-24	8.41	2.89	0.25	0.310
W02-6-10	8.12	2.96	0.23	0.328
W02-6-24	7.57	2.91	0.20	0.346

[a]Compare Equation 3.2 and Figure 3.2
[b]Mean values from Table 3.4 for non-catalytic membranes
[c]concentration of precursor solution 2, 4 or 6 $g_{Pd(acac)_2}/l$
[d]impregnation time: 10 min or 24 h respectively

3.2.3 Results

Catalyst is deposited in several membranes of the types W02, K02 and K20 according to the procedure described above.

Indirect proof of catalyst concentration is given by comparing the permeance measurements before and after catalyst deposition (Table 3.6). As explained in Subsection 3.1.2, the parameters apparent pore size d and apparent porosity ϵ/τ are determined from the experimental data by means of the fluid dynamic model given in Equation 3.2 and are at least for non-catalytic anodized membranes in good agreement with SEM analysis. In Figure 3.7 the resulting apparent pore size and porosity are displayed as a function of the precursor concentration. The differences between the parameters determined for the non-catalytic membranes and those determined for the catalytic membranes demonstrate that the pore microstructure is in deed affected by the catalyst deposition.

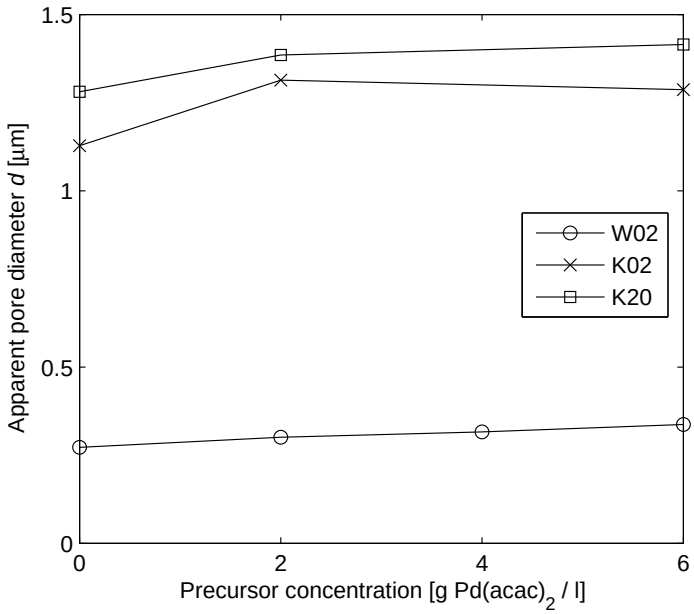

(a) Apparent pore diameter d as function of precursor concentration

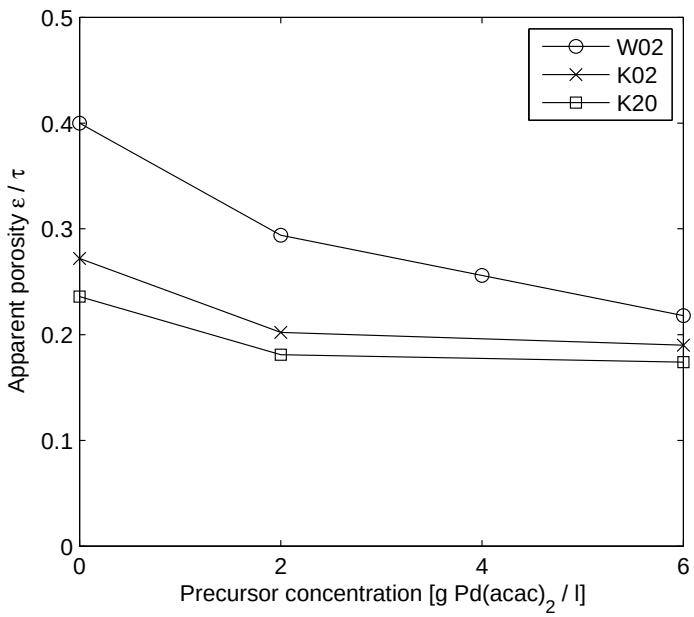

(b) Apparent porosity ϵ/τ as function of precursor concentration

Figure 3.7: Catalytic membrane parameters determined from permeance measurements by means of a flow model for transition regime

The α values represent the axis intercept of the permeance plots corresponding to the Knudsen contribution to the total permeance (Figure 3.2). Surprisingly, these values decrease after catalyst deposition, which coincides with increasing apparent pore diameters. The observed reduction of the apparent porosity during catalyst deposition by trend matches the physical expectations, although to an unexpected degree. Comparing the different impregnation times (Table 3.6), no conclusive influence can be determined. In all cases the apparent porosity decreases at longer impregnation time, but the apparent pore diameter either decreases or increases.

The influence of the precursor concentration is more obvious (Figure 3.7). For the W02 membrane a linear increase of the apparent pore diameter as a function of the precursor concentration is observed. The K02 and K20 diameters also increase with precursor concentration, although based on a limited number of experimental points. A strong porosity decrease is observed at low precursor concentrations, extenuating towards higher concentrations. Assuming constant tortuosity, the porosity decrease can be converted to a theoretical catalyst volume fraction in the membrane pores

$$\zeta_{\text{cat}} = \frac{V_{\text{cat}}}{V_{\text{pore}}} = 1 - \frac{\epsilon_{\text{cat}}}{\epsilon_{\text{noncat}}}. \tag{3.6}$$

For the W02 membrane this theoretical catalyst volume reaches values of up to 45 % of the total pore volume after catalyst deposition with a precursor concentration of 6 $g_{Pd(acac)_2}$/l. The real catalyst volume is presumably smaller than this theoretical value, as a part of the decrease can be contributed to increased tortuosity, generated by catalyst particles adhering to the pore walls.

On the other hand, the continuous increase of the apparent pore diameter, determined by combining the permeance measurements with a fluid dynamic model, lacks a physical explanation, as a decreasing pore size should be expected when catalyst is deposited on the pore walls. The values may be explained as correction for the overestimated porosity decrease. The flow resistance increases during catalyst deposition, resulting in an increased transmembrane pressure drop. The dramatically reduced apparent porosi-

Table 3.7: Catalyst loading determined by UV-vis of precursor solution and by ICP-OES of catalytic membrane samples

Sample	m_{mem} mg	$m_{\mathrm{cat,UV}}$ mg	$x_{\mathrm{cat,UV}}$ wt-%	$x_{\mathrm{cat,ICP}}$ wt-%	$x_{\mathrm{cat,ICP}}/x_{\mathrm{cat,UV}}$
W02-2[a]-10[b]	101.8	0.21	0.20	0.13	0.64
W02-2-24	109.0	0.26	0.24	0.11	0.46
W02-4-10	104.2	0.25	0.24	0.19	0.79
W02-4-24	104.7	0.26	0.25	0.17	0.68
W02-6-10	101.8	0.50	0.49	0.18	0.36
W02-6-24	107.6	0.28	0.26	0.16	0.61
K02-2-10	7385.6	1.24	0.02	0.01	0.59
K02-6-10	7752.5	3.66	0.05	0.02	0.42
K20-2-10	7596.7	1.50	0.02	0.01	0.51
K20-6-10	7568.9	3.77	0.05	0.03	0.60

[a]concentration of precursor solution 2, 4 or 6 $g_{Pd(acac)_2}/l$
[b]impregnation time: 10 min or 24 hour respectively

ties would cause a much stronger increase of the pressure drop than observed experimentally, with the result that the apparent pore sizes increase in order to compensate for this error. Thus, the combination of permeance measurements with a transition regime flow model generates interesting information about the pore structure but seems to be unsuitable for the exact determination of the geometric properties pore size and porosity. Nevertheless the measurements confirm an increase of catalyst loading proportional to the precursor concentration.

Combination of UV-vis measurements of the precursor solution and ICP-OES analyses of the catalytic membrane samples allows for a complete material balance of catalyst. Table 3.7 summarizes the resulting catalyst loading as calculated from the change in precursor concentration and those measured by ICP-OES.

The catalyst loading determined from the concentration change of the precursor solution is always higher than the one determined by elemental analysis of the catalytic membrane sample. The ratios vary between 36 and 79 %. This may have different reasons. A feasible explanation can be given by assuming that, despite high pressure microwave digestion, not all

of the catalyst is dissolved before the analysis. A different approach is based upon the assumptions that either not all of the catalyst is deposited on the membrane, but also on the impregnation vessel, or that a part of the catalyst is lost during the evaporation and calcination steps. The extraordinarily high value of the W02-6-10 sample suggests that systematic errors cannot be entirely prevented.

Although the total amount of catalyst deposited on the K02 and K20 membranes exceeds that found on the W02 membranes, the specific catalyst loading is smaller by one order of magnitude. This can be contributed to the smaller pore dimensions in the W02 membranes, correlated to a higher specific surface. In fact, for comparable deposition conditions, the catalyst loading is approximately proportional to the specific surface.

Comparing the catalyst loading of the W02 membranes as a function of the impregnation time, no correlation can be found. In some cases the catalyst loading determined for 10 min of impregnation time exceeds the one determined for 24 h of impregnation. It can be assumed that an impregnation time of 10 min is sufficient for complete intrusion of the precursor solution into the pores and that no further precursor adsorbs to the pore walls in the following period of time. Thus, no variation of impregnation time is performed for the Kerafol membranes.

Apparently the catalyst loading is a function of the precursor concentration and the specific surface of the sample, whereas the influence of impregnation time is negligible. Scattering of the measurement data impedes determining a proper function, but comparing with the permeance measurements a slightly less than linear relationship can be assumed. These observations are in agreement with the results of Boitiaux et al. (1983) and Goetz et al. (1995) presented in Table 3.5. The precursor solution concentrations of 2, 4 or 6 $g_{Pd(acac)_2}/l$ correspond to 0.7, 1.4 or 2.1 g_{Pd}/l. With a specific surface of 7.5 m^2/g (Table 3.3) slightly lower than those given in Table 3.5, the catalyst loadings determined by ICP are in good agreement with those measured by Boitiaux et al. (1983) and Goetz et al. (1995).

3.3 Reaction Experiments

Reaction experiments are performed to validate the different reactor models, measuring conversion and selectivity of model reactions, pressure drop and several temperatures. In Subsection 3.3.1 the thermodynamics and kinetics of the applied model reactions are reviewed. Two different flow configurations are discussed in Subsection 3.3.2 for the case that more than one catalytic membrane is used as reactor. The experimental facilities for all performed flow and reaction experiments are described in Subsection 3.3.3, including the method applied for determining the product concentration by FTIR spectroscopy. Finally initial experimental results are presented in Subsection 3.3.4, aiming at correlating catalyst loading and catalytic activity.

3.3.1 Model Reactions

Hydrogenations of unsaturated hydrocarbons are frequently applied as model systems for heterogeneous gas phase reactions (Section 2.3). Palladium efficiently catalyzes hydrogenation and dehydrogenation reactions. In the work at hand, ethylene hydrogenation experiments are conducted, if only catalytic activity and temperature effects are investigated. If selectivity is of interest, partial ethyne hydrogenation is performed. Both reactions are highly exothermic:

$$\mathrm{C_2H_2 + H_2 \longrightarrow C_2H_4} \qquad \Delta H_\mathrm{R} = -172\,\mathrm{kJ/mol}, \tag{3.7}$$

$$\mathrm{C_2H_4 + H_2 \longrightarrow C_2H_6} \qquad \Delta H_\mathrm{R} = -137\,\mathrm{kJ/mol}. \tag{3.8}$$

Ethene Hydrogenation Kinetics

Ethene hydrogenation is not of industrial relevance, because ethene is, in contrast to the product ethane, a valuable intermediate for organic synthesis. That is why reaction kinetics are hardly reported. For the hydrogenation of ethene to ethane in absence of ethyne, Bos et al. (1993) observe severe mass transfer limitations if the reaction is carried out in excess of hydrogen. Under less extreme conditions, that is for temperatures between 303 and 353 K,

pressures from 0.15 to 2 MPa and hydrogen concentrations of 2 to 15 %, the following power-law rate expression is obtained:

$$r_{C_2H_6} = 1.99 \cdot 10^6 \ \exp(-4883/T) \ p_{C_2H_4}^{-0.85} \ p_{H_2}^{1.45} \ \text{mol/(kg s)}.^1 \tag{3.9}$$

It is worth noting that the exponent of ethene is negative, predicting a decrease of ethane formation for increased ethene partial pressures. This result suggests that the influence of adsorption and desorption and the resulting coverage of the catalytically active surface play a decisive role and must be taken into account if a mechanistic model is desired.

Ethyne Partial Hydrogenation Kinetics

Typical industrial conditions for the selective ethyne hydrogenation include an ethene rich stream with only around 1 % of ethyne and a slight excess of hydrogen. Bos and Westerterp (1993) review the kinetics and mechanism of ethyne hydrogenation on palladium catalysts. Describing several reaction steps, they claim that the reaction selectivity cannot be exclusively calculated from thermodynamics. The low number of kinetic studies presenting practical rate expressions is attributed to the complex nature of the system, which consists of at least four different reactions: hydrogenation of ethyne to ethene, hydrogenation of ethene to ethane, direct hydrogenation of ethyne to ethane and oligomerization of ethyne. However, the direct hydrogenation route is of minor importance. Borodzinski (1999) postulates the existence of two types of catalytic sites, created by carbonaceous deposits on the palladium surface. "A" sites represent small spaces that adsorb ethyne and hydrogen but due to steric hindrance do not adsorb ethene and are thus responsible for selectivity, whereas "E" sites adsorb all reactants.

For pressures between 0.3 and 2.1 MPa and temperatures between 299 and 330 K, Bos et al. (1993) test eight different sets of Langmuir-Hinshelwood-like rate expressions. Many models are found to describe the data similarly well, with lower accuracy for selectivity compared to conversion. Without addition of CO the selectivity towards ethene typically reaches values between 0.3 and

[1] partial pressures in MPa

0.6, whereas in the presence of CO selectivity increases up to 0.9. Mostoufi et al. (2005) perform similar experiments deriving kinetic data for industrial conditions, yielding complex expressions with a large number of parameters.

As the work at hand does not aim at reaction kinetics under industrial conditions, the experiments are performed in absence of CO and without excess of ethene. For these conditions, simple power-law expressions are reported by Bos et al. (1993). The rate of ethyne hydrogenation at low concentrations of ethene is found to be at least one or two orders of magnitude lower than that of ethene hydrogenation in absence of ethyne, reducing the probability of mass transfer limitations. The best results are obtained with the following power-law rate expressions for a temperature of 303 K and pressures between 0.4 and 1.6 MPa:

$$r_{\mathrm{C_2H_4}} = 8.1 \cdot 10^{-6}\ p_{\mathrm{C_2H_2}}^{0.52}\ p_{\mathrm{H_2}}^{0.43}\ \mathrm{mol/(kg\ s)}, \tag{3.10}$$

$$r_{\mathrm{C_2H_6}} = 4.3 \cdot 10^{-6}\ p_{\mathrm{C_2H_2}}^{0.14}\ p_{\mathrm{H_2}}^{0.49}\ \mathrm{mol/(kg\ s)}. \tag{3.11}$$

It is important to note that these kinetic rates only describe the gross behavior of the reaction system. Both products are treated as if they are directly generated from ethyne and hydrogen, although the by far more relevant mechanism for ethane formation is the hydrogenation of ethene, which should be a function of ethene partial pressure rather than of ethyne.

As a result of the poor availability of kinetic data, the general power rate law with variable parameters shown in Equations 3.12 and 3.13 is applied in the work at hand, using the kinetics given by Bos et al. (1993) as a reference. Although this is a severe simplification of the heterogeneous reaction mechanism, this approach should generate suitable reaction rates for the range of operating conditions applied in the work at hand. An Arrhenius approach (Equation 3.14) accounts for temperature dependence of the rate constants.

$$r_{\mathrm{C_2H_2}} = -k_1\ p_{\mathrm{C_2H_2}}^{m_1}\ p_{\mathrm{H_2}}^{n_1} \tag{3.12}$$

$$r_{\mathrm{C_2H_6}} = k_2\ p_{\mathrm{C_2H_4}}^{m_2}\ p_{\mathrm{H_2}}^{n_2} \tag{3.13}$$

$$k_i = k_{i\infty} \cdot \exp\left(-\frac{E_i}{RT}\right) \tag{3.14}$$

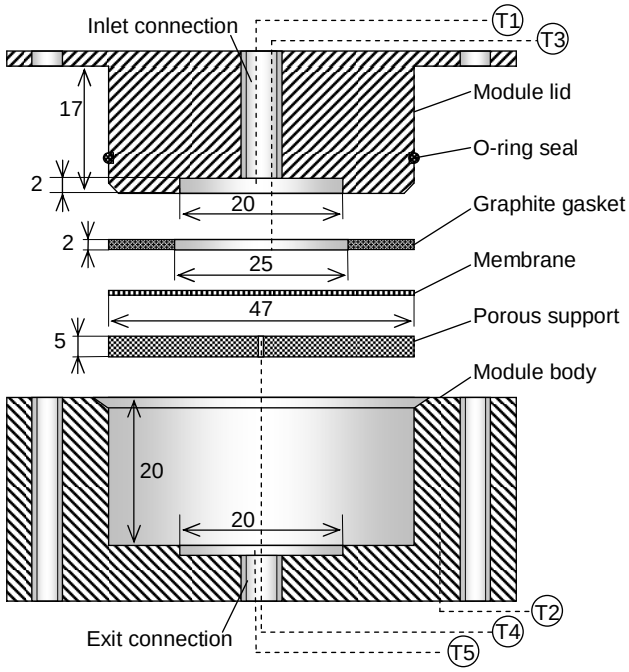

Figure 3.8: Reactor module employed for flow-through experiments

3.3.2 Reactor Module and Membrane Configurations

The reactor module has to fulfil several tasks:

- Provide inlet and outlet for gas flows on opposite sides of the membrane,
- Provide open membrane surface with even flow distribution,
- Support the membrane to prevent breakup,
- Seal the gap between membrane and module to prevent slippage,
- Transfer heat to the membrane during heating,
- Transfer heat from the membrane during reaction.

For a single catalytic membrane the best results are achieved by a module consisting of a bottom part (body), a porous support plate, a graphite gasket and a top part (lid), as displayed in Figure 3.8. The body provides an exit connection for the product gas flow and a circular cavity for a porous metal support plate, the membrane itself and the module lid. The catalytic membrane is put on top of the support plate, followed by a graphite gasket with a thickness of 2 mm (Seybold IP 47 x 25 mm). A hole in the center of the

support plate allows for insertion of a thermocouple. The lid of the module is equipped with an inlet connection for the feed gas flow and an outside sealing O-ring (FKM 80) to seal the gap between lid and bottom part. It is mounted to the body by means of four socket screws. The thermocouples are introduced via the inlet and exit fittings. No special measures have been taken to improve the heat transfer from the membrane.

Assembly

The support plate is introduced into the body of the module. The catalytic membrane is put on top of the support plate, followed by the graphite gasket, ensuring that the chamfered side faces the membrane. The lid is introduced into the body and manually pressed until touching the graphite gasket. The screws are tightened only slightly. Due to the different thermal expansion of the materials, the membrane has to be heated to the desired operation temperature before further tightening to prevent membrane breakage. When operation temperature is reached, a low inert gas flow is metered to the module, measuring pressure drop. Finally the screws are tightened gradually until no further pressure drop increase is observed.

Multiple Flow-Through

Although the extremely short reactor length represents one of the main characteristics of the concept, in some cases a longer reaction path is desirable, resulting in increased contact time and narrower residence time distribution. Ways of increasing the reactor length without increasing individual membrane thickness are given either by flowing through several membranes in sequence (Figure 3.9(a)) or by flowing through different parts of the same membrane in sequence according to Figure 3.9(b). Flow through multiple membranes in sequence can easily be achieved by piling more than one catalytic membrane directly on top of each other in the reactor module described above. No further sealing is necessary, which can be seen in an increase of the pressure drop proportional to the number of membranes. The concept of flowing multiply through a single membrane has been abandoned after first

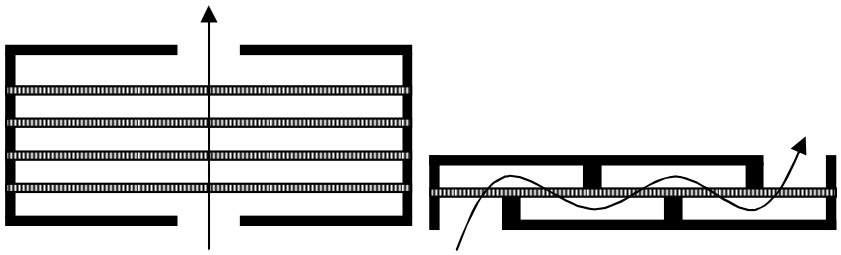

(a) Flow through multiple membranes

(b) Multiple flow through single membrane

Figure 3.9: Configurations for multiple flow-through

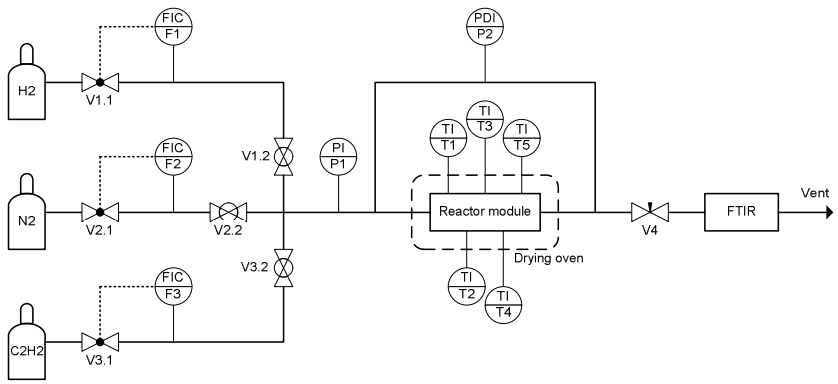

Figure 3.10: Flow sheet of experimental test facility

trials due to serious problems with sealing and membrane stability. Increased pressure drop represents the major drawback of multiple flow-through.

3.3.3 Test Rig and Analytics

An experimental setup consisting of a heated reactor module with supply of up to three controlled gas flows, temperature and pressure measurement as well as in-line product analytics is applied for the flow and reaction experiments (Figure 3.10).

The gaseous reactants (Acetylene 2.6, Ethylene 5.0, Hydrogen 5.0) as well as inert gas (Nitrogen 5.0) are supplied in compressed gas cylinders and metered by means of three mass flow controllers F1, F2 and F3 (Buerkert Mass Flow Controller Byp. CMOSENS Light 8711, $3\,\mathrm{l_N/min}$). The reactor module is situated in a temperature controlled drying oven (Siemens Sichro-

mat 1, 300 °C) and equipped with five thermocouples (NiCr-Ni (Type K), $D = 0.5\,\mathrm{mm}$) for measuring the temperatures of feed gas (T1), reactor module (T2), inlet membrane surface (T3), outlet membrane surface (T4) and permeate gas (T5). The manual needle valve V4 downstream of the reactor can be used to control the absolute pressure in the reactor, which is measured upstream of the reactor by means of a WIKA pressure transmitter IS-10 (P1, 0 – 1 bar abs.). The transmembrane pressure difference is measured by a WIKA Differential pressure transmitter Tronic 891 (P2, 0 – 1 bar).

Measurement of reactant concentration

The reactant concentrations are measured in-line by means of Fourier transform infrared spectroscopy (FTIR), applying a Bruker Vector 33 instrument. The hydrocarbons ethyne, ethene and ethane can be detected independently according to their representative absorption signals. The highest peaks are found for ethyne at $730\,\mathrm{cm}^{-1}$, for ethene at $950\,\mathrm{cm}^{-1}$ and for ethane at $2950\,\mathrm{cm}^{-1}$ (Figure 3.11). The absorption signals are evaluated to calculate the relative concentrations of the detectable reactants. Hydrogen and nitrogen cannot be detected by FTIR. Their concentrations are calculated by a stoichiometric balance.

The measured spectrum of the gas mixture is reproduced by a linear combination of the pure component signals, weighted according to their relative absorption $a_{\mathrm{rel},i}$, which resembles the ratio of the measured signal and the pure component signal. Two further variables are added to account for zero offset and linear drift. The five parameters are obtained using a least squares method.

While the absolute absorption signal obtained by FTIR is subject to change due to wear of optical components, the ratio of signals of two different components stays constant. Thus, the sum of the relative absorptions $a_{\mathrm{rel},i}$ of the detected gases obtained by the described method might reach values larger than one, if the measurement of the pure component signals has not been performed on the same day. Definition of reduced mole fractions x_i^*, which are related to the total amount of hydrocarbons rather than to the

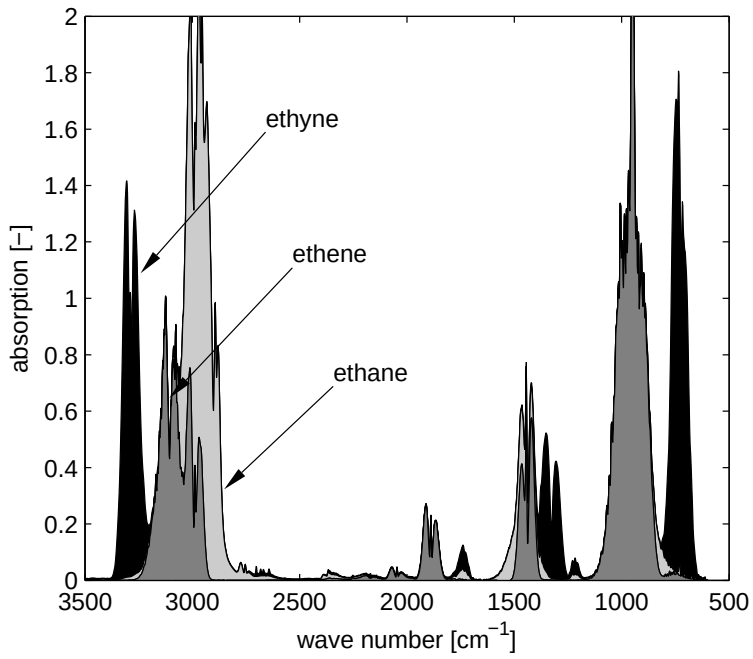

Figure 3.11: FTIR spectra of ethyne, ethene and ethane

complete reactant mixture, allows for direct calculation of conversion X and selectivity S. In contrast to the mole fractions x_i, the reduced mole fractions x_i^* are not affected by a molar flow rate reduction due to reaction, as the total amount of HC molecules is invariant.

$$x_i^* = \frac{a_{\mathrm{rel},i}}{\sum a_{\mathrm{rel},i}} = \frac{\dot{n}_i}{\dot{n}_{\mathrm{HC}}} \tag{3.15}$$

$$\sum x_i^* = 1 \tag{3.16}$$

For ethene hydrogenation in absence of ethyne, only two HC are detected and the total amount of hydrocarbons corresponds to the initial amount of ethene. Thus, the conversion can be calculated according to:

$$X_{\mathrm{C_2H_4}} = \frac{\dot{n}_{\mathrm{C_2H_4},0} - \dot{n}_{\mathrm{C_2H_4},1}}{\dot{n}_{\mathrm{C_2H_4},0}} = 1 - x^*_{\mathrm{C_2H_4}}. \tag{3.17}$$

For ethyne hydrogenation in initial absence of ethene and ethane, all three HC are detected. Ethyne conversion and selectivity towards ethene are calculated

as

$$X_{C_2H_2} = \frac{\dot{n}_{C_2H_2,0} - \dot{n}_{C_2H_2,1}}{\dot{n}_{C_2H_2,0}} = 1 - x^*_{C_2H_2}, \tag{3.18}$$

$$S_{C_2H_4} = \frac{\Delta\dot{n}_{C_2H_4}}{\Delta\dot{n}_{C_2H_2}} = \frac{x^*_{C_2H_4}}{1 - x^*_{C_2H_2}}. \tag{3.19}$$

3.3.4 Catalyst Loading and Catalytic Activity

The catalytic activity of the different membranes is characterized by performing reaction experiments, applying ethene hydrogenation as model reaction. The measured conversion for given process parameters is correlated to the calculated porosity and amount of catalyst as determined in Section 3.2.2. Both Whatman and Kerafol membranes are applied.

Figure 3.12(a) shows the achieved conversions of ethene hydrogenation experiments with stoichiometric feed of reactants as a function of the total standard volumetric flow rate. W02 membranes with different catalyst loading are employed at feed temperatures of 100 °C with ambient pressure on the permeate side. As determined in Subsection 3.2.2, the catalyst loading increases with increasing concentration of the precursor solution. The observed space-time-yields reach values of 100 kmol/(m^3 s) or 3 kg/(L s) respectively.

Contrary to the expectations, the achieved ethene conversion decreases with increasing catalyst loading. Apparently the catalytically active surface does not grow proportionally to the amount of catalyst, for example due to formation of larger particles. If additionally the reaction rate is limited by a low number of available catalytically active sites due to the surface coverage, the decreasing conversion as a function of the flow rate can be explained. Consequently, the reduced apparent porosity of the catalytic membranes with higher catalyst loading, as determined in Subsection 3.2.3, reduces the hydrodynamic residence time in the catalytic pores, which in combination with the missing increase of catalytically active sites results in decreased conversions. As a further explanation, increasing the total amount of catalyst in the membrane may lead to complete blocking of single pores, resulting in an increased pressure drop and keeping the catalyst in the blocked pores unavailable for the reactants.

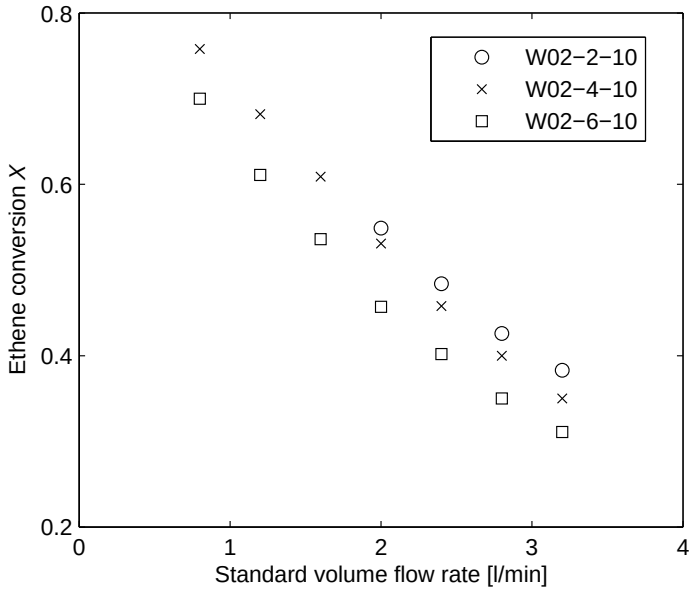

(a) Catalytic anodized membranes (Whatman)

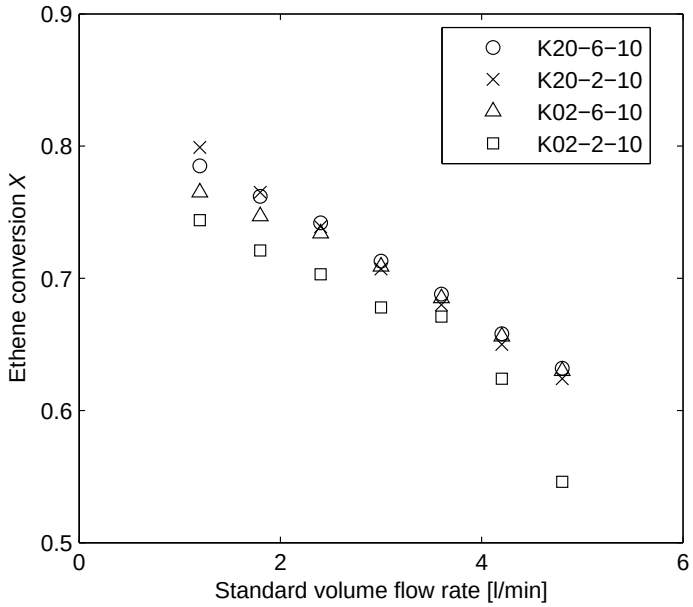

(b) Catalytic sintered membranes (Kerafol)

Figure 3.12: Ethene hydrogenation experiments with catalytic membranes: Conversion as function of total standard volumetric flow rates; stoichiometric feed of ethene and hydrogen, feed temperature 100 °C, ambient permeate pressure

Results of ethene hydrogenation experiments performed with sintered Kerafol membranes are shown in Figure 3.12(b). In the displayed experiments, the reactants are fed stoichiometrically with 33 % nitrogen dilution at feed temperatures of 100 °C with ambient pressure on the permeate side. Although three of the four investigated membranes produce similar conversions, especially at higher flow rates, the K20 membranes show higher catalytic activity than the K02 membranes, although their catalyst loading is comparable. In contrast to the experiments with the anodized membranes, the conversions do not decrease with increasing amount of deposited catalyst.

In summary of all measurements, the obtained conversion is not directly correlated to the catalyst loading determined by ICP and UV-vis, but rather to the mean hydrodynamic residence time, indicating transport resistances due to a limited number of free catalytic sites. The influence of the membrane type and microstructure appears to be equally significant and will be discussed in Section 5.4.

3.4 Conclusions

The microstructure of different ceramic alumina membranes is characterized according to pore geometry, size distribution, porosity and tortuosity by means of several analytic methods. Anodic alumina membranes are made up of uniform cylindrical channels with a mean pore size around 0.2 µm and a narrow pore size distribution, whereas sintered alumina membranes show a non-uniform structure with remarkable tortuosity.

Palladium is deposited as hydrogenation catalyst in the pores of the both anodized and sintered ceramic membranes by a dry impregnation method employing $Pd(acac)_2$ solved in toluene. The catalytic preparation slightly modifies the microstructure by reducing the porosity, although catalytic particles are not detectable by SEM. The amount of catalyst deposited in the membranes is assessed by different methods. The resulting catalyst loading is a function of the catalyst concentration in the precursor solution and of the specific surface of the membrane, whereas increasing the impregnation time beyond 10 minutes shows no measurable effect on the catalyst loading. At in-

termediate catalyst concentrations in the precursor solution of $4\,g_{Pd(acac)_2}/l$, corresponding to $1.4\,g_{Pd}/l$, a catalyst loading of around 0.2 wt% Pd is obtained for the anodized membranes. Due to low catalyst concentrations below the detection limit of the applied methods, a spatial catalyst distribution inside the membrane cannot be determined.

Ethene hydrogenation and partial ethyne hydrogenation are selected as model reactions. The experimental test rig allows for performing flow and reaction experiments with up to three independently metered reactants and in-line product analytics using FTIR-spectrometry. Arranging several membranes in sequence can create a longer reaction path resulting in increased contact time and a narrower residence time distribution. Ethene hydrogenation experiments are performed with space-time-yields in the range of $100\,kmol/(m^3\,s)$ applying the anodized Whatman membranes. Whereas the catalytic activity of the membranes is expected to increase with the catalyst loading, the observed decrease indicates a reduction of available catalytic surface sites. Especially in the anodized Whatman membranes, an excessive amount of catalyst in the pores might cause an inhomogeneous catalyst distribution or even complete blockage of single pores, reducing the total catalytic activity of the membrane.

Chapter 4

Reactor Fluid Dynamics

Fluid dynamic models allow for detailed characterization of chemical reactors independently from a respective chemical reaction. The pressure drop caused by a reactor can be calculated beforehand by means of correlations. Suitable models can predict the residence time distribution, which is one of the main characteristics to describe reactor performance. This is elucidated in Section 4.1 for the investigated catalytic membrane reactor, deducing guidelines for suitable operating parameters. The models are based on the straight microchannel structure of the anodized Whatman membranes. They might be applied for sintered membranes as well, but would require implementation of suitable correction factors such as tortuosity.

Commonly used correlations are based on the continuum hypothesis, which neglects molecule-wall interactions compared to molecule-molecule interactions. For the small dimensions of the membrane pore channels, this hypothesis is not always valid. Section 4.2 discusses the influence of so-called rarefaction effects on the reactor behavior, especially on the pressure drop.

4.1 Residence Time Distribution

Basic reactor modelling assumes idealized flow patterns in continuous reactors with the extreme cases of a plug flow tubular reactor (PFTR) on the one

hand and a continuous stirred tank reactor (CSTR) on the other hand. For non-ideal flow, elements of fluid can take different routes through a reactor, spending different periods of time inside the reactor. The residence time distribution (RTD) $E(t)$ describes the distribution of these times for the stream of fluid leaving the vessel. It has the unit of [1/s] and is normalized in such a way, that the area under the curve becomes unity (Levenspiel, 1999)

$$\int_0^\infty E(t)dt = 1. \tag{4.1}$$

For measuring the RTD, a tracer signal has to be set at the reactor inlet at $t = 0$ and the concentration of the tracer at the outlet has to be measured as a function of time. $E(t)$ is obtained experimentally as a pulse response, which means that all tracer is added in a single pulse. The step response $F(t)$ can be obtained by permanently increasing the tracer concentration at the inlet in a step function. Both functions are correlated as follows:

$$F(t) = \int_0^t E(t)dt, \tag{4.2}$$

$$E(t) = \frac{dF(t)}{dt}. \tag{4.3}$$

Step and pulse responses of an ideal CSTR and an ideal PFTR will be, amongst others, displayed in Figure 4.2.

A narrow residence time distribution is crucial for reaction systems with undesired sequential reactions. PFTR behavior represents the optimum flow pattern in this case. In a PFTR all fluid elements flow through the reactor at equal velocity without any axial mixing, yielding a sharp RTD in the shape of a Dirac delta function, equal to the tracer signal at the inlet.

For the investigated reactor concept the RTD can hardly be measured directly. From a reaction point of view, only the time the reactants are in contact with catalyst is of interest, being the time the fluid spends in the membrane pores. Due to the large number of membrane pores, the time required for spreading the signal to all pore channels will be at least in the same order as the time the tracer spends inside the membrane, which is in the range of milliseconds. Thus, direct measurement of the RTD is not

promising.

Nevertheless, based on a few assumptions a realistic model of the reactor hydrodynamics can be created, allowing for calculation of the resulting RTD for various operation conditions. Experimental proof for a narrow RTD can be found indirectly by performing a sequential reaction, comparing the selectivity with the ideal selectivity expected in a PFTR. This will be examined in Chapter 6.

The so-called dispersion model has been created to describe the hydrodynamic behavior of non-ideal reactors similar to PFTRs. All deviations from ideal behavior, such as velocity profiles or axial diffusion processes, are accounted for with a single parameter, called axial dispersion coefficient D_{ax}, in a diffusion-like process superimposed on plug flow.

The flow-through catalytic membrane microchannel reactor can be considered a tube bundle reactor on microscale. It consists of a large number of parallel independent pore channels. In the ideal case all pore channels exhibit equal diameter and axial dispersion is negligible, resulting in PFTR behavior. The following deviations from this ideal behavior will be elucidated:

- The influence of pore size distribution is investigated by applying a model of parallel PFTRs with different diameters.
- Based on the parallel PFTR model, the influence of flowing through several membranes in series will be quantified.
- Axial dispersion in a single pore channel is quantified applying the dispersion model.
- Finally, pore size distribution and axial dispersion influence are combined to find ideal operating conditions.

4.1.1 Pore Size Distribution and Plug Flow

The commercially available anodized alumina membranes do not show exactly uniform pores but an observable pore size distribution (Section 3.1). To quantify the influence of this distribution on the expected RTD, a simple membrane model is set up, consisting of a number of parallel PFTRs with different diameters. For ease of computation, the distribution of pore

Table 4.1: Representative pore size distribution determined for W02 membrane (Whatman Anodisc 0.2 µm), subdivided into nine pore size classes

Nominal pore size d_i [nm]	Pore size range [nm]	Rel. frequency N_i/N_{tot}
150	$140 < d \leq 160$	0.014
170	$160 < d \leq 180$	0.043
190	$180 < d \leq 200$	0.075
210	$200 < d \leq 220$	0.146
230	$220 < d \leq 240$	0.241
250	$240 < d \leq 260$	0.268
270	$260 < d \leq 280$	0.172
290	$280 < d \leq 300$	0.036
310	$300 < d \leq 320$	0.006

diameters is discretized into j pore size classes of equal width and a nominal pore size in the arithmetic mean of the pore size class. Table 4.1 shows an exemplary distribution for $j = 9$.

Each single pore is considered to be an ideal PFTR with constant diameter and axial velocity. Axial dispersion effects are neglected in this section, but will be quantified in Subsection 4.1.2. Although pressure drop along the channel due to friction is neglected regarding axial velocity, it has to be considered to calculate the split of the total flow into the single pore size classes. The influence of Knudsen-diffusion is neglected.

Introducing the mean pore diameter d_{m}, the mean cross-sectional area of the pores A_{m} is

$$A_{\text{m}} = \frac{\pi}{4} \cdot d_{\text{m}}^2. \tag{4.4}$$

The flow-through area of the membrane A_{mem} is

$$A_{\text{mem}} = \epsilon \cdot \frac{\pi}{4} \cdot D_{\text{mem}}^2, \tag{4.5}$$

with the open membrane diameter D_{mem} and the porosity ϵ.

The total number of pores available for convective flow N_{tot} amounts to

$$N_{\text{tot}} = \frac{A_{\text{mem}}}{A_{\text{m}} \cdot \sum_i \left(\frac{A_i}{A_{\text{m}}} \cdot \frac{N_i}{N_{\text{tot}}} \right)} = \frac{A_{\text{mem}}}{A_{\text{m}} \cdot \sum_i \frac{N_i}{N_{\text{tot}}} \left(\frac{d_i}{d_{\text{m}}} \right)^2} \tag{4.6}$$

with the subscript i representing the single pore size classes and $\frac{N_i}{N_{\mathrm{tot}}}$ the relative frequency of the respective pore size class as determined in Table 4.1. The sum in the denominator can be interpreted as a correction factor for non-ideal membrane geometry, turning to one for uniform pores.

The total flow is split into the pore size classes in such a way that the resulting pressure drop in all parallel pores will be equal. Thus, the relative axial flow velocity in each pore size class, related to the axial velocity in a pore of the mean pore size, can be calculated from the correlation for the pressure drop in laminar circular channels

$$\Delta p = \frac{32\,\eta\,u_i\,L}{d_i^2}, \tag{4.7}$$

yielding

$$\frac{u_i}{u_{\mathrm{m}}} = \left(\frac{d_i}{d_{\mathrm{m}}}\right)^2. \tag{4.8}$$

The resulting residence time for each pore size class amounts to

$$\tau_i = \frac{L}{u_i}. \tag{4.9}$$

For calculation of the RTD not only the residence times of each pore size class are required, but also the share of the total flow, that passes through the respective pore size class. This is calculated by the number of pores in the pore size class N_i and the molar flow rate through each pore size class $\dot{n}_i$, which itself depends on the axial flow velocity u_i and the cross-sectional area A_i. The relative molar flow rate through each pore size class can be calculated by means of the continuity equation, assuming constant density for the sake of simplicity

$$\frac{\dot{n}_i}{\dot{n}_{\mathrm{m}}} = \frac{u_i}{u_{\mathrm{m}}} \cdot \left(\frac{d_i}{d_{\mathrm{m}}}\right)^2 = \left(\frac{d_i}{d_{\mathrm{m}}}\right)^4. \tag{4.10}$$

As all pore size classes are correlated to a mean pore size d_{m}, the absolute values for axial velocity u_{m} and molar flow rate $\dot{n}_{\mathrm{m}}$ of this mean pore size

remain to be calculated according to

$$\dot{n}_{\mathrm{m}} = \frac{\dot{n}_{\mathrm{tot}}}{N_{\mathrm{tot}} \cdot \sum_i \frac{N_i}{N_{\mathrm{tot}}} \left(\frac{d_i}{d_{\mathrm{m}}}\right)^4}, \tag{4.11}$$

$$u_{\mathrm{m}} = \frac{\dot{n}_{\mathrm{m}} \cdot R \cdot T}{p \cdot A_{\mathrm{m}}}, \tag{4.12}$$

assuming ideal gas behavior with pressure p, temperature T and the gas constant R. Again the sum in the denominator can be interpreted as a correction factor for non-ideal membrane geometry, turning to one for uniform pores.

With this information, the resulting residence time distribution can be calculated for given molar flow rate $\dot{n}_{\mathrm{tot}}$, pressure p, temperature T and pore size distribution. The result will be a step-shaped function with a number of steps according to the number of pore size classes j (Figure 4.1).

To obtain a resulting RTD for flow through several membranes in series, perfect mixing is assumed in the space between the single membranes. The RTD after each membrane is determined by adding the residence times in the current membrane to the accumulated residence times of the previous membranes, taking into account all possible combinations of pore classes and weighting their probability according to their relative flow rates. Thus the step-shaped function after the nth membrane consists of j^n steps.

As becomes obvious when considering the case of a cascade of CSTR, flowing through several reactors in sequence reduces the width of the RTD. If different configurations are supposed to be comparable, the total mean residence time has to be kept constant. Thus, for comparing the resulting RTD for flow through n membranes in series with the RTD for a single membrane, the total molar flow rate has to be multiplied by n to obtain the same total mean residence time. The result of this calculation is illustrated in Figure 4.1, comparing the cases of 1, 2, 4 and 8 membranes in series. Increasing the number of membranes to values higher than 4 quickly leads to prohibitive pressure drops, if the flow through velocity is increased simultaneously. As the pressure drop is proportional to the axial velocity (Equation 4.7) and also proportional to the number of membranes, a reactor of n serial membranes with the same mean residence time as a single membrane reactor will have

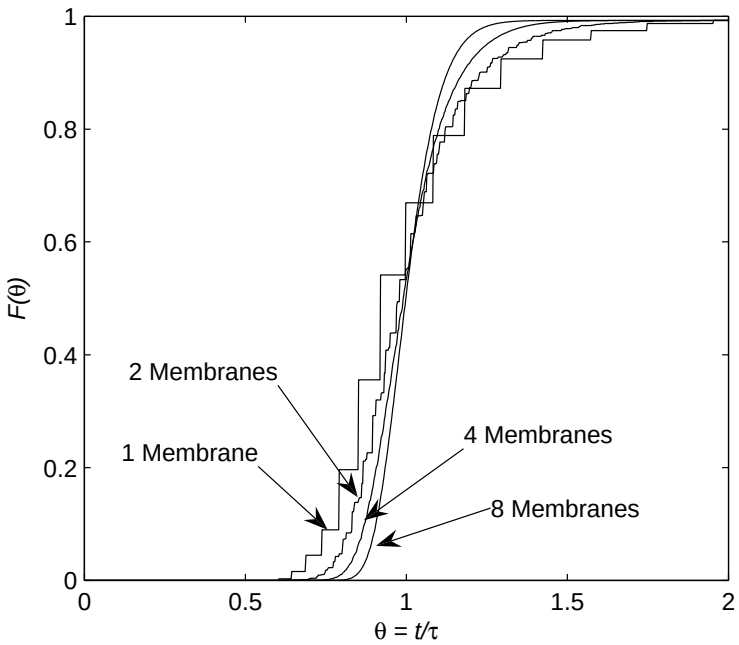

Figure 4.1: Step response RTD for plug flow through 1, 2, 4 and 8 membranes in series as function of normalized residence time

an increased pressure drop by a factor of n^2.

The resulting RTD obviously shows deviations from ideal PFTR behavior. The dependence on the fourth power of the pore diameter significantly amplifies even smaller deviations from the mean pore size. Nevertheless, even a single membrane is far from CSTR behavior, and for a membrane reactor consisting of 3 or more membranes in series, the RTD can be considered rather narrow.

4.1.2 Isoporous Membrane with Dispersion

The material balance for the dispersion model is given as:

$$\frac{\partial c}{\partial t} = -u\frac{\partial c}{\partial z} + D_{\text{ax}}\frac{\partial^2 c}{\partial z^2}. \tag{4.13}$$

Introducing the dimensionless Bodenstein number *Bo*, describing the flow behavior of the whole reactor

$$Bo = \frac{uL}{D_{\mathrm{ax}}}, \tag{4.14}$$

and the mean residence time $\tau = L/u$ yields:

$$\frac{\partial c}{\partial (t/\tau)} = \frac{1}{Bo}\frac{\partial^2 c}{\partial (z/L)^2} - \frac{\partial c}{\partial (z/L)}. \tag{4.15}$$

When axial dispersion is taken into account, the RTD of a single pore deviates from PFTR behavior. For small deviations from plug flow, i.e. $Bo > 100$, a symmetric $E(t)$ can be assumed, the reactor behavior is very similar to a PFTR. Appreciable dispersion results in an asymmetric $E(t)$. In this case different boundary conditions can be assumed. The closed vessel boundary condition implies that the fluid only enters or leaves the pore once, whereas the open vessel boundary condition allows the fluid to cross the boundaries more often. As Levenspiel (1999) points out, only the closed-closed boundary condition (closed at inlet and at outlet) yields a proper RTD, but cannot be solved analytically. A numerical solution can be determined using the boundary conditions introduced by Danckwerts (1953), allowing a concentration step at the reactor entrance

$$z = 0: \quad c = c_{0-} + \frac{1}{Bo}\frac{d^2 c}{d(z/L)^2} \tag{4.16}$$

$$z = L: \quad \frac{dc}{d(z/L)} = 0 \tag{4.17}$$

with c_{0-} as upstream concentration just outside the reactor.

For open-open boundary conditions an analytical solution exists (Baerns et al., 1999; Pallaske, 1984). The normalized pulse response amounts to

$$E(\theta) = \frac{1}{2\,\theta}\sqrt{\frac{Bo}{\pi \cdot \theta}} \cdot \exp\left(\frac{-(1-\theta)^2 \cdot Bo}{4\,\theta}\right) \tag{4.18}$$

and exclusively contains *Bo* as variable parameter. The respective step re-

sponses can be calculated by integration.

Resulting $E(\theta)$ and corresponding $F(\theta)$ for different values of Bo for closed and open boundary conditions are illustrated in Figure 4.2. A large value of D_{ax} corresponds to a wide RTD with the extreme case of CSTR behavior for $D_{\mathrm{ax}} \to \infty$ or $Bo = 0$ respectively. Accordingly a small value describes a narrow RTD with PFTR behavior for $D_{\mathrm{ax}} = 0$ or $Bo \to \infty$ respectively. For high values of Bo the differences between open-open and closed-closed boundary condition are negligible, whereas for high dispersion, i.e. low Bo, significant deviations can be observed.

In the case of the catalytic membrane microchannel reactor, the pore length $L = 60\,\mu\mathrm{m}$ is assumed to be constant for all membranes. The other parameters influencing Bo, axial velocity u and axial dispersion coefficient D_{ax} depend on the operating conditions. The axial velocity is directly influenced by the volumetric flow rate, which itself depends on molar flow rate, absolute pressure and temperature

$$u = \frac{\dot{n} \cdot R \cdot T}{p \cdot \epsilon \cdot A_{\mathrm{mem}}}. \tag{4.19}$$

For small channel diameters the feed to permeate pressure ratio can reach values up to 10 or higher. Compressibility effects are extremely pronounced in this case (Sabry, 2000), producing a significant velocity profile. For reasons of simplification, we assume a rather small ratio of feed and permeate pressure, leading to an almost constant axial velocity.

Although the flow in the microchannels is laminar, the intensive radial mixing produces a uniform radial concentration profile (Rouge et al., 2001). Consequently, axial dispersion in a microstructured pore is not based on deviations of the flow profile from plug flow but exclusively on molecular diffusion (rarefaction will be accounted for in Section 4.2.3). The molecular dispersion coefficient for a single fluid represents a fluid property and strongly depends on absolute pressure and temperature

$$D_{\mathrm{ax}} = D_{\mathrm{mol}} = \frac{1}{3}\bar{u}\lambda \propto \frac{T^{1.5}}{p}, \tag{4.20}$$

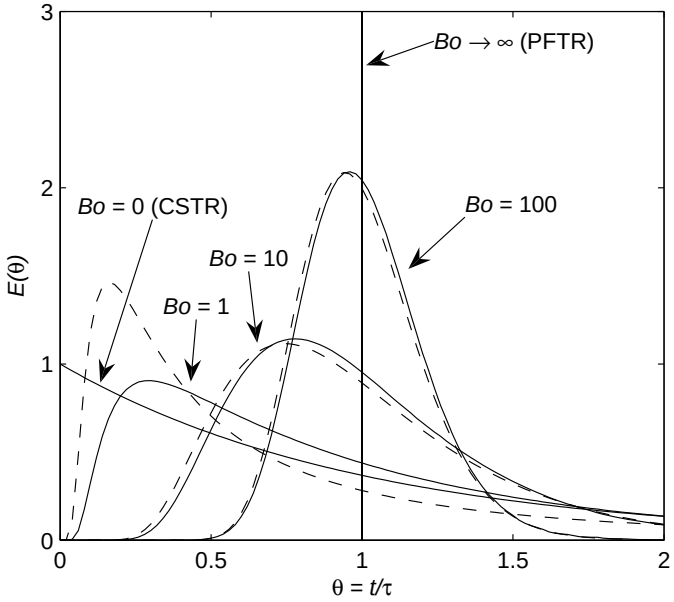

(a) Normalized pulse response $E(\theta)$

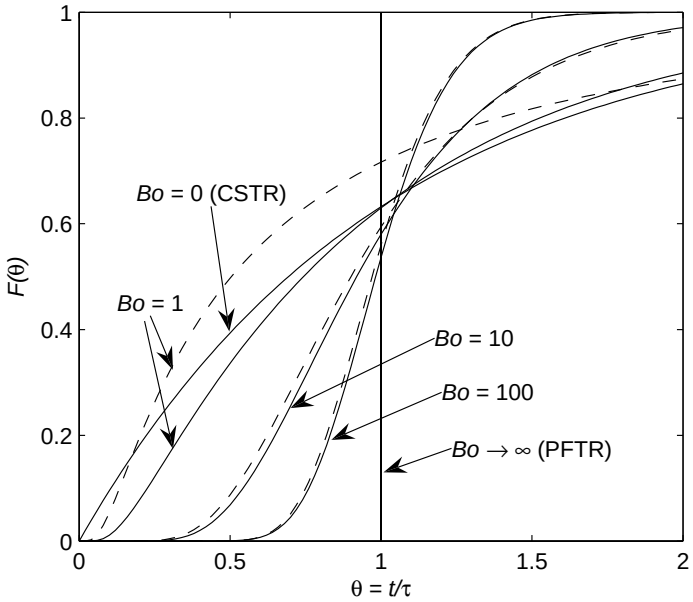

(b) Normalized step response $F(\theta)$

Figure 4.2: Residence time distributions for dispersion model with closed-closed boundary condition (solid lines) and open-open boundary condition (dashed lines) under variation of $Bo = uL/D_{\mathrm{ax}}$

with the mean molecular velocity $\bar{u}$ and the mean free path λ. For example the molecular diffusion coefficient and thus the axial dispersion coefficient of nitrogen under standard conditions is in the range of $D_{\mathrm{ax}} = 10^{-5}\,\mathrm{m^2/s}$. For an axial velocity of $u = 1\,\mathrm{m/s}$ and ambient pressure, the Bodenstein number results to $Bo = 6$. At 10 bar, D_{ax} decreases to $10^{-6}\,\mathrm{m^2/s}$. At the same time the axial velocity will be reduced by a factor of 10, if the molar flow rate is kept constant. Accordingly Bo is proportional to the molar flow rate and strongly increases for constant axial velocity at elevated pressures, which signifies that the negative effect of axial dispersion on the RTD is of major importance mainly for low absolute pressures.

4.1.3 Combined Pore Size Distribution and Axial Dispersion

In reality, the two considered effects do not occur separately. The resulting RTD is influenced by both PSD and axial dispersion. As a combined model, the multi-tube model composed of PFTR with different diameters as introduced in Subsection 4.1.1 can be extended by allowing axial dispersion according to Subsection 4.1.2 in each pore size class. The analytical solution for the dispersion model with open-open boundary conditions (Equation 4.18) is applied to each pore size class. Bo will vary in the different pore size classes proportional to the axial velocity u_i, while the other parameters L and D_{ax} remain constant for all pores. As the resulting pulse response $E(t)$ for each pore size class is now a continuous curve rather than a Dirac delta function, an integration yielding the corresponding step responses is not required.

For each pore size class i a pulse response with a mean residence time τ_i and a resulting Bo_i is obtained. These responses are weighted according to the share of the total flow, which passes the respective pore size class. The resulting RTD for the whole membrane is obtained by summation of the respective signals of the pore size classes as shown in Figure 4.3 for the two cases $Bo_{\mathrm{m}} = 1$ and $Bo_{\mathrm{m}} = 50$. Bo_{m} signifies the Bodenstein number valid for the mean pore size d_{m}. The increased axial velocity in the large

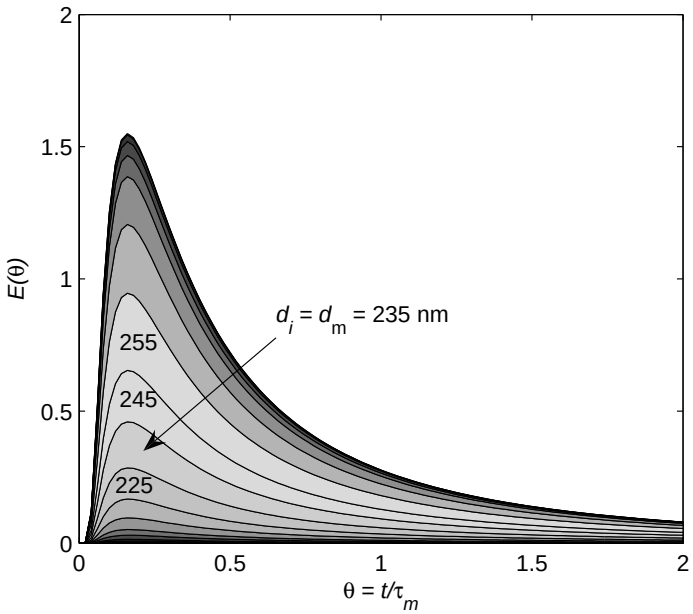

(a) $Bo_{\mathrm{m}} = 1$ (Strong axial dispersion)

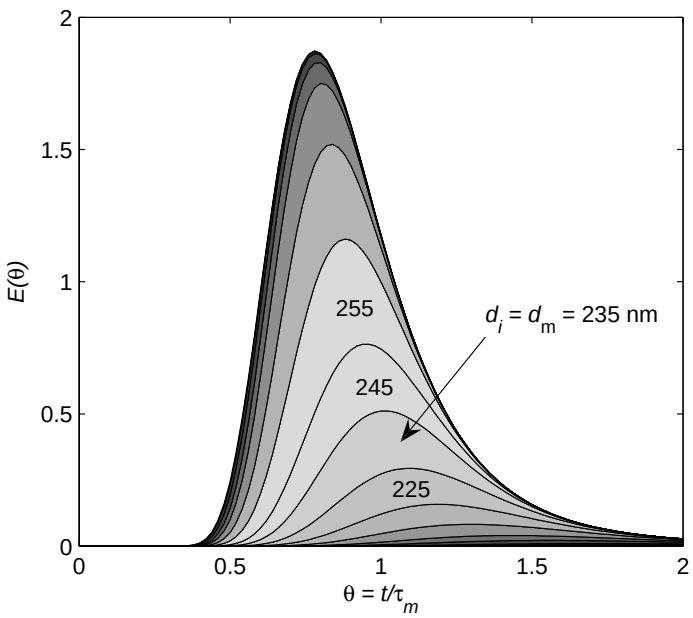

(b) $Bo_{\mathrm{m}} = 50$ (Weak axial dispersion)

Figure 4.3: Accumulated pulse responses for combined dispersion model and 17 pore size classes

pores results in a reduced mean residence time as well as a high value of Bo_i, yielding sharp peaks for small residence times and wide peaks for large residence times. Further, a larger share of the total flow passes the large pores, leading to a negligible influence of the small pore size classes. As can be seen in Figure 4.3, the pore size classes larger than the mean pore diameter $d_\mathrm{m} = 235\,\mathrm{nm}$ contribute much stronger to the RTD than the mean pore diameter, whereas the influence of the four smallest pore size classes is hardly visible.

For small values of Bo_m (Figure 4.3(a)), two features should be noticed: On the one hand, the resulting residence time distribution is very wide, resembling more a CSTR than a PFTR. On the other hand, the influence of the pore size distribution is negligible. The pulse responses of the single pore size classes show comparable mean values. The accumulated signal is similar to the pulse response of an isoporous membrane with mean pore size.

For increased Bo_m (Figure 4.3(b)) in contrast, the resulting RTD is rather narrow. However, the contributions of the discrete pore size classes are shifted laterally, leading to a much wider $E(t)$ than for an isoporous membrane. The smaller pore size classes generate a considerable tailing due to their low axial velocities. Further increase of Bo_m would consequently lead to a number of single peaks corresponding to the pore size classes, finally becoming the plug flow pore size distribution model developed in Subsection 4.1.1 for $Bo_\mathrm{m} \to \infty$.

For simplified handling and improved comparability, the influences of axial dispersion and pore size distribution can be combined in a single parameter, called effective Bodenstein number Bo_eff. It can be obtained by fitting the parameter Bo in Equation 4.18 to best reproduce the accumulated RTD with combined axial dispersion and pore size distribution as displayed in Figure 4.3.

Figure 4.4 shows a comparison of the RTD obtained by applying the combined axial dispersion and PSD model with the respective RTD for the dispersion model in the reference pore and the effective dispersion model with the resulting Bo_eff. For strong dispersion (Figure 4.4(a)), all three models produce similar results, $Bo_\mathrm{eff} \approx Bo_\mathrm{m}$. For weak dispersion (Figure 4.4(b)), the dispersion model for the reference pore strongly deviates from the combined

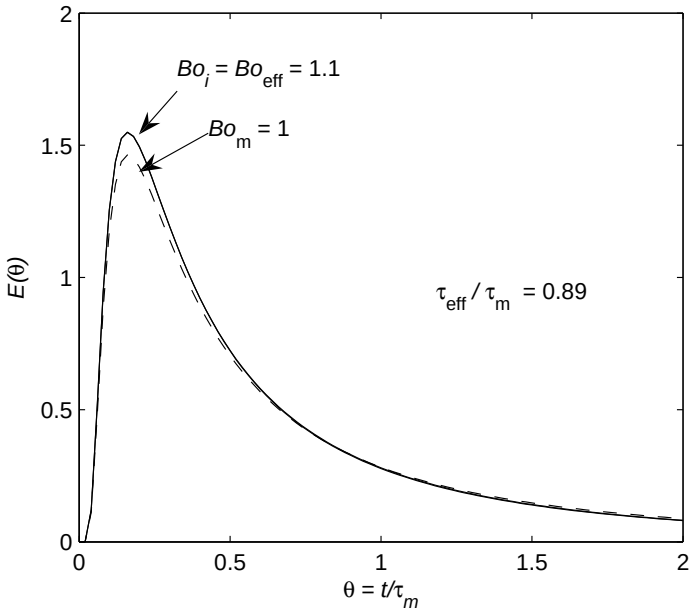

(a) $Bo_{\mathrm{m}} = 1$ (Strong axial dispersion), note that the combined model coincides with the effective dispersion model

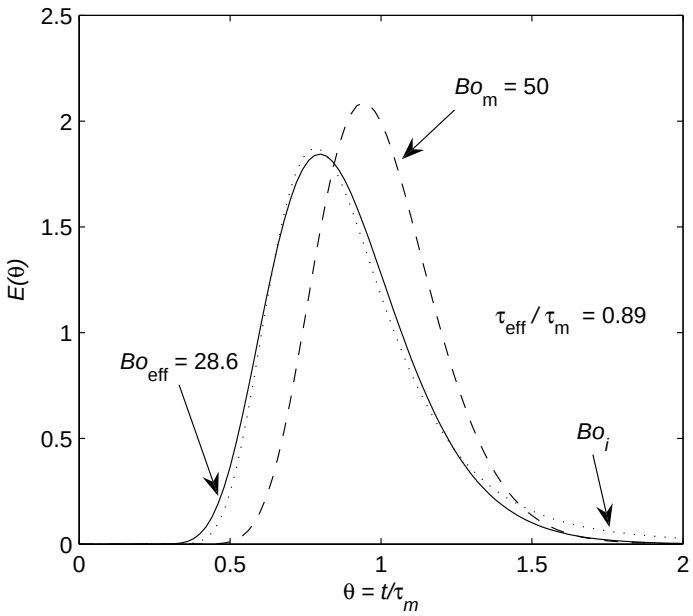

(b) $Bo_{\mathrm{m}} = 50$ (Weak axial dispersion)

Figure 4.4: Comparison between pulse response for (1) combined pore size distribution and dispersion "Bo_i", (2) dispersion model for mean pore size "Bo_{m}" and (3) effective dispersion model "Bo_{eff}"

model and the corresponding Bo_{eff} is significantly smaller than Bo_{m}.

In both cases, a deviation between the resulting mean residence time of the whole membrane τ_{eff} and the mean residence time in the pore of mean diameter τ_{m} is caused by the disproportionately high contributions of the large pores to the total membrane flux. Consequently, the Bodenstein number of the mean pore size Bo_{m} has limited relevance, because it corresponds to a fluid velocity u_{m} smaller than the effective mean velocity u_{eff}. This explains why in Figure 4.4(a), the resulting Bo_{eff} with PSD even slightly exceeds Bo_{m} for the mean pore size.

A representative reference pore size d_{ref} has to be defined in such a way, that its mean residence time corresponds to the mean residence time of the membrane. It can be determined from the resulting $\tau_{\mathrm{eff}}/\tau_{\mathrm{m}}$ as given in Figure 4.4 by means of Equations 4.8 and 4.9 resulting in

$$\frac{\tau_{\mathrm{eff}}}{\tau_{\mathrm{m}}} = \left(\frac{u_{\mathrm{ref}}}{u_{\mathrm{m}}}\right)^{-1} = \left(\frac{d_{\mathrm{ref}}}{d_{\mathrm{m}}}\right)^{-2}. \tag{4.21}$$

If the effective Bodenstein numbers are compared with those of a single channel with the reference pore size d_{ref} rather than with the mean pore size, the deviation observed in Figure 4.4 disappears and even for small values Bo_{eff} does not exceed Bo_{ref}.

A functional correlation between Bo_{ref} and the corresponding Bo_{eff} can be obtained by calculating Bo_{eff} for several values of Bo_{ref} and fitting the parameters of a suitable function, as shown in Figure 4.5. An excellent agreement can be obtained by applying the following single-parameter function:

$$Bo_{\mathrm{eff}} = \frac{58.6 \cdot Bo_{\mathrm{ref}}}{58.6 + Bo_{\mathrm{ref}}}. \tag{4.22}$$

For small values of Bo_{ref}, i.e. strong dispersion, Bo_{eff} is equal to Bo_{ref}, implying that effective dispersion is solely based on axial dispersion. For large values of Bo_{ref} on the other hand, Bo_{eff} is significantly lower than Bo_{ref}. It approaches a maximum value of $Bo_{\mathrm{PSD}} = 58.6$, which is caused by the pore size distribution, even if axial diffusion is completely negligible. In other

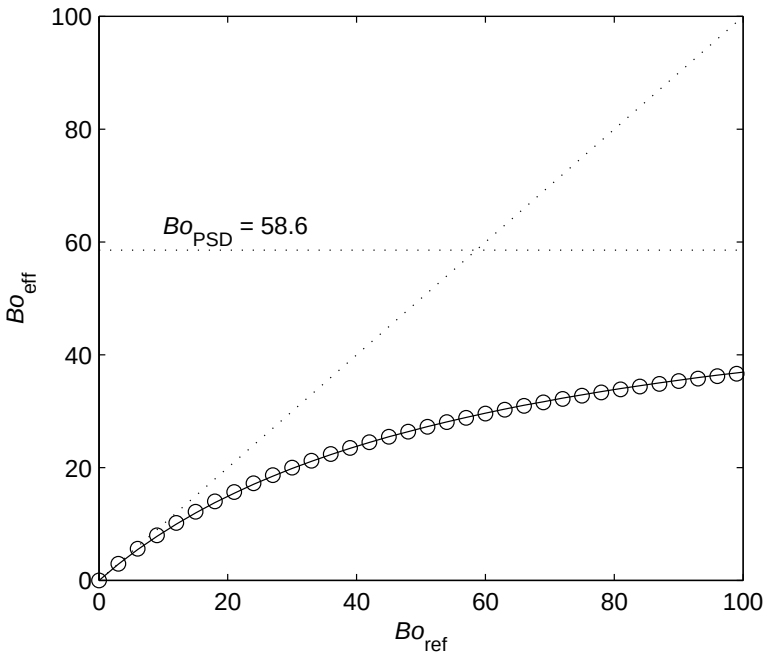

Figure 4.5: Bo_{eff} as a function of Bo_{ref} for given PSD of W02 membrane

terms, the correlation can be rewritten to

$$\frac{1}{Bo_{\mathrm{eff}}} = \frac{1}{Bo_{\mathrm{ref}}} + \frac{1}{Bo_{\mathrm{PSD}}}. \tag{4.23}$$

This way it becomes obvious, that the effective dispersion depends on axial diffusion and pore size distribution in equal measure and that it can be calculated comparably to a parallel circuit of electric resistances. The parameter Bo_{PSD} and the reference pore size d_{ref} can directly be determined from the pore size distribution by varying the parameter Bo in Equation 4.18 to best fit the pulse response of a plug flow reactor with pore size distribution, as described in Subsection 4.1.1.

Regarding the best operating conditions of the catalytic membrane reactor, the narrowest RTD and consequently the highest selectivity can be achieved at the lowest effective dispersion. This means that high pressure and high axial velocity are desirable. As the resulting pressure drop limits the economic feasibility of the process, a reasonable optimum can be determined

based on Figure 4.5. An imaginable limit for increasing the axial velocity would for example be given by arbitrarily defining the condition, where axial diffusion and pore size distribution contribute equally to the effective dispersion as optimum, that is $Bo_{\mathrm{ref}} = Bo_{\mathrm{PSD}} = 58.6$, resulting in $Bo_{\mathrm{eff}} = 29.3$ for a single membrane reactor.

4.2 Pressure Drop and Microeffects

The small dimensions in the range of micrometers and below, resulting in avoidance of diffusive limitations, are the main characteristics that discriminate the concept of flow-through catalytic membrane reactors from conventional catalytic reactors. Two contrary effects stem from this miniaturization: On the one hand, the pressure drop caused by laminar flow through a channel is inversely proportional to the square of the channel diameter, resulting in potentially very high pressure drop. On the other hand, the channel dimensions are in the order of the mean free path of the reactants, especially if the reactor is operated close to ambient pressure. This causes unfamiliar effects compared to the conventional theory based on a continuum of fluid. These two phenomena and their effects on reactor behavior are discussed in this section.

4.2.1 Flow Regimes in Microchannels

Flow and heat transfer characteristics of a gas flowing in microchannels cannot be adequately predicted by the correlations and theories developed for conventionally sized channels (Rostami et al., 2002). Due to the small characteristic dimensions present in the investigated membrane, the behavior of the system may show deviations from classical continuum theory. In microstructures, size and surface effects play a much stronger role than in macroscopic dimensions leading to phenomena such as intensified heat and mass transfer or Knudsen and molecular diffusion.

Momentum and energy transport in a fluid as well as convergence to a thermodynamic equilibrium occur due to intermolecular collisions (Karni-

Table 4.2: Flow regimes according to Knudsen number

Flow regime	Knudsen range
Continuum flow	$Kn \leq 0.01$
Slip flow	$0.01 < Kn < 0.1$
Transition flow	$0.1 < Kn < 10$
Free-molecular flow	$10 \leq Kn$

adakis et al., 2005). The average distance travelled by molecules between two collisions is known as the mean free path λ. For example for air at standard conditions the mean free path is $\lambda = 6.5 \cdot 10^{-8}$ m.

If the channel dimensions are in the order of the mean free path, wall collisions become more probable than intermolecular collisions, resulting in different fluid behavior than in a continuum. The key parameter to describe the relative importance of fluid and wall collisions is the Knudsen number, defined as the ratio between the mean free path and the channel diameter d

$$Kn = \frac{\lambda}{d}. \tag{4.24}$$

As λ and thus Kn is inversely proportional to the pressure, non-continuum effects are known from high-vacuum technology, producing the term 'rarefaction effects'.

Table 4.2 displays the different flow regimes that are defined according to the value of Kn (Karniadakis et al., 2005). In continuum flow regime the continuum hypothesis is valid and the Navier-Stokes equations properly describe fluid flow. Most published works dealing with microreactors assume the validity of the Navier-Stokes equations. For microchannels larger than 30 µm the flow can be described by conventional theory and laminar to turbulent transition is governed by the conventional rule $Re \approx 2500$. Gas is modelled as continuum, in liquids rarefaction does not occur in microchannels (Gokhale et al., 2005). The slip flow regime received its name from the apparent invalidity of the no-slip boundary condition at the walls, due to the fact that the thickness of the boundary layer is not negligible compared to the channel diameter. In the transition flow regime, molecule-molecule and molecule-wall

interactions are equally important, whereas in the free-molecular flow regime finally molecule-molecule interactions become negligible.

In a flow-through membrane reactor with a mean pore size of 0.2 µm the resulting Knudsen number for air at standard conditions is $Kn \approx 0.3$, corresponding to the transition flow regime. This has the effect that pressure drop, shear stress, heat flux and corresponding mass flow rate cannot be predicted properly from flow and heat transfer models based on the continuum hypothesis (Karniadakis et al., 2005). Numerical simulation is difficult as the standard assumptions of Navier-Stokes equations do not apply at submicrometer scales, while the computational times of applicable molecular-dynamics codes become exorbitant (Roy et al., 2003). Based on the slip flow theory, some applicable extensions to the conventional equations will be introduced to characterize the flow through catalytic membranes in both slip flow and transition regime.

4.2.2 Pressure Drop in Catalytic Membrane Reactors

The pressure drop caused by fluid flow through a reactor is commonly calculated by the following equation:

$$\Delta p = \xi \frac{\rho u^2}{2} \frac{L}{d} \tag{4.25}$$

For laminar flow in circular pipes the friction factor ξ is a function of the Reynolds number $\xi = 64/Re$, yielding the Hagen-Poiseuille equation. With an average pressure in the pore of $p_{\mathrm{av}} = 0.5 \cdot (p_{\mathrm{feed}} + p_{\mathrm{permeate}})$ and assuming ideal gas behavior, the corresponding flow rate through the circular pipe amounts to

$$\dot{n}_{\mathrm{p}} = \frac{\pi d^4 p_{\mathrm{av}}}{128 \eta R T L} \Delta p. \tag{4.26}$$

In the slip flow regime, convection is superimposed by a net flow resulting from Knudsen diffusion, leading to an increased total flow for equal pressure drop compared to continuum theory or a reduced pressure drop for equal flow, respectively. This reduced pressure drop is coherent with a reduced wall friction due to wall slip. The difference can be accounted for by a correction

factor, being a function of the Knudsen number and allowing for the use of the conventional flow equations. This correction is calculated from the Navier-Stokes equations with slip flow boundary conditions and accurately predicts the pressure drop for gas flow in microchannels at low Reynolds numbers (Papautsky et al., 2001).

Karniadakis et al. (2005) propose a unified model for pipe flow which is valid for the whole Knudsen regime. The resulting effective flow rate $\dot{n}_{\text{eff}}$ can be given as a correction factor to the one obtained for continuum flow $\dot{n}_{\text{cont}}$. For the different flow regimes molecular, transition and slip flow the following equations apply:

$$\frac{\dot{n}_{\text{mol}}}{\dot{n}_{\text{cont}}} = 1 + 5.5Kn, \tag{4.27}$$

$$\frac{\dot{n}_{\text{trans}}}{\dot{n}_{\text{cont}}} = 1 + 5Kn, \tag{4.28}$$

$$\frac{\dot{n}_{\text{slip}}}{\dot{n}_{\text{cont}}} = 1 + 4Kn. \tag{4.29}$$

In all cases Kn represents the Knudsen number at the average absolute pressure in the channel p_{av}.

Knudsen and laminar contributions

The permeance of a membrane made up of isoporous circular channels can be calculated for a continuum of fluid from Equation 4.26 by multiplication with the total number of pores

$$N_{\text{tot}} = \frac{4\epsilon A_{\text{mem}}}{\pi d_{\text{p}}^2}. \tag{4.30}$$

Additionally the tortuosity factor τ can be introduced, as the ratio between the real distance covered by a molecule passing the membrane and the membrane thickness, allowing for deviations from linear channel geometry. The laminar contribution to the permeance finally becomes

$$\frac{\dot{n}_{\text{mem}}}{A_{\text{mem}}\Delta p} = \frac{\epsilon}{\tau}\frac{d^2}{32\eta RTL}p_{\text{av}}. \tag{4.31}$$

Accounting for rarefaction effects with the Knudsen correction for slip flow regime (Equation 4.29) yields two contributions to the total permeance

$$P_{\text{tot}} = P_{\text{laminar}} + P_{\text{Knudsen}}, \tag{4.32}$$

$$P_{\text{laminar}} = \frac{\epsilon}{\tau}\frac{d^2}{32\eta RTL}p_{\text{av}}, \tag{4.33}$$

$$P_{\text{Knudsen}} = \frac{\epsilon}{\tau}\frac{4\lambda d}{32\eta RTL}p_{\text{av}}. \tag{4.34}$$

According to kinetic gas theory, the ratio between mean free path and viscosity is a function of pressure p, temperature T and molar weight M (Bird et al., 2001):

$$\frac{\lambda}{\eta} = \frac{3}{p}\sqrt{\frac{\pi RT}{8M}}. \tag{4.35}$$

This ratio is inversely proportional to the absolute pressure, resulting in an independence of pressure for the Knudsen contribution to the total permeance (Equation 4.34). The Chapman-Enskog correlation used in some publications (Roy et al., 2003) produces the same proportionality with somewhat different numbers. As is the case with the mean free path, the definition of the viscosity is based on the continuum hypothesis, thus its validity may be questionable in the slip flow and transition regime (Sabry, 2000). Assuming the same relationship towards the channel diameter for both parameters, the ratio given in Equation 4.35 remains constant. Combining Equation 4.35 with a Knudsen correction factor of 9 yields the numerical values used by Lin and Burggraaf (1991), which are also applied for the permeance method in the work at hand (Equation 3.2).

Comparison of Membrane Reactor Structures

The structural difference between anodized and sintered alumina membranes is illustrated in Section 3.1. For non-catalytic sintered membranes a tortuosity of $\tau \approx 2$ has been determined, whereas for anodized membranes SEM images confirm the existence of straight channels with a tortuosity of $\tau \approx 1$. Assuming an equivalent model of straight circular channels with the length of membrane thickness multiplied by tortuosity, the tortuosity can be incor-

porated into the friction factor ξ, yielding

$$\xi = \tau \cdot \frac{64}{Re}. \tag{4.36}$$

The resulting pressure drop for flowing through a sintered membrane is twice as high as that of an anodized membrane of the same porosity, pore diameter and thickness. However, the mean hydrodynamic residence time inside the catalytic pores is equal, as it only depends on flow rate and porosity.

As a different approach, a sintered membrane can be regarded as fixed bed reactor made up of small particles in the scale of the resulting pore sizes. For a fixed bed of spherical particles, the following relationship between particle size and hydraulic diameter of an equivalent circular channel can be calculated:

$$d_{\text{part}} = \frac{3}{2}\frac{(1-\epsilon)^2}{\epsilon} d_{\text{hyd}}. \tag{4.37}$$

For estimation of the pressure drop in a fixed bed reactor, the so-called Ergun equation is frequently used (Baerns et al., 1999). In the common connotation it refers to particle diameter and superficial velocity of the empty tube. Using channel diameter and channel velocity instead, the following friction factor can be determined, corresponding to Equation 4.25:

$$\xi = \frac{4}{3(1-\epsilon)}\left(1.75 + \frac{100}{Re(1-\epsilon)}\right). \tag{4.38}$$

For low Reynolds numbers the term 1.75 is negligible. The main difference between the two equations is that Equation 4.36 uses the tortuosity τ to account for non-ideal geometry, whereas Equation 4.38 is only a function of the porosity ϵ. The resulting pressure drop is equal for the case

$$\tau_{\text{equivalent}} \approx \frac{2}{(1-\epsilon)^2}. \tag{4.39}$$

For a porosity of $\epsilon = 0.4$ the equivalent tortuosity is $\tau_{\text{equivalent}} = 5.56$, which means that in case of the real tortuosity of $\tau \approx 2$, the Ergun equation predicts an almost three times higher pressure drop than Equation 4.36.

Neither correlation takes into account rarefaction effects, which can be

incorporated using the appropriate Knudsen correction. Combining Equation 4.36 for pressure drop and tortuosity with Equation 4.28 for the Knudsen correction in transition regime yields a correlation that properly predicts the pressure drop caused by flowing through an anodized membrane for a tortuosity of $\tau = 1$ and that of the applied sintered membranes for $\tau = 2$:

$$\Delta p = \frac{64}{Re}\frac{L}{d}\frac{\rho u^2}{2}\frac{\tau}{(1+5Kn)} = \frac{32\eta u L}{d^2}\frac{\tau}{(1+5Kn)}. \tag{4.40}$$

For small pore diameters in catalytic membrane reactors, the pressure drop can be a limiting factor. Comparison of differently structured membranes results in an increased reactor efficiency for the anodized membranes compared to the sintered membranes by a factor of τ.

4.2.3 Dispersion in Transition Regime

As mentioned in Section 4.1.2, axial dispersion in microchannels is exclusively based on axial diffusion, meaning that radial velocity profiles in the microchannels do not affect the axial dispersion coefficient. If the membrane reactor is operated at low pressures, that is in the transition or slip flow regime, the molecular diffusion is superimposed by Knudsen diffusion (Section 4.2.2). The resulting effective diffusion coefficient is a combination of the molecular diffusion coefficient and the Knudsen diffusion coefficient:

$$D_{\text{mol}} = \frac{1}{3}\bar{u}\lambda, \tag{4.41}$$

$$D_{\text{Kn}} = \frac{1}{3}\bar{u}d = \frac{D_{\text{mol}}}{Kn}, \tag{4.42}$$

$$D_{\text{eff}} = \frac{1}{1/D_{\text{mol}} + 1/D_{\text{Kn}}} = \frac{D_{\text{mol}}}{1+Kn}. \tag{4.43}$$

Figure 4.6 shows the effective diffusion coefficient of nitrogen at room temperature in microchannels with a diameter of 0.2 µm as a function of the absolute pressure. For $p \geq 10^6$ Pa, corresponding to $Kn = 0.03$ the influence of Knudsen diffusion can be neglected, whereas for $p \leq 10^3$ Pa, corresponding to $Kn = 32$, diffusion is completely dominated by Knudsen

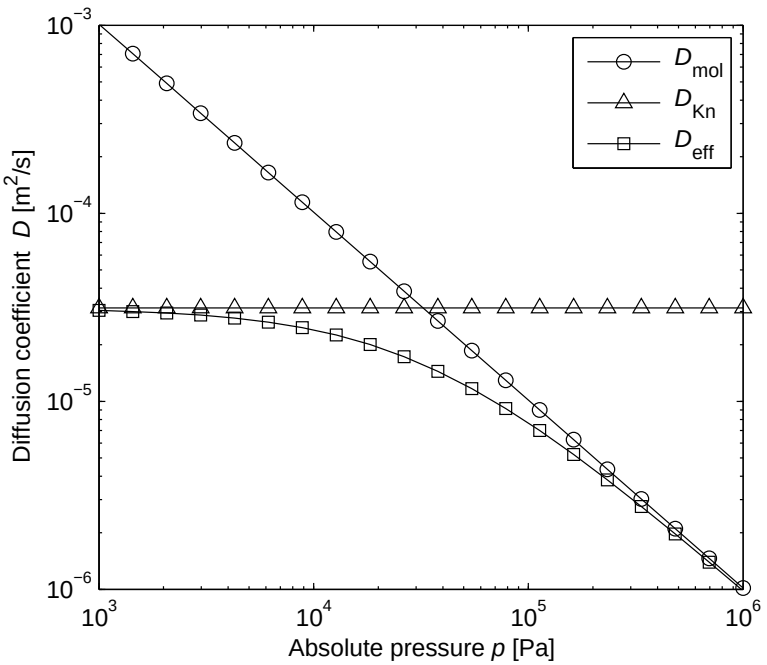

Figure 4.6: D_{eff} for nitrogen in 0.2 µm microchannels at room temperature

diffusion. At ambient pressure ($Kn = 0.3$) the effective diffusion coefficient deviates from the molecular diffusion coefficient by almost 25 %, leading to an increase of *Bo* by 32 % for the same flow-through velocity compared to axial dispersion caused by molecular diffusion only.

In addition, rarefaction effects at increased Knudsen numbers also reduce the pressure drop across the membrane according to Equation 4.40. Both effects improve the reactor behavior in terms of the achievable Bodenstein number as a function of the transmembrane pressure drop in the slip flow and transition regime. Figure 4.7 shows the dependence between *Bo* and transmembrane pressure drop in microchannels with a length of $L = 60\,\mu\text{m}$ and a diameter of $d = 0.2\,\mu\text{m}$ at room temperature.

In Figure 4.7(a), the influence of rarefaction effects is demonstrated for nitrogen with ambient pressure on the permeate side, comparing the achievable Bodenstein numbers with those for the model liquid water, which shows no rarefaction effects. For low pressure drops ($\Delta p < 0.5 \cdot 10^5\,\text{Pa}$) rarefaction increases *Bo* by a factor of 2 and more, nevertheless the resulting *Bo* is

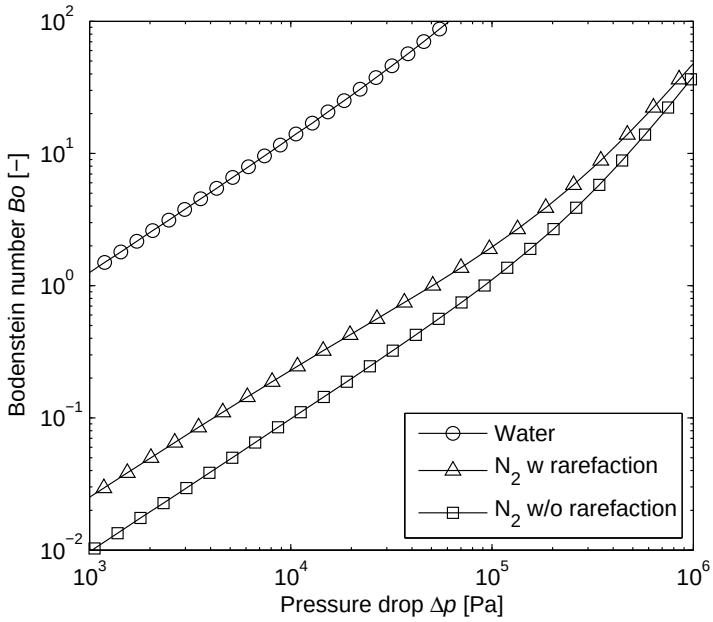

(a) Comparison of nitrogen with rarefaction, nitrogen without rarefaction and water for ambient pressure on the permeate side

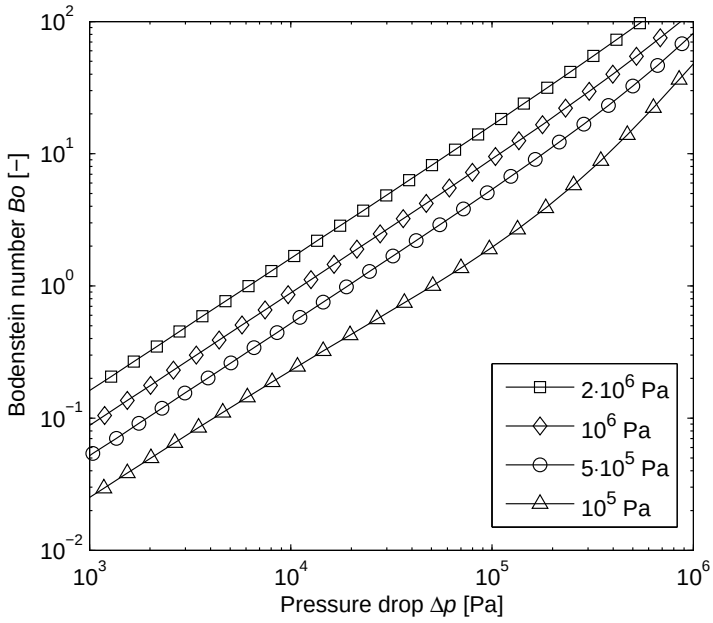

(b) Nitrogen with rarefaction for different permeate pressures

Figure 4.7: Relationship between Bodenstein number and transmembrane pressure drop for $L = 60\,\mu\text{m}$ and $d = 0.2\,\mu\text{m}$ at room temperature

smaller than 1, corresponding to a rather wide residence time distribution. To achieve higher values of $Bo > 10$, a pressure drop of $\Delta p > 4 \cdot 10^5$ Pa is required, corresponding to a feed pressure of $p_{\text{feed}} > 5 \cdot 10^5$ Pa. In this range the influence of rarefaction is significantly lower. The figure also demonstrates that for liquid reactants the influence of axial dispersion can be reduced much easier, producing almost ideal plug flow behavior with $Bo > 100$ already for a pressure drop as low as $\Delta p = 0.6 \cdot 10^5$ Pa.

Figure 4.7(b) shows that the influence of axial dispersion for gas phase reactions can most easily be reduced by increasing the absolute pressure. As described above, for a permeate pressure of $p_{\text{permeate}} = 1 \cdot 10^5$ Pa a feed pressure of $p_{\text{feed}} > 5 \cdot 10^5$ Pa is required to achieve $Bo > 10$. For a permeate pressure of $p_{\text{permeate}} = 20 \cdot 10^5$ Pa instead the required feed pressure is only slightly higher with $p_{\text{feed}} = 21 \cdot 10^5$ Pa.

Summarizing the above, to reduce the influence of axial dispersion, either the flow-through velocity or the absolute pressure have to be increased. At low pressures, rarefaction effects have a positive influence, but the achievable Bodenstein number is low. Increasing the velocity quickly leads to prohibitive transmembrane pressure drops. Reasonable values of Bo can only be realized for higher absolute pressures, where rarefaction is negligible.

4.3 Conclusions

The residence time distribution provides important information about the hydrodynamic behavior of a reactor. As a direct measurement of the RTD is hardly possible for the investigated reactor concept, a reactor model is created, which allows for calculation of the RTD taking into account deviations from an ideal plug flow reactor caused by pore size distribution and axial dispersion.

The influence of the pore size distribution is demonstrated by treating a number of pore size classes as parallel plug flow reactors. The total flow is distributed into the pores of different sizes in such a way that the pressure drop in all pores will be equal. Due to a dependence of the flow per pore on the fourth power of the pore diameter, even smaller deviations from the

mean pore size are amplified resulting in a relatively wide RTD, which is nevertheless far from CSTR behavior. Flowing through several membranes in sequence reduces the width of the RTD at the cost of increased pressure drop.

The influence of axial dispersion in a single pore is calculated by means of the dimensionless Bodenstein number $Bo = uL/D_{\mathrm{ax}}$. The width of the resulting RTD strongly depends on axial velocity and absolute pressure.

Both influences can be combined into an effective dispersion model with the single parameter Bo_{eff}. Bo_{eff} is a function of the Bodenstein number of the reference pore size Bo_{ref}, which takes into account axial flow velocity, reactor length and molecular diffusion coefficient, and of the equivalent Bodenstein number Bo_{PSD}, characterizing the pore size distribution without axial diffusion.

For strong dispersion caused by low axial velocities and absolute pressures, the influence of the pore size distribution is negligible. Increasing velocity and/or pressure reduces the axial dispersion, resulting in a narrower RTD. At the same time the influence of the pore size distribution grows, limiting the minimum achievable effective dispersion. For the given pore size distribution a limit of $Bo_{\mathrm{PSD}} = 58.6$ is determined. A reasonable point of operation can be achieved for $Bo_{\mathrm{ref}} = Bo_{\mathrm{max}} = 58.6$ with a resulting $Bo_{\mathrm{eff}} = 29.3$. For an absolute pressure of $p = 10^6$ Pa the required axial velocity in the reference pore amounts to $u_{\mathrm{ref}} = 1\,\mathrm{m/s}$, causing a pressure drop of approximately $\Delta p = 5 \cdot 10^5$ Pa.

Due to the small dimensions of the pore channels, microeffects may play a significant role. The pressure drop caused by flowing through a catalytic membrane can be calculated using the established Hagen-Poiseuille correlation with correction factor taking into account tortuosity and rarefaction effects. Especially at low absolute pressures, the pressure drop is reduced compared to continuum theory. Comparing a sintered and an anodized membrane, the pressure drop in the sintered membrane is higher due to the pronounced tortuosity.

Axial dispersion is also influenced by rarefaction for gas flows at pressures below 10^6 Pa. Higher Knudsen numbers exert a positive effect on the Boden-

stein number compared to continuum theory, but cannot compensate for the high diffusivity present at low pressures. Thus, if the reactor is operated at higher pressure or even in liquid phase, much higher Bodenstein numbers can be reached at equal pressure drop. As described above, the reduction of dispersion to reach a possibly narrow residence time distribution is limited by the pore size distribution of the membrane.

Chapter 5

Reactor Performance

Conversion, selectivity and temperature profiles in the membrane reactor under different operating conditions can be predicted by means of suitable reactor models. Reaction kinetics of the applied hydrogenation reactions are determined by fitting kinetic parameters of power rate laws to experimental results obtained with the membrane reactor setup, assuming ideal PFTR behavior. For assessment of catalytic activity and heat transfer, the unselective ethene hydrogenation is performed. The partial hydrogenation of ethyne to ethene with the undesired by-product ethane is applied as indirect verification of the shape of the residence time distribution in the catalytic membrane reactor. The performance of the membrane microchannel reactor is experimentally compared to that of a randomly structured membrane reactor and to equivalent fixed beds of ground catalytic membranes.

5.1 Reaction Kinetics

Available literature covering reaction kinetics for ethyne or ethene hydrogenation has been discussed in Subsection 3.3.1, leading to the decision to discard a detailed kinetic analysis based on the assumed heterogeneous reaction mechanism in favor of a simple formal kinetic approach with validity only within the range of performed experiments. Thus, a general power rate law is applied with an Arrhenius approach to account for the tempera-

ture dependence of the rate constants. The reaction volume of the catalytic membrane reactor is limited to the volume of accessible pores. Due to the small dimensions the reaction is considered quasi-homogeneous, assuming equal catalyst loading in each pore (Adler, 2000). If operated in a regime with low effective dispersion (Section 4.1.3), the simplifying assumption of an isoporous plug-flow reactor is justifiable. For reasons of model simplicity, constant axial velocity and temperature are assumed. As the number of moles is reduced during the reaction, the assumption of constant velocity is a strong simplification for low dilution and high conversions. Also at high ratios of transmembrane pressure drop to absolute pressure, the axial velocity varies significantly. But if the reaction is performed at increased pressure and dilution or with low conversions, the error is negligible. The assumption of an isothermal reactor is justified if the permeate temperature rather than the feed temperature is applied as reactor temperature, as will be explained in Section 5.2.

5.1.1 Ethene Hydrogenation

Details of the hydrogenation of ethene to ethane catalyzed by palladium are discussed in Subsection 3.3.1. All experiments are carried out with stoichiometric feed of the reactants ethene and hydrogen, with the result that their concentrations are equal at all times. This procedure does not allow for exact determination of the reaction kinetics, but it reduces the number of kinetic parameters compared to Equation 3.9 as the two individual reaction orders can be replaced by a total reaction order. Applying an Arrhenius expression for temperature dependence, a three parameter kinetic rate law is supposed. The kinetic parameters are determined by applying an ideal isoporous PFTR reactor model with varying reactant concentrations. The isobaric and isothermal differential material balance is solved applying the MATLAB-solver ode45 for ordinary differential equations. The model parameters are fit to experimentally measured conversions using a least squares method (Equations 5.1 to 5.4). The corresponding experiments are performed applying an anodized catalytic membrane with available cat-

Table 5.1: Ethene hydrogenation kinetics: Reaction conditions and measured conversions compared to model predictions

$x_{C_2H_4}$	Q_{tot} [l_N/min]	$Q_{C_2H_4}$ [l_N/min]	p_{feed} [10^5 Pa]	T [K]	X_{exp}	X_{sim}
0.50	0.80	0.40	1.00	572	0.77	0.80
0.50	1.50	0.75	1.03	537	0.67	0.67
0.50	2.50	1.25	1.09	477	0.51	0.54
0.40	1.00	0.40	1.02	531	0.71	0.71
0.40	1.88	0.75	1.06	505	0.60	0.57
0.40	3.13	1.25	1.15	454	0.47	0.46
0.33	1.20	0.40	1.04	481	0.62	0.63
0.33	2.25	0.75	1.11	466	0.52	0.49
0.33	3.75	1.25	1.24	429	0.41	0.40
0.29	1.40	0.40	1.06	447	0.55	0.56
0.29	2.63	0.75	1.16	433	0.45	0.43
0.29	4.38	1.25	1.34	410	0.34	0.36

alyst mass of 0.14 mg to a stoichiometric feed of reactants. The operating conditions in combination with the observed and the simulated conversions are given in Table 5.1.

$$r_{C_2H_4} = -k_\infty \ \exp(-E_A/RT) \ p^n_{C_2H_4} \tag{5.1}$$

$$n = 1.8 \tag{5.2}$$

$$\begin{aligned} k_\infty &= 3.75 \cdot 10^4 \ \text{mol/(kg}_{\text{cat}} \text{ s bar}^n) \\ &= 3.75 \cdot 10^{-5} \ \text{mol/(kg}_{\text{cat}} \text{ s Pa}^n) \end{aligned} \tag{5.3}$$

$$E_A = 2\,001 \ \text{J/mol.} \tag{5.4}$$

The best agreement between experiment and model is reached for a reaction order of $n = 1.8$ (Figure 5.1), which is much larger than the value of $1.45 - 0.85 = 0.6$ reported in Equation 3.9.

The determined temperature dependence is rather low with an activation energy of $E_A = 2\,001$ J/mol. Compared to the reaction kinetics given in Equation 3.9 with a corresponding value of $E_A = 40\,600$ J/mol, determined

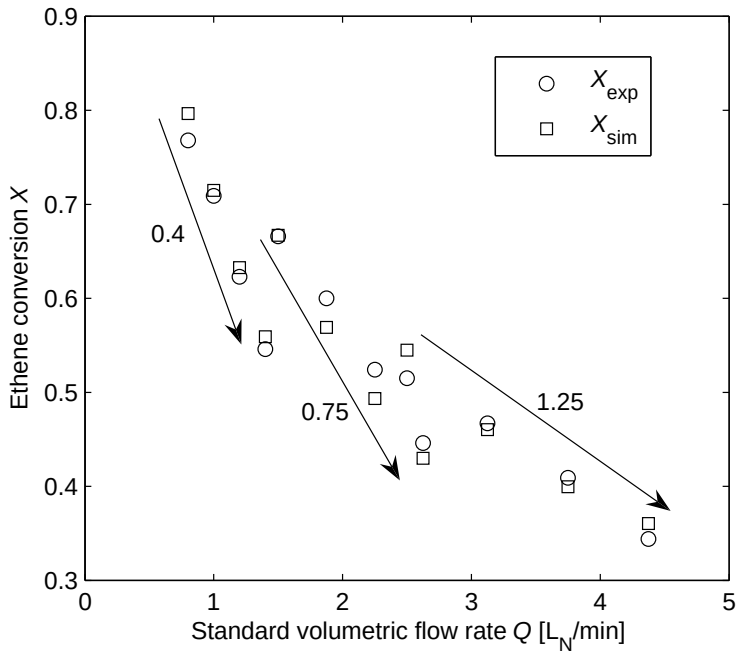

Figure 5.1: Experimental and calculated conversions for ethene hydrogenation with stoichiometric feed of reactants. The numbers represent the standard flow rate of ethene, with the arrows pointing in direction of increasing N_2 dilution

for higher dilutions and at lower temperatures, the temperature influence is much less significant. This allows for the assumption that under the applied conditions not the reaction step itself but rather the adsorption and desorption steps limit the reaction kinetics, calling for application of a Langmuir-Hinshelwood type approach, if reaction kinetics with validity for a wider range of parameters are required. This mechanistic approach implies additional parameters such as sorption constants with a temperature dependence of their own, which may even lead to decreasing reaction rates at increasing temperatures. For the sake of simplicity, the power law approach is favored at this point, bearing in mind its limited validity beyond the conditions of the performed experiments.

The resulting reaction rates for the applied experimental conditions obtained with the determined power rate law are several orders of magnitude higher than those obtained hypothetically with the rate law given in Equa-

tion 3.9. However, as the experimental conditions are not comparable and the power law kinetics are only valid in a small region of operating parameters, this result is no conclusive evidence regarding increased catalytic activity.

5.1.2 Ethyne Hydrogenation

The selective hydrogenation of ethyne to ethene with the undesired by-product ethane catalyzed by palladium is discussed in Subsection 3.3.1. At stoichiometric feed of reactants and low excess factors of hydrogen, an oligomerization reaction generates C_{4+} components, which can plug the membrane pores by forming a liquid film with high capillary pressure, frequently called "green oil". This undesired side reaction is avoided by performing the reactions with a large excess of hydrogen and nitrogen dilution. To reduce the large number of kinetic parameters, the reactions are performed at a constant permeate temperature of $T_{\text{perm}} = 443\,\text{K}$. For constant reactor pressure, the large excess of hydrogen would allow for treating the hydrogen concentration as constant, further reducing the number of rate parameters. But as pressure has been identified as an important parameter regarding axial dispersion, all four exponents of the kinetic approach specified in Equations 3.12 and 3.13 remain to be quantified.

Kinetic experiments are performed applying a catalytic membrane with an available catalyst mass of $m_{\text{cat}} = 1.35 \cdot 10^{-7}\,\text{kg}$ to a reactant mixture with a molar reactant ratio of $C_2H_2 : H_2 : N_2 = 1 : 10 : 19$. Reactor pressure and total flow rate are varied according to Table 5.2. Once again, an isoporous ideal plug flow reactor model is applied. The isobaric and isothermal differential material balance is solved applying the MATLAB-solver ode45 for ordinary differential equations. The six corresponding kinetic parameters (Equations 5.5 and 5.6) are determined by a least squares method fitting their values to the experimentally measured conversions and selectivities as displayed in Figure 5.2.

Table 5.2: Ethyne hydrogenation kinetics for $T = 443\,\mathrm{K}$ with a molar reactant ratio of $C_2H_2 : H_2 : N_2 = 1 : 10 : 19$. Reaction conditions, measured conversions and selectivities compared to model predictions

$x_{C_2H_2}$	Q_{tot} [l_N/min]	p_r [10^5 Pa]	T [K]	X_{exp}	X_{sim}	S_{exp}	S_{sim}
0.033	0.9	1.99	442.0	0.89	0.88	0.10	0.06
0.033	1.8	1.98	442.5	0.86	0.84	0.15	0.10
0.033	3.6	1.99	442.2	0.75	0.78	0.16	0.15
0.033	5.4	2.01	443.7	0.69	0.73	0.19	0.20
0.033	7.2	1.97	442.3	0.72	0.69	0.25	0.25
0.033	9.0	1.99	444.9	0.66	0.66	0.28	0.28
0.033	9.0	2.00	442.0	0.66	0.66	0.27	0.29
0.033	0.9	4.02	444.0	0.91	0.91	0.07	0.04
0.033	1.8	4.01	443.6	0.88	0.87	0.08	0.05
0.033	3.6	4.01	442.3	0.79	0.82	0.09	0.08
0.033	5.4	4.02	444.0	0.76	0.79	0.10	0.11
0.033	7.2	3.96	444.0	0.84	0.76	0.09	0.13
0.033	0.9	5.03	443.0	0.91	0.91	0.06	0.03
0.033	1.8	4.99	442.7	0.89	0.88	0.07	0.04
0.033	3.6	4.99	442.3	0.79	0.84	0.07	0.07
0.033	5.4	4.98	443.9	0.78	0.80	0.08	0.09
0.033	7.2	4.99	444.6	0.81	0.78	0.08	0.11

$$
\begin{aligned}
r_{C_2H_2} &= -k_1\, p_{C_2H_2}^{m_1}\, p_{H_2}^{n_1} && (5.5)\\
m_1 &= 3.3\\
n_1 &= -2.6\\
k_1(443\,\mathrm{K}) &= 5.532 \cdot 10^3\ \mathrm{mol/(kg_{cat}\ s\ Pa^{m_1+n_1})},\\
r_{C_2H_6} &= k_2\, p_{C_2H_4}^{m_2}\, p_{H_2}^{n_2} && (5.6)\\
m_2 &= 2.8\\
n_2 &= -1.1\\
k_2(443\,\mathrm{K}) &= 0.1478\ \mathrm{mol/(kg_{cat}\ s\ Pa^{m_2+n_2})}.
\end{aligned}
$$

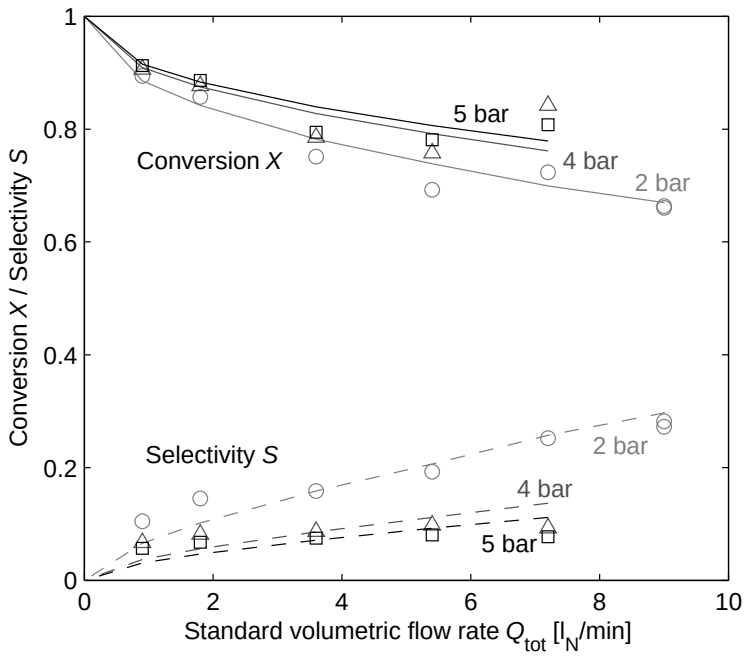

Figure 5.2: Experimental and calculated conversions and selectivities for ethyne hydrogenation at $T = 443\,\mathrm{K}$ with a molar reactant ratio of $C_2H_2 : H_2 : N_2 = 1 : 10 : 19$

For the hydrogenation of ethyne to ethene a total reaction order of 0.7 is obtained, whereas the reaction order of the consecutive hydrogenation to ethane of 1.7 closely corresponds to the one determined in Subsection 5.1.1. As the reaction order of the partial hydrogenation is smaller than the reaction order of the consecutive reaction, increasing pressure reduces the reaction selectivity. In both partial reactions, the reaction order of hydrogen is negative, which means that the reaction is inhibited by high H_2 concentrations. This effect is especially pronounced for the partial hydrogenation reaction and also explains the overall low selectivities obtained under large excess of hydrogen. The negative exponents for hydrogen partial pressures determined for the applied power rate law indicate that sorption mechanisms play an important role in this heterogeneous reaction network, calling for a Langmuir-Hinshelwood type approach, if validity in a wider range of operating conditions is required.

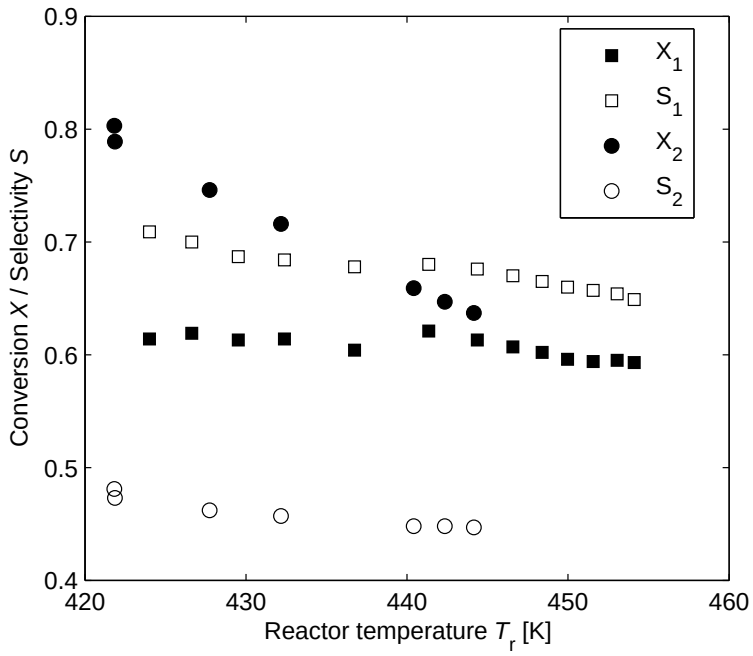

Figure 5.3: Ethyne hydrogenation conversion and selectivity as a function of reactor temperature for two operating points ($p = 1.1 \cdot 10^5\,\mathrm{Pa}$, $Q_{C_2H_2} = 0.1\,\mathrm{l_N/min}$)
Experiment 1 (squares): $C_2H_2 : H_2 : N_2 = 1 : 4 : 16$
Experiment 2 (circles): $C_2H_2 : H_2 : N_2 = 1 : 8 : 21$

Compared to the kinetic rates obtained by Bos and Westerterp (1993) given in Equation 3.10, a completely different pressure dependence of selectivity is determined. Bos and Westerterp observe a higher total reaction order for the partial hydrogenation reaction, predicting a selectivity increase at higher pressures. In both investigations the reaction order of hydrogen is higher for the consecutive reaction, resulting in a reduction of selectivity for increasing excess of hydrogen.

The reaction selectivity is proportional to the ratio of the kinetic rate constants of desired and undesired reaction. If the activation energies of the two reactions are different, the selectivity changes with temperature. Experiments performed with constant pressure and molar flow rates under variation of reactor temperature yield an at first sight surprising result: Both conversion and selectivity decrease when the reactor temperature increases

(Figure 5.3).

A feasible explanation for the decrease of conversion is the temperature dependence of the sorption isotherms. If the reaction rate is limited by the coverage of the catalytically active surface, increasing temperature reduces the coverage and thus the overall reaction rate, even though the reaction itself is accelerated. Simultaneous increase of selectivity and conversion is only possible if the kinetics change. As the temperature dependence of the undesired reaction is stronger than that of the desired reaction, selectivity decreases with increasing temperatures.

Comparable to the reaction kinetics determined for ethene hydrogenation (Subsection 5.1.1), the temperature dependence observed for both partial reactions is rather low, especially if compared to the pronounced pressure dependence.

5.2 Heat Transfer in Catalytic Membrane

In the previous section a constant temperature of reactor and reactants has been assumed, simplifying the determination of kinetic parameters. This assumption is not self-evident taking into account the strongly exothermal reactions and the temperature difference between feed and permeate. For the investigated hydrogenation reactions the adiabatic temperature rise

$$\Delta T_{\mathrm{ad}} = \frac{x_{\mathrm{HC}} \cdot (-\Delta H_{\mathrm{R,HC}})}{c_p} \tag{5.7}$$

can easily exceed 1000 K if operated at low dilution ratios.

Microstructured reactors outstand for their superior heat and mass transfer properties compared to conventional reactors. Heat transfer across an interface of gas and wall $\dot{Q}_{\mathrm{trans}}$ is proportional to the temperature difference $T_{\mathrm{gas}} - T_{\mathrm{wall}}$, the surface area of the interface A_{transfer} and a heat transfer coefficient h according to

$$\dot{Q}_{\mathrm{trans}} = h \cdot A_{\mathrm{transfer}} \cdot (T_{\mathrm{gas}} - T_{\mathrm{wall}}) \,. \tag{5.8}$$

Heat generation by chemical reaction on the other hand is proportional to the reactor volume or in case of heterogeneous reactions to the amount of catalyst. By reducing the diameter of a channel, the ratio between channel surface and volume increases, leading to improved heat transfer. However, even more important is another effect: For a constant Nusselt number, describing the ratio between heat transfer and heat conduction, the heat transfer coefficient h is inversely proportional to the channel diameter d, leading to extremely high heat transfer coefficients in microstructured reactors. Additionally the laminar flow profile in microchannels can be neglected, assuming plug flow as reactor model, because strong diffusive radial mixing efficiently counteracts concentration or temperature profiles (Knösche, 2005).

Regarding the anodized membrane geometry, the nano-scale porous structure promises highly efficient heat transfer between gas and pore walls. On the other hand, the limited external surface area of the almost two-dimensional flat sheet membrane does not allow for heat removal in radial direction. On the feed side, the membrane can be regarded exclusively in contact with the feed gas, on the permeate side, heat can be transferred to the porous metal support and further to the external surface of the reactor module.

This section aims at determining an axial temperature profile along the membrane reactor and corresponding heat transfer coefficients by combining experimental measurements with a non-isothermal reactor model, in order to analyze and predict reactor temperatures under given conditions. As only heat generation caused by the chemical reaction is of interest, all measurements are performed with the hydrogenation of ethene as model reaction as described in Section 5.1 and with equal catalyst loading.

5.2.1 Isoporous PFTR Model with Heat Transfer

Assuming identical pores, the investigated model system can be reduced to a single pore and the surrounding pore wall, with symmetry in radial direction. For small concentration gradients inside the pore in radial direction due to intensive radial mixing, a quasi-homogeneous reaction with plug flow can be assumed (Xu and Platzer, 2001). The plug flow assumption reduces the

complexity to a single dimension, in which gas temperature, wall temperature and gas composition will be treated as separate variables. Pressure drop is neglected and fluid properties are assumed to be constant along the reactor. Especially for high axial velocities, low absolute pressures, low dilution and high conversion, this is a major simplification, as strong pressure and velocity gradients may arise. Nevertheless neglecting these parameters allows to focus on heat transfer processes and should lead to at least qualitatively useful correlations.

Material Balance

A steady state differential material balance of ethene yields

$$\frac{dX_{\mathrm{C_2H_4}}}{dZ} = -\frac{r_{\mathrm{C_2H_4}}}{x_{\mathrm{C_2H_4,feed}}} = \frac{m_{\mathrm{cat}}}{\dot{n}_{\mathrm{tot}}} k \cdot p^n \cdot x_{\mathrm{C_2H_4,feed}}^{(n-1)} \cdot (1 - X_{\mathrm{C_2H_4}})^n. \tag{5.9}$$

This equation implies the conversion of ethene $X_{\mathrm{C_2H_4}}$ with the simplification

$$X_{\mathrm{C_2H_4}} = 1 - \frac{\dot{n}_{\mathrm{C_2H_4}}}{\dot{n}_{\mathrm{C_2H_4,feed}}} \approx 1 - \frac{x_{\mathrm{C_2H_4}}}{x_{\mathrm{C_2H_4,feed}}}. \tag{5.10}$$

The reaction kinetics according to Equation 5.1 are transformed to a dimensionless term, assuming constant pressure and molar flow rate

$$r_{\mathrm{C_2H_4}} = -\frac{m_{\mathrm{cat}}}{\dot{n}_{\mathrm{tot}}} k \cdot \left(p_{\mathrm{C_2H_4,feed}} \left(1 - X_{\mathrm{C_2H_4}}\right)\right)^n. \tag{5.11}$$

Catalyst mass and molar flow rate can be calculated either for a single pore or for the whole membrane.

Gas Phase Energy Balance

To determine axial profiles of gas and pore wall temperature, two separate energy balances are applied, which are coupled by the heat transfer term between gas and pore wall. In both balances all radial profiles are neglected. A steady state differential energy balance for a volume element $A \cdot dz$ takes into account convective heat transfer $\dot{Q}_{\mathrm{conv}}$ into and out of the control volume, heat conduction $\dot{Q}_{\mathrm{cond}}$ in and against flow direction, heat transfer between

gas and pore wall $\dot{Q}_{\text{trans}}$ and heat generation by chemical reaction $\dot{Q}_{\text{react}}$. The effective axial heat conduction incorporates all axial mixing processes (Stief et al., 1998).

$$-\frac{\partial \dot{Q}_{\text{conv}}}{\partial z} dz - \frac{\partial \dot{Q}_{\text{cond}}}{\partial z} dz - \dot{Q}_{\text{trans}} + \dot{Q}_{\text{react}} = 0 \tag{5.12}$$

The single terms can be calculated as follows:

$$\dot{Q}_{\text{conv}} = \dot{n}_{\text{tot}} \cdot c_p \cdot T, \tag{5.13}$$

$$\dot{Q}_{\text{cond}} = -A \cdot k_{\text{gas}} \cdot \frac{\partial T_{\text{gas}}}{\partial z}, \tag{5.14}$$

$$\dot{Q}_{\text{trans}} = h \cdot (T_{\text{gas}} - T_{\text{wall}}) \cdot \pi d \cdot dz, \tag{5.15}$$

$$\dot{Q}_{\text{react}} = \Delta H_{\text{R}} \cdot \dot{n}_{\text{tot}} \cdot \frac{\partial x_{\text{C}_2\text{H}_4}}{\partial z} \cdot dz. \tag{5.16}$$

Introducing dimensionless length $Z = z/L$ and temperature $\Theta = T/T_0$ as well as ethene conversion according to Equation 5.10, several parameters can be cropped, forming dimensionless quantities: The Nusselt number

$$Nu = \frac{h \cdot \pi d L^2}{A \cdot k_{\text{gas}}} \tag{5.17}$$

describes the ratio between heat transfer and heat conduction in the gas phase. It is important to note, that heat transfer is proportional to the pore wall surface $\pi d L$, whereas heat conduction is proportional to the cross-section area of the pore $A = \pi/4\ d^2$. The Péclet number

$$Pe = \frac{\dot{n} \cdot c_p \cdot L}{A \cdot k_{\text{gas}}} \tag{5.18}$$

characterizes the ratio between heat convection and heat conduction in the gas phase. The dimensionless adiabatic temperature difference

$$\Delta\Theta_{\text{ad}} = -\frac{\Delta H_{\text{R}} \cdot x_{\text{C}_2\text{H}_4,\text{feed}}}{c_p \cdot T_0} \tag{5.19}$$

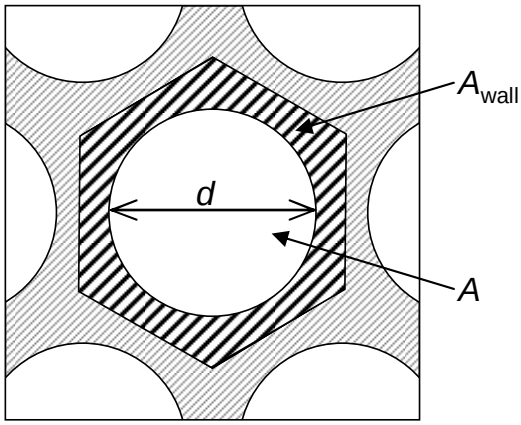

Figure 5.4: Axial membrane cross-section with pore area A and allocated wall area A_{wall}

is normalized to the reference temperature T_0. The energy balance for the gas phase results as:

$$\frac{d^2\Theta_{\text{gas}}}{dZ^2} = Pe \cdot \frac{d\Theta_{\text{gas}}}{dZ} + Nu \cdot (\Theta_{\text{gas}} - \Theta_{\text{wall}}) - Pe \cdot \Delta\Theta_{\text{ad}} \cdot \frac{dX_{\text{C}_2\text{H}_4}}{dZ}. \tag{5.20}$$

Pore Wall Energy Balance

The accessible membrane area A_{mem} can be subdivided into total pore area $A_{\text{mem,pore}}$ and total wall area $A_{\text{mem,wall}}$ according to the porosity ϵ:

$$A_{\text{mem}} = A_{\text{mem,pore}} + A_{\text{mem,wall}} = \epsilon \cdot A_{\text{mem}} + (1 - \epsilon) \cdot A_{\text{mem}}. \tag{5.21}$$

The cross-sectional area of wall material A_{wall} of a single pore, characteristic for heat conduction is calculated by allocating the same amount of wall material to each pore according to

$$A_{\text{wall}} = \frac{1 - \epsilon}{\epsilon} \cdot A, \tag{5.22}$$

assuming identical heat transfer characteristics in each pore and thus no radial heat transfer between the walls of the different pores (Figure 5.4).

The steady state differential energy balance for a volume element of the pore wall $A_{\text{wall}} \cdot dz$ takes into account heat conduction $\dot{Q}_{\text{cond}}$ in and against

flow direction and heat transfer between gas and pore wall $\dot{Q}_{\text{trans}}$:

$$-\frac{\partial \dot{Q}_{\text{cond}}}{\partial z} dz + \dot{Q}_{\text{trans}} = 0. \tag{5.23}$$

Note that in contrast to the gas phase energy balance, the heat transfer is declared as positive. The single terms can be calculated as follows:

$$\dot{Q}_{\text{cond}} = -\frac{1-\epsilon}{\epsilon} \cdot A \cdot k_{\text{wall}} \cdot \frac{\partial T_{\text{wall}}}{\partial z} \tag{5.24}$$

$$\dot{Q}_{\text{trans}} = h \cdot (T_{\text{gas}} - T_{\text{wall}}) \cdot \pi d \cdot dz. \tag{5.25}$$

Again, a dimensionless quantity can be introduced. The Biot number

$$Bi = \frac{\epsilon}{1-\epsilon} \frac{h \cdot \pi d L^2}{A \cdot k_{\text{wall}}} \tag{5.26}$$

characterizes the ratio between heat transfer and heat conduction in the pore wall. Heat transfer is proportional to the pore wall surface πdL, whereas heat conduction is proportional to the allocated cross-section area of the pore wall A_{wall} as described in Equation 5.22.

The energy balance for the pore wall results as:

$$\frac{d^2\Theta_{\text{wall}}}{dZ^2} = -Bi \cdot (\Theta_{\text{gas}} - \Theta_{\text{wall}}). \tag{5.27}$$

Boundary Conditions

The reactor model consists of the three coupled differential equations 5.9, 5.20 and 5.27 with the variables $X_{C_2H_4}$, Θ_{gas} and Θ_{wall}. The energy balances are second order differential equations and the material balance is of first order. This leads to a boundary value problem, requiring five boundary conditions.

The boundary condition for the material balance is rather simple, as the conversion of ethene is assumed to be zero at the pore entrance due to neglect of axial dispersion

$$X_{C_2H_4}(Z = 0) = 0. \tag{5.28}$$

Energy balances at the pore entrance for both gas phase and pore wall lead to the well-known boundary conditions proposed by Danckwerts (1953)

$$\Theta_{\text{gas}}(Z=0) = 1 + \frac{1}{Pe} \cdot \frac{d\Theta_{\text{gas}}}{dZ}(Z=0), \tag{5.29}$$

$$\Theta_{\text{wall}}(Z=0) = 1 + \frac{1}{Bi_0} \cdot \frac{d\Theta_{\text{wall}}}{dZ}(Z=0). \tag{5.30}$$

They allow for a temperature step between feed temperature T_0 and gas and wall temperatures at $Z = 0$. As the feed temperature is chosen as reference temperature, the dimensionless feed temperature $\Theta_{\text{feed}} = 1$ appears in the boundary conditions.

For the pore wall energy balance, the Danckwerts boundary condition results from the consideration of axial heat transfer from the membrane and should not be confused with a convective term. A Biot number for the pore entrance

$$Bi_0 = \frac{h_0 \cdot L}{k_{\text{wall}}} \tag{5.31}$$

appears as additional dimensionless quantity, which differs from the Biot number defined in Equation 5.26 not only by the characteristic length, but also by the heat transfer coefficient h_0, as the heat transfer characteristics are different inside a channel and at the front face of the channel.

Boundary conditions 4 and 5 define the heat transfer behavior at the pore exit. Two different models are discussed at this stage. As a first assumption, temperature steps similar to those at the entrance are also allowed at the exit. This assumption is feasible, if the catalytic membrane is cooled from the exit side. The corresponding boundary conditions completing model 1 are

$$\Theta_{\text{gas}}(Z=1) = \Theta_{\text{permeate}} - \frac{1}{Pe} \cdot \frac{d\Theta_{\text{gas}}}{dZ}(Z=1), \tag{5.32}$$

$$\Theta_{\text{wall}}(Z=1) = \Theta_{\text{permeate}} - \frac{1}{Bi_1} \cdot \frac{d\Theta_{\text{wall}}}{dZ}(Z=1). \tag{5.33}$$

The Biot number at the pore exit Bi_1 is defined correspondingly to Equation 5.31. It has to be noted, that the dimensionless permeate temperature

Θ_{permeate} is not known if the model is predictive.

If the gas and wall temperature at the pore exit are close to the permeate temperature, heat conduction as well as heat transfer from the pore wall to the reactor module can be neglected. In this case, the temperature gradients at $Z = 1$ turn to zero, yielding the classical Danckwerts boundary conditions also at the exit, completing model 2:

$$\frac{d\Theta_{\text{gas}}}{dZ}(Z = 1) = 0, \tag{5.34}$$

$$\frac{d\Theta_{\text{wall}}}{dZ}(Z = 1) = 0. \tag{5.35}$$

This assumption is a severe simplification, especially if the catalytic membrane is actively cooled. The two models differ in the temperature gradients allowed at the exit. Nevertheless, both of them are suitable to describe the reactor behavior under the applied experimental conditions, as will be demonstrated for model 2. They even produce identical temperature profiles. Thus, in the following, only the results of model 2 will be presented for reasons of convenience. It does not require knowledge of the permeate temperature, neither of the additional parameter Bi_1, with the result that all heat removal is attributed to Bi_0.

5.2.2 Parameter Study for Heat Transfer Model

The general model derived in Section 5.2.1 allows for different temperature profiles, depending on the numerical values of the model parameters. The developed reactor model includes the dimensionless quantities Nu, Pe, and Bi as parameters, which are functions of material properties and operating parameters and can thus be calculated in advance. The unknown parameter Bi_0 characterizes the heat removal from the membrane.

As an exemplary result, Figure 5.5 shows the resulting profiles for the case that all dimensionless parameters are equal to one. This means that the heat transfer in the pore is equal to the heat transfer on the feed side, to the heat conduction in the gas phase, to the heat conduction in the pore wall and to the heat convection. No heat transfer is assumed on the permeate side

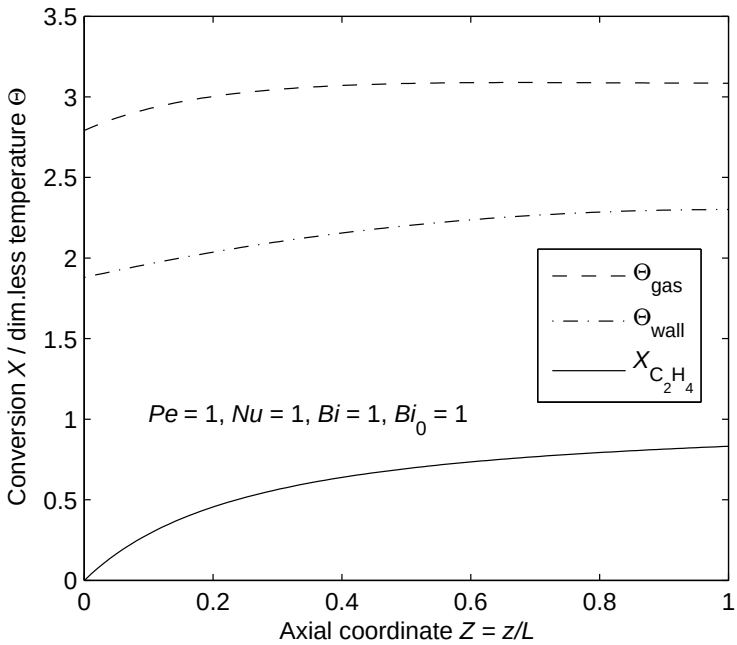

Figure 5.5: Axial profiles of conversion, gas and wall temperature for $T_{\text{feed}} = 387\,\text{K}$, $p = 10^5\,\text{Pa}$, $Q_{\text{tot}} = 0.8\,\text{l}_\text{N}/\text{min}$ and $x_{\text{C}_2\text{H}_4} = 0.5$

according to Subsection 5.2.1. These conditions do not represent a specific point of operation of the investigated reactor, but demonstrate the general profiles and the influence of the single parameters. The conversion is based on the reaction kinetics determined in Section 5.1 and corresponds to the conditions of the first experiment in Table 5.1, although the dimensionless quantities are chosen deliberately.

The dimensionless feed temperature is defined to be $\Theta_{\text{feed}} = 1$. The resulting temperature jump at the reactor inlet to $\Theta_{\text{gas}}(Z = 0) = 2.8$ (Figure 5.5) is very pronounced and proportional to the temperature gradient at the same point according to Equation 5.29. The wall temperature is far below the gas temperature, but well above the feed temperature. This order is fixed, because the reaction heat is generated in the gas phase, transferred to the pore wall and from the feed side of the pore wall to the surrounding reactor module, following temperature differences. At $Z = 1$, both temperature gradients turn to zero, as defined in Equations 5.34 and 5.35. The gas

temperature increases by 59 % of the adiabatic temperature rise, signifying that 41 % of the generated heat is removed from the reactor.

In Figure 5.6 the same model is calculated four times, varying only one of the four parameters Pe, Nu, Bi and Bi_0. In each case the respective parameter is set to 10. For equal catalyst concentration, the conversion is a function of the total flow rate, which is proportional to Pe. For better comparability this proportionality is neglected by assuming an adjusted catalyst mass, leading to comparable conversions and thus comparable heat generation.

The case $Nu = 10$ signifies that internal heat transfer between gas and pore walls is intensified compared to heat conduction in the gas. Due to mutual dependence of the dimensionless quantities, this implies intensified heat transfer on the feed side and heat conduction in the pore wall compared to heat convection. Due to the good heat conduction in the solid, a nearly isothermal profile of the wall temperature is achieved. The intensified heat transfer in the pore does not allow for large temperature differences between pore wall and gas phase. The result is a much smaller difference between gas and wall temperature at a much lower level compared to Figure 5.5. The gas temperature reaches a maximum short after the reactor inlet, where heat generation still is high but the influence of heat removal on the feed side has decreased. 87 % of the generated heat is removed from the reactor.

The case $Pe = 10$ corresponds to intensified heat convection compared to heat conduction in the gas phase as well as to internal and external heat transfer and heat conduction in the pore wall. Only 20 % of the generated heat is removed from the reactor, leading to very high gas temperatures close to the adiabatic temperature. The poor conductivities generate pronounced temperature profiles. For a very short interval at the reactor inlet, the wall temperature is even slightly higher than the gas temperature due to heat conduction in the pore wall from the warmer zones in the rest of the reactor.

For $Bi = 10$, internal heat transfer in the pore is intensified compared to heat conduction in the pore wall. This implies intensified heat convection and heat conduction in the gas phase compared to external heat transfer on the feed side. Similar to the case $Nu = 10$ the intensive heat transfer in the pore accounts for small temperature difference between gas and wall. The

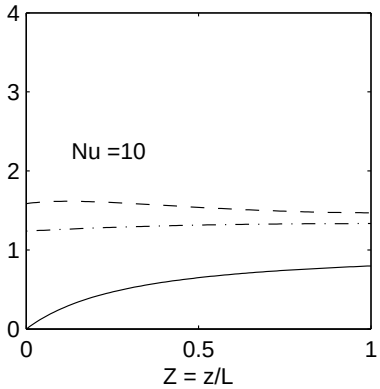

(a) $Nu = 10, Pe = Bi = Bi_0 = 1$

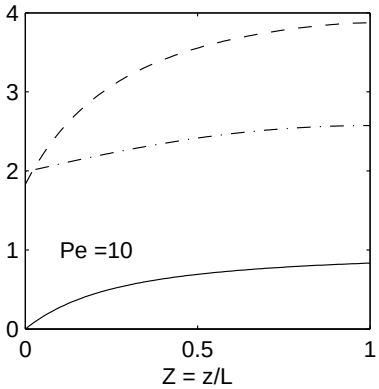

(b) $Pe = 10, Nu = Bi = Bi_0 = 1$

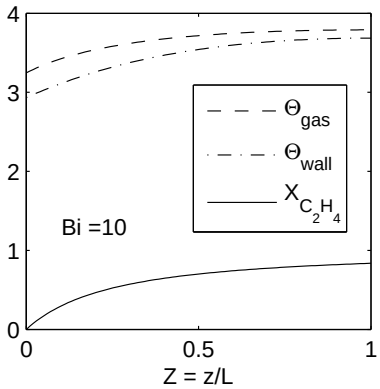

(c) $Bi = 10, Nu = Pe = Bi_0 = 1$

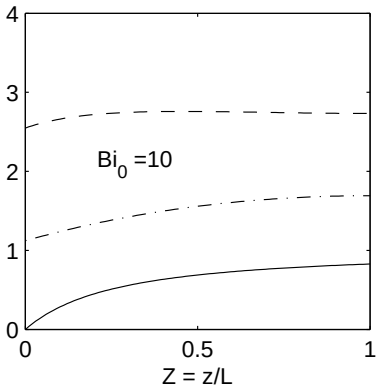

(d) $Bi_0 = 10, Nu = Pe = Bi = 1$

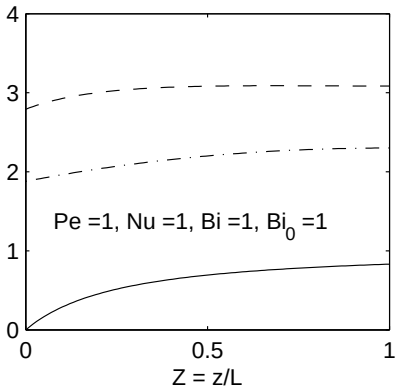

(e) $Nu = Pe = Bi = Bi_0 = 1$

Figure 5.6: Influence of model parameters on axial profiles of conversion, gas and wall temperature for $T_{\text{feed}} = 387\,\text{K}$, $p = 10^5\,\text{Pa}$, $Q_{\text{tot}} = 0.8\,\text{l}_\text{N}/\text{min}$ and $x_{\text{C}_2\text{H}_4} = 0.5$; (b) amount of catalyst increased to compensate for reduced residence time

heat removal rate on the other hand is much smaller with only 22 % due to the reduced heat transfer on the feed side. The temperature jump at the reactor inlet is the most pronounced of all cases.

Finally, $Bi_0 = 10$ signifies that the external heat transfer on the feed side is intensified compared to heat conduction in the pore wall, as well as to heat conduction in the gas phase, heat convection and and internal heat transfer. Nevertheless the heat removal rate is rather low with a value of 52 %, due to poor internal heat transfer from gas phase to pore wall. The dimensionless wall temperature at $Z = 0$ is close to 1, but the difference between gas and wall temperature is comparable to Figure 5.5.

The discussion demonstrates that for a given system, the parameters cannot be varied independently. Each of the four dimensionless quantities significantly influences the temperature profiles. For an assessment of the real reactor behavior, reasonable ranges for the parameter values are determined.

Heat Transfer Coefficient and Nusselt Number

The heat transfer coefficient h, which appears in the dimensionless quantities Nu and Bi, represents the proportionality factor for heat transfer between gas and pore wall. For various conditions it can be calculated by means of Nusselt correlations. For laminar flow through a circular channel assuming constant wall temperature, the mean Nusselt number $\overline{Nu}_\mathrm{d} = h \cdot d/k_\mathrm{gas}$ is a function of the factor $Re \cdot Pr \cdot d/L$ (Gnielinski, 2006). For very low Reynolds numbers present in sub-micron channel diameters, the factor becomes very small and the correlation asymptotically reaches the value $Nu_d = 3.66$ (Knösche, 2005).

However, for a given Nusselt number the heat transfer coefficient h is inversely proportional to the channel diameter. Hence, at small sizes, surprisingly high values are obtained (Sabry, 2000). For the given geometry of the anodized membrane pores and a thermal conductivity of $k_\mathrm{gas} \approx 0.03\,\mathrm{W/(mK)}$ the heat transfer coefficient h reaches a value of

$$h = 3.66 \cdot \frac{k_\mathrm{gas}}{d} > 5 \cdot 10^5\,\mathrm{W/(m^2K)}. \tag{5.36}$$

Owing to the small channel dimension, heat transfer in microchannels is

much better than in channels of conventional size. For modelling gas micro heat exchangers, a value of $h = 1\,000\,\mathrm{W/(m^2K)}$ is commonly assumed (Stief et al., 1998), which already represents a rather high value compared to macrochannels. Recently, values up to $35\,000\,\mathrm{W/(m^2K)}$ are reported for micro heat exchangers (Stankiewicz, 2004). With pore diameters smaller than one micrometer, it seems quite probable, that heat transfer coefficients even exceed these values as calculated in Equation 5.36.

It has to be noted that for laminar flow in small channels, correct Nusselt numbers are generally smaller than those calculated applying normal size relations (Sabry, 2000). The deviation increases with smaller channels, with a stronger dependence for liquids than for gases. For the Nusselt number Nu defined in Equation 5.17, the characteristic length is different from the one used in $\overline{Nu}_d$. With a length to diameter ratio of $L/d = 300$ as present in the pore channels of the applied anodized membranes, applying the macroscale relation (Equation 5.36) results in

$$Nu = \frac{h \cdot \pi d L^2}{A \cdot k_{\mathrm{gas}}} = 1.3 \cdot 10^6. \tag{5.37}$$

Even if this number has to be reduced by several orders of magnitude, any temperature difference between gas and wall inside the membrane pore would immediately disappear.

Thermal Conductivity and Biot Numbers

The thermal conductivity of the membrane material k_{wall} is a material property and a function of temperature. For sintered Al_2O_3 at room temperature, values of $k_{\mathrm{wall}} = 33\,\mathrm{W/(mK)}$ are given, decreasing to $11.4\,\mathrm{W/(mK)}$ at $T = 500\,^\circ\mathrm{C}$ (Munro, 1997). At low material thickness, the thermal conductivity is reported to decrease. For aluminium oxide thin films with a thickness of around $0.3\,\mu\mathrm{m}$ lower values of $3.3\,\mathrm{W/(mK)}$ have been determined (Kato et al., 2001; Bai et al., 2008), indicating amorphous rather than crystalline structure.

Axial heat conduction is inversely proportional to the channel length.

For the small reactor length of $L = 60\,\mu\text{m}$ the axial heat conduction is pronounced even for isolating materials. Assuming the high value of $k_{\text{wall}} = 20\,\text{W/(mK)}$ for the anodized alumina membranes at $T = 200\,°\text{C}$ and the heat transfer coefficient calculated in Equation 5.36, the resulting Biot number is

$$Bi = \frac{\epsilon}{1-\epsilon}\frac{h \cdot \pi d L^2}{A \cdot k_{\text{wall}}} \approx 500. \tag{5.38}$$

Smaller values of k_{wall} lead to a further increase of Bi, whereas a reduced h proportionally reduces Bi. If the real heat transfer coefficient is smaller than the one given in Equation 5.36 by a factor of 10, the Biot number is still larger than 50, corresponding to very intensive heat transfer between gas and pore wall compared to heat conduction in the wall.

The heat transfer coefficient h_0 in Bi_0, which characterizes heat transfer at the feed side of the membrane, is assumably much smaller than the one for heat transfer in the pores. Even for a high value of $h_0 = 1\,000\,\text{W/(m}^2\text{K)}$, the Biot number does not exceed a value of

$$Bi_0 = \frac{h_0 \cdot L}{k_{\text{wall}}} = 3 \cdot 10^{-3}, \tag{5.39}$$

which signifies that due to the small channel length, heat conduction in the pore wall is much larger than heat transfer on the feed side.

Flow Rate and Péclet Number

The Péclet number is proportional to the convective heat transport and thus to the flow rate in the pores. It can be calculated either with the flow rate through a single pore divided by the cross-sectional area of the pore or with the total flow rate divided by the open membrane area, producing equal values. The total standard volumetric flow rates applied in the heat transfer experiments are varied between $Q_{\text{tot}} = 1 - 5\ \text{l}_\text{N}/\text{min}$. This corresponds to molar flow rates of $\dot{n}_{\text{tot}} = 0.74 \cdot 10^{-3} - 3.72 \cdot 10^{-3}\,\text{mol/s}$. For a mean molar heat capacity of $c_p = 53\,\text{J/(molK)}$ and a mean thermal conductivity of $k_{\text{gas}} = 0.03\,\text{W/(mK)}$ (both valid for ethene at 400 K), the resulting Péclet

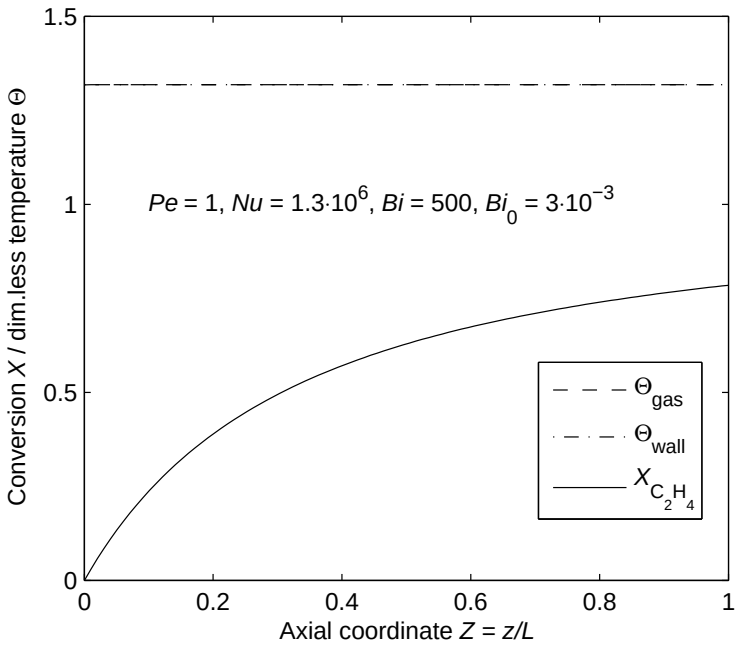

Figure 5.7: Axial profiles of conversion, gas and wall temperature for $T_{\text{feed}} = 387\,\text{K}$, $p = 10^5\,\text{Pa}$, $Q_{\text{tot}} = 0.8\,\text{l}_\text{N}/\text{min}$ and $x_{\text{C}_2\text{H}_4} = 0.5$ and parameters determined for the catalytic membrane reactor

number range is

$$Pe = \frac{\dot{n}_{\text{tot}} \cdot c_p \cdot L}{A_{\text{mem}} \cdot k_{\text{gas}}} = 0.54 - 2.68. \tag{5.40}$$

These values show that heat convection and heat conduction in the fluid are in the same order of magnitude.

Temperature Profile in the Catalytic Membrane

With the dimensionless quantities determined beforehand for the anodized catalytic membrane reactor, the resulting profiles of temperatures and conversion are illustrated in Figure 5.7. The temperatures of gas and wall turn out to be identical and the reactor can be regarded isothermal.

Parameter variation yields further interesting results: The Stanton number St (Eq. 5.41) characterizes the ratio between heat transfer in the pore and heat convection. For values of $St > 1\,000$, gas and wall temperature are

always in complete agreement and the reactor temperature is constant:

$$St = \frac{Nu}{Pe} = \frac{h \cdot A_{\text{int}}}{\dot{n}_{\text{tot}} \cdot c_p} \overset{!}{\geq} 1\,000 \tag{5.41}$$

$$A_{\text{int}} = \frac{4L}{d} \cdot \epsilon A_{\text{mem}}, \tag{5.42}$$

with the internal surface area of the membrane A_{int}. The correlation implies that the high value for Nu determined in Equation 5.37 is not mandatory. For the same Péclet number of $Pe = 1$ a Nusselt number of $Nu = 1\,000$ is already sufficient to achieve isothermal behavior. Accordingly, for the determined value of $Nu > 10^6$ the flow rate could be increased by orders of magnitude, proportionally increasing Pe, without changing the shape of the temperature profiles.

The second observation concerns the resulting reactor temperature. If Equation 5.41 is fulfilled, the permeate temperature, which can be measured experimentally, is equal to both gas and wall temperature along the whole membrane length. All four dimensionless quantities used in the model influence the exact value of the reactor temperature, but these influences can be merged into a single dimensionless quantity, the external Stanton number St_0

$$St_0 = \frac{Nu}{Pe}\frac{Bi_0}{Bi} = \frac{h_0 \cdot (1-\epsilon) A_{\text{mem}}}{\dot{n}_{\text{tot}} \cdot c_p}. \tag{5.43}$$

An integral energy balance of the reactor demonstrates that the parameter St_0 is sufficient to describe the reactor temperature:

$$\dot{n}_{\text{tot}} c_p (T_{\text{feed}} - T_{\text{perm}}) - h_0 (1-\epsilon) A_{\text{mem}} (T_{\text{wall}}(0) - T_{\text{feed}}) + \dot{n}_{\text{tot}} c_p \Delta T_{\text{ad}} X(1) = 0, \tag{5.44}$$

$$1 - \Theta_{\text{permeate}} - St_0 \cdot (\Theta_{\text{wall}}(0) - 1) + \Delta\Theta_{\text{ad}} \cdot X(1) = 0. \tag{5.45}$$

If isothermal behavior can be assumed ($St \geq 1\,000$), the inlet wall temperature $\Theta_{\text{wall}}(Z = 0)$ and the permeate temperature Θ_{permeate} are equal and can be replaced by the reactor temperature Θ_{r}. This resulting reactor temperature is a function of the heat generation term $\Delta\Theta_{\text{ad}} \cdot X(1)$ and of

St_0:

$$\Theta_\mathrm{r} = 1 + \frac{\Delta\Theta_\mathrm{ad} \cdot X(1)}{1 + St_0}. \tag{5.46}$$

As $St \geq 1\,000$ is always fulfilled for the anodized catalytic membrane reactor, the isothermal reactor temperature is only a function of a single unknown parameter, which can be determined experimentally by measuring temperature difference and conversion.

With these correlations it is worth to look once more at the temperature profiles in Figure 5.6. The case $Nu = 10$ corresponds to $St = St_0 = 10$, $Pe = 10$ signifies $St = St_0 = 0.1$, $Bi = 10$ equals to $St = 1, St_0 = 0.1$ and finally $Bi_0 = 10$ means $St = 1, St_0 = 10$. Thus for neither of the four cases, Equation 5.41 is fulfilled, leading to non-isothermal profiles. $Nu = 10$ comes closest, whereas $Pe = 10$ is far away from this constraint, producing pronounced temperature profiles. Regarding reactor temperature, $Nu = 10$ and $Bi = 10$ demonstrate effective heat removal with $St_0 = 10$, whereas in the other two cases heat removal is poor with $St_0 = 0.1$, leading to permeate temperatures close to the adiabatic temperature.

The heat transfer reactor model based on these theoretical considerations will be validated experimentally in the following subsection with the aim of determining a correlation for the parameter St_0, which would allow for prediction of reactor temperature and consequently conversion.

5.2.3 Experimental Validation

The unknown parameter St_0 characterizes heat removal from the membrane. If the system complies with the constraint $St \geq 1\,000$, it can directly be calculated from measured conversion and temperature difference with no need for the differential model by means of Equation 5.46, which can be transformed to:

$$1 + St_0 = \frac{\Delta T_\mathrm{ad} \cdot X}{T_\mathrm{permeate} - T_\mathrm{feed}}. \tag{5.47}$$

The twelve experiments performed for determining ethene hydrogenation kinetics (compare Table 5.1) can now be applied to determine the external Stanton number from measured conversion and reactor temperature. For

Table 5.3: Determined St_0 values and resulting reactor temperatures for ethene hydrogenation experiments

$x_{C_2H_4}$	Q_{tot} [l_N/min]	X	ΔT [K]	$X \cdot \Delta T_{ad}$ [K]	$St_{0,exp}$	$T_{r,exp}$ [K]	$T_{r,sim}$ [K]
0.50	0.80	0.77	185	988	4.34	572	573
0.50	1.50	0.67	161	856	4.33	537	537
0.50	2.50	0.51	99	662	5.70	477	502
0.40	1.00	0.71	155	729	3.72	531	514
0.40	1.88	0.60	132	617	3.68	505	489
0.40	3.13	0.47	87	481	4.55	454	458
0.33	1.20	0.62	104	534	4.12	481	477
0.33	2.25	0.52	96	450	3.71	466	455
0.33	3.75	0.41	65	351	4.38	429	429
0.29	1.40	0.55	72	401	4.57	447	450
0.29	2.63	0.45	66	328	3.95	433	428
0.29	4.38	0.34	49	253	4.15	410	408
				$St_{0,fit}$ =	4.33		

each experiment an individual St_0 can be determined (Table 5.3), which exactly predicts the measured temperature. The small variation of the individually calculated values allows for the conclusion, that for the membrane reactor setup under the applied operating parameters a constant value will lead to satisfying results. Using a least squares method, a value of $St_0 = 4.33$ best fits the experimental results. The theoretical reactor temperatures calculated by means of this constant value are also given in Table 5.3. The simulated reactor temperatures $T_{r,sim}$ are generally in excellent agreement with the measured temperatures $T_{r,exp}$. In eight out of twelve experiments the deviation is lower than 5 K. The largest relative error of 5 % is obtained in the third experiment, which already produced the largest deviation in the determination of the reaction kinetics, suggesting an experimental error.

A constant value of St_0 signifies that heat removal from the reactor is not a function of the flow rate. For increasing flow rate $\dot{n}_{tot}$, the heat transfer coefficient h_0 on the feed side increases proportionally. For a rather low standard volume flow rate of $Q_{tot} = 1\,l_N/min$ the resulting heat transfer coefficient is $h_0 = 500\,W/(m^2K)$, increasing up to $5\,000\,W/(m^2K)$ for 10 l/min.

By means of St_0, which is characteristic for the membrane reactor, a constant heat removal ratio can be specified, defined as the ratio between heat removed from the reactor and heat generated in the reactor, based on Equation 5.47:

$$1 - \frac{T_{\text{permeate}} - T_{\text{feed}}}{\Delta T_{\text{ad}} \cdot X} = \frac{St_0}{1 + St_0} = 0.81. \tag{5.48}$$

This heat removal ratio means that 81 % of the heat of reaction is transferred from the reactor to the surrounding module, whereas 19 % contribute to the temperature jump at the reactor inlet, i.e. are transported convectively.

The reactor model described in this section is well suited to predict the temperature profiles of the flow-through membrane reactor. Due to the small reactor dimensions, isothermal operation will be reached under any operating conditions. In this case, an integral reactor balance allows for calculation of the reactor temperature, which is a function of feed temperature, conversion, adiabatic temperature difference and a constant dimensionless quantity St_0, which accounts for the heat removal from the reactor and is characteristic for the reactor setup.

Reaction kinetics and consequently the conversion reached in the reactor are a function of the reactor temperature. The steady state reactor temperature in turn is a function of conversion, coupled by the adiabatic temperature rise. As a result, a predictive reactor model has to calculate conversion and reactor temperature simultaneously. The resulting reactor model does not require differential energy balances and represents a boundary value problem, in which the conversion at $Z = 1$ is coupled to the constant reactor temperature according to Equation 5.46.

5.3 Reaction Selectivity

The selectivity towards the intermediate product of a sequential reaction depends on various parameters. The conversions of both partial reactions are functions of rate constant, partial pressure of the reactants and residence time. If no product appears in the reactor feed, the initial reaction rate of the

undesired reaction is 0, leading to an initial selectivity of $S = 1$. For increasing residence time, the conversion increases, which automatically results in an increased reaction rate of the undesired reaction, reducing the selectivity. If the concentration of the second reactant is not limiting and both reactions can be regarded irreversible, the selectivity towards the desired intermediate product drops to 0 after sufficient time. For a given conversion, the achievable selectivity is a function of temperature, as the two competing reactions usually show different temperature dependence. Backmixing of the intermediate product always leads to a selectivity reduction. This means that the selectivity for a given conversion in a flow-through reactor cannot exceed that of an ideal PFTR without axial dispersion. The width of the residence time distribution determines the suitability of a reactor for performing sequential reactions.

As explained in Section 4.1, the residence time distribution of an FTCMR cannot properly be measured directly. Comparing the experimentally measured selectivity for a given conversion with the theoretical one that would be obtained in an ideal PFTR is an indirect proof for the width of the residence time distribution. The effective Bodenstein number, accounting for axial dispersion and pore size distribution, as determined in Section 4.1.2, is a suitable parameter to describe the width of the RTD. The reactor temperature determines the ratio of rate constants, which accounts for the achievable selectivity at a given conversion. The membrane reactor will be described by an isothermal effective dispersion model, predicting conversion and selectivity for given operating conditions as a function of reactor temperature and Bo_{eff}.

5.3.1 Isothermal Reactor with Effective Dispersion

If more than one chemical reaction is involved, quantifying the reactant concentrations in terms of conversion becomes impractical. Thus material balances are set up for each of the reactants. The general material balance for a network of chemical reactions in a plug flow reactor with axial dispersion

with i components and j reactions results as follows:

$$\frac{\partial c_i}{\partial t} = -\frac{\partial (c_i u)}{\partial z} + D_{\text{ax}} \frac{\partial^2 c_i}{\partial z^2} + \sum \nu_{ij} R_j. \tag{5.49}$$

Analyzing only steady state and neglecting changes of pressure, molar flow rate and temperature along the channel as well as rarefaction effects, the following simplified system of material balances results:

$$\frac{dx_i}{dZ} = \frac{1}{Bo_{\text{eff}}} \frac{d^2 x_i}{dZ^2} + \sum \nu_{ij} R_j. \tag{5.50}$$

With the above assumptions, the parameter for effective dispersion Bo_{eff}, taking into account both molecular axial diffusion and pore size distribution, is constant in the whole reactor. In case of the ethyne hydrogenation a boundary value problem with a system of four second order differential equations results, requiring eight boundary conditions.

Assuming ideally mixed reactants in the volume before the membrane on the feed side, no concentration gradients appear. If the volume is sufficiently large, reactants which diffusively leave the membrane on the feed side do not alter the feed composition significantly, which is equivalent to a closed boundary. Thus, the previously discussed Danckwerts boundary conditions (Equation 5.29) apply for each component i:

$$x_i(Z = 0) = x_{i,\text{feed}} + \frac{1}{Bo_{\text{eff}}} \frac{dx_i}{dZ}(Z = 0), \tag{5.51}$$

$$\frac{dx_i}{dZ}(Z = 1) = 0. \tag{5.52}$$

Assuming power law kinetics, the dimensionless reaction rates for each reaction j can be written as:

$$r_j = \frac{m_{\text{cat}}}{\dot{n}_{\text{tot}}} \cdot p^{\sum_i n_{ij}} \cdot k_{j,\infty} \cdot \exp(-E_{\text{A},j}/RT) \cdot \prod_i x_i^{n_{ij}}. \tag{5.53}$$

As the reactor is isothermal, an energy balance is not required and the reaction rates can be calculated by specifying the constant reactor temperature. In this case the required feed temperature can be determined by means

of Equation 5.46. A different approach would be to specify the feed temperature and implicitly calculate the reactor temperature by including the same equation as additional side condition. For better comparability of the results the first approach is applied, allowing for separate analysis of the kinetic influence of temperature and of the influence of the residence time distribution on the achievable reaction selectivity.

5.3.2 Parameter Study

By adapting the flow rate to the reaction kinetics, any desired conversion can be achieved. In case of sequential reactions it is more interesting, which selectivity can be achieved for a given conversion. In the investigated system this depends on two parameters: The reactor temperature determines the respective reaction kinetics. If for example the temperature dependence of the desired reaction is stronger than that of the undesired sequential reaction, higher reactor temperatures will lead to higher selectivities. The residence time distribution, which appears in terms of Bo_{eff}, represents the second parameter. For high effective Bodenstein numbers, the influence of effective dispersion is low and the reactor behavior is close to that of an ideal PFTR. In this case, the maximum selectivity can be achieved for a given reactor temperature and conversion. For lower values of Bo_{eff} backmixing effects reduce the selectivity towards the desired intermediate product.

Figure 5.8(a) demonstrates the achievable ethene selectivities as a function of ethyne conversion for an ideal PFTR, varying reactor temperature and therefore kinetics. Due to the different temperature dependence of the two reactions, the highest selectivities can be achieved at the highest reactor temperature. At lower temperatures not only the selectivity for a desired conversion is reduced, but also the reaction rate, requiring much longer residence times to achieve the same conversion. If the reaction kinetics behave like in the described case, the reaction temperature will be chosen as high as the constraints, such as thermal degradation or material limits allow.

Figure 5.8(b) shows the achievable ethene selectivities as a function of ethyne conversion for a constant reactor temperature of $T_{\mathrm{r}} = 500\,\mathrm{K}$. For

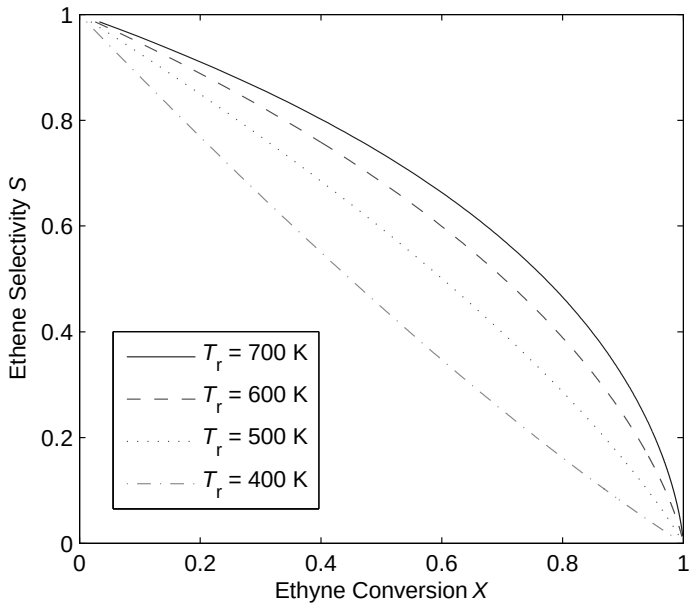

(a) Ideal PFTR ($Bo_{\mathrm{eff}} = \infty$), varying reactor temperature T_{r}

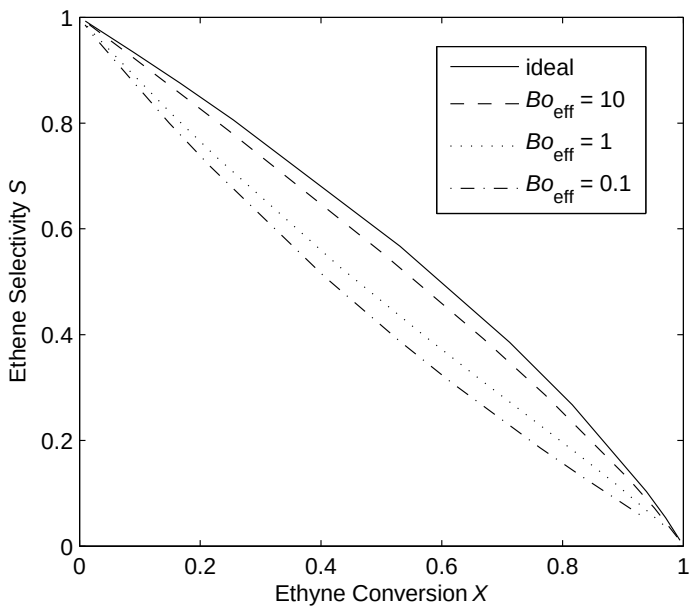

(b) Reactor temperature $T_{\mathrm{r}} = 500\,\mathrm{K}$, varying Bo_{eff}

Figure 5.8: Selectivity S as a function of conversion X for model kinetics and excess hydrogen ($e = 1$)

high values of $Bo_{\text{eff}} \geq 50$, a difference from the ideal PFTR behavior can hardly be quantified, but for the presented case of $Bo_{\text{eff}} = 10$, the selectivity loss at an intermediate conversion of $X = 0.5$ already amounts up to four percentage points. For strong dispersion ($Bo_{\text{eff}} = 0.1$) the selectivity at a high conversion of $X = 0.9$ is even reduced by more than 50 % compared to the ideal reactor. The figure does not show explicitly that for strong dispersion, comparable to reduced temperature, the required mean residence time to achieve a desired conversion is much higher than in case of the ideal reactor. A comparison of Figure 5.8(a) and Figure 5.8(b) shows that the influence of the residence time distribution on reaction selectivity is comparable to a change of the reaction temperature.

5.3.3 Experimental Validation

Experimentally, Bo_{eff} can most easily be varied by altering the reactor pressure or the flow-through velocity. Increasing the flow-through velocity reduces axial dispersion, but the resulting selectivities are difficult to compare due to different mean residence times and consequently different conversions. Increasing the absolute pressure while keeping the partial pressures constant by diluting with inert nitrogen has the advantage that equal residence times and equal kinetics can be achieved for different values of Bo_{eff}. Kölbl et al. (2004) argue in a similar way that variation of the absolute pressure is more suitable to check for mass transfer limitations in microstructured reactors than variation of the fluid velocity. Nevertheless, if the same feed temperatures are applied, the reactor temperatures decrease with increasing dilution. So in order to achieve equal reactor temperatures as well, the feed temperature has to be adjusted.

Ethyne hydrogenation experiments are performed applying constant partial pressures of the reactants as well as constant mean residence times and permeate temperatures in each set of experiments, varying only the absolute pressure by diluting with nitrogen. The resulting conversions and selectivities are displayed as a function of the mean reactor pressure in Figure 5.9. In spite of constant partial pressures and residence times, both conversion and

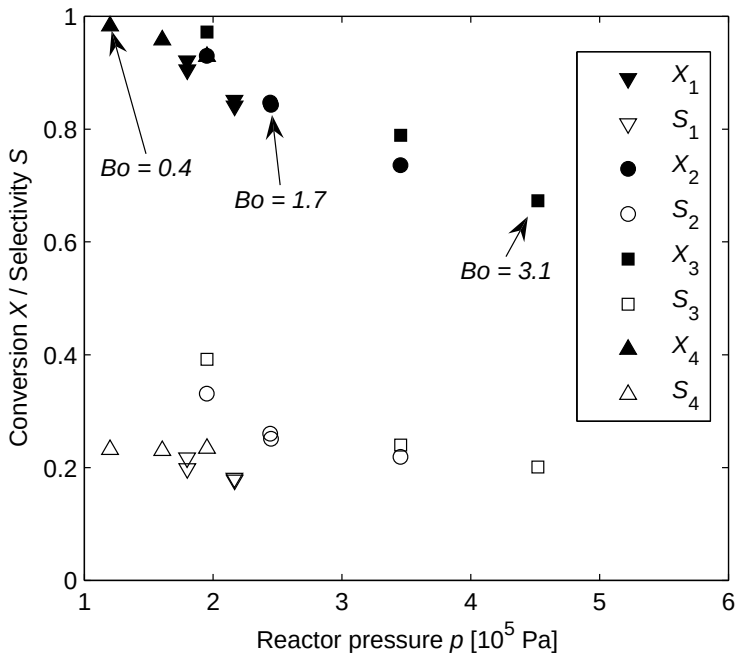

Figure 5.9: Measured conversions and selectivities for constant partial pressures of $p_{C_2H_2} = 0.1 \cdot 10^5$ Pa and $p_{H_2} = 0.8 \cdot 10^5$ Pa, rest N_2
Subscript 1 (triangles, down): $T = 460$ K, $\tau = 0.31$ ms
Subscript 2 (circles): $T = 440$ K, $\tau = 0.32$ ms
Subscript 3 (squares): $T = 430$ K, $\tau = 0.33$ ms
Subscript 4 (triangles, up): $T = 440$ K, $\tau = 0.64$ ms

selectivity strongly decrease with increasing nitrogen dilution, which corresponds to increasing values of Bo_{eff}. This behavior could be explained by assuming a role of nitrogen in the reaction kinetics. Nitrogen seems to compete with the reactants for adsorption sites at the catalyst and thus reduces the overall reaction rate. The simultaneous decrease of selectivity indicates that this site competition is more pronounced for the partial hydrogenation than for the consecutive hydrogenation. As no site competition with nitrogen has been reported for Pd-catalyzed hydrogenation reactions, small traces of CO in the nitrogen 5.0 gas cylinder could also cause the decrease of reaction kinetics at higher nitrogen dilution (Bos and Westerterp, 1993). The observed kinetic phenomenon interferes with the influence of axial dispersion and prevents the determination of effective dispersion coefficients.

5.4 Impact of Catalytic Microstructure

Catalytic activity experiments performed in anodized and sintered catalytic membranes have already been presented in Subsection 3.3.4 with the aim of characterizing catalyst amount. Although the amount of catalyst in the sintered membranes determined by UV-vis or ICP exceeds the one in the anodized membranes by a factor of at least five due to the increased membrane thickness, and although the mean residence time in the sintered membranes is one order of magnitude higher, the observed conversions are comparable, suggesting more efficient use of catalyst in the anodized membranes due to intensive contact in the microchannels.

Ethyne hydrogenation experiments are performed in four different reactor types to identify the impact of reactor microstructure on conversion and selectivity. The performance of the membrane microchannel reactor (W02 MR) is compared to that of a randomly structured sintered membrane reactor (K02 MR) and to equivalent fixed beds of ground catalytic membranes (W02 FBR, K02 FBR). For the applied sintered membrane (K02-4-10) a catalyst mass of 2 mg Pd is determined by means of UV-vis, whereas the applied anodized membranes (W02-4-10) are loaded with 0.3 mg Pd. After initial membrane reactor experiments, the same catalytic membranes are finely ground and reintroduced into the reactor module in shape of a fixed bed of catalytic particles. To prevent loss of catalyst, the powder is placed between two non-catalytic membranes and surrounded by an aluminium ring with internal diameter of 20 mm.

Due to the different geometries, resulting in different pressure drop and heat transfer, equivalent operating conditions are hard to establish. All experiments are performed applying a reactant ratio of $C_2H_2 : H_2 : N_2 = 1 : 9 : 19$ at a product temperature of $T = 443\,\mathrm{K}$, varying reactor pressure and flow rate. The experimental results are displayed in Figure 5.10.

Due to the large amount of catalyst in combination with intensive reactant contact, full conversion to ethane is obtained in the sintered membrane reactor even at the highest applied flow rate (Figure 5.10(a)). Due to the high membrane thickness of 2 mm, pressure drop is considerable compared

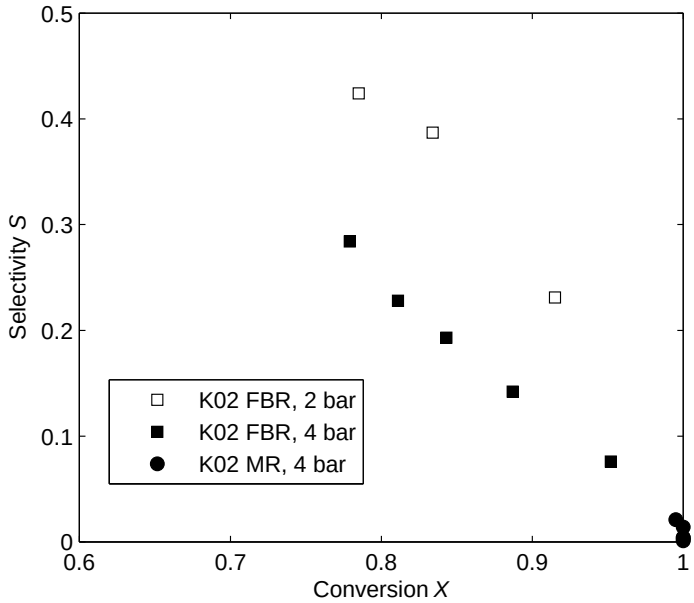

(a) Sintered K02-4-10 membrane, 2 mg Pd

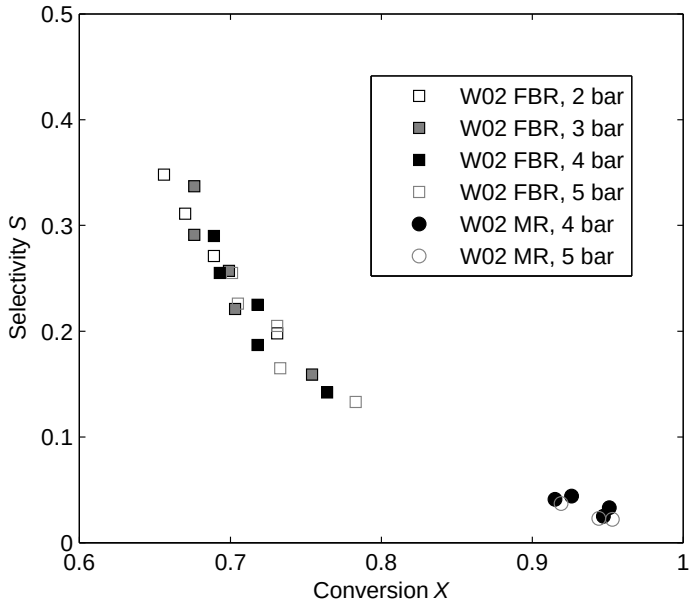

(b) Anodized W02-4-10 membrane, 0.3 mg Pd

Figure 5.10: Comparison of catalytic membrane reactor (MR) and fixed bed reactor (FBR) performance for sintered K02 membrane and for anodized W02 membrane at $T = 443\,\mathrm{K}$, $p = 2 - 5\,\mathrm{bar}$ and reactant ratio $C_2H_2 : H_2 : N_2 = 1 : 9 : 19$

to the thin anodized membranes. In fixed bed mode, ethyne conversion as well as pressure drop are significantly reduced. The conversion decreases for reduced residence times, accompanied by an increase of selectivity.

The anodized catalytic membrane reactor mode also reaches high conversions $X > 90\,\%$ and accordingly low selectivities towards ethene (Figure 5.10(b)). In fixed bed mode conversions are reduced significantly. On the other hand, selectivities increase in the FBR compared to the MR, as could be expected from the reduced conversions. All measured selectivities lie on the same trajectory if compared to the corresponding conversions, not allowing to quantify a microstructure impact on selectivity.

For both membrane types, the intensive contact in the membrane reactor mode leads to higher catalytic activity compared to the catalytic fixed beds with equivalent amount of catalyst. A comparison between the four reactor setups shows that the obtained selectivity for a certain conversion is higher in the fixed bed of sintered K02 membranes than in the reactors with anodized W02 membranes, while the conversion in the K02 membrane reactor is too high and consequently the selectivities are too low for a comparison. This result cannot be explained with the microstructure influence, in fact it demonstrates that all four reactor setups are operated in a regime where axial dispersion rather than microstructure or pore size distribution limits the reactor performance. To prevent decomposition of ethyne, the anodized membrane reactor has to be operated below the optimum pressure regime, allowing for maximum values of $Bo = 6$. The Bodenstein number is proportional to axial velocity and reactor length. The increased thickness of the K02 membrane leads to increased values of Bo_{eff} compared to the W02 membrane. Further, the reactor diameter of the applied fixed beds is lower than the open membrane diameter, leading to higher axial velocities, while the bed height is significantly higher than the membrane thickness. Both effects lead to an increased value of Bo_{eff} for the fixed bed compared to the membrane reactor. Thus, if the membrane reactor is not operated in a regime where it can be considered ideal, reduced axial dispersion in a fixed bed overcompensates the effect of regular microstructure, allowing for higher selectivities.

In all reactor types, catalyst deactivation can be observed. For exam-

ple with the W02 fixed bed, the initial experiments are repeated after two hours of operation, producing comparable selectivities at reduced conversions (at $p = 5\,\text{bar}$ decrease from initially $X = 70\,\%$ to finally $X = 62\,\%$ while selectivity stays constant at $S = 25\,\%$). Simultaneously, a slight decrease of pressure drop can be observed. Especially the thin anodized membranes are difficult to handle. Breakage can be observed by a simultaneous decrease of pressure drop, conversion and selectivity. After use, most of the catalytic membranes are destroyed during disassembly, if not already during the reaction experiments. These constraints impede the determination of reproducible experimental results and certainly need to be eliminated before moving forward to industrial applications of the reactor concept.

The performed experiments prove the high catalytic activity of flow-through membrane reactors compared to fixed bed reactors with the same amount of catalyst, whereas improved selectivity can only be achieved in a small window of operating conditions.

5.5 Conclusions

The kinetics of ethene hydrogenation as well as partial ethyne hydrogenation reactions are determined experimentally, assuming ideal plug flow behavior, by fitting the parameters of power law approaches to the measured conversions and selectivities. For ethene hydrogenation a reaction order of $n = 1.8$ with low temperature dependence is identified. Ethyne hydrogenation with large excess of hydrogen and nitrogen dilution is best represented by a total reaction order of $n = 0.7$. While the influence of temperature is limited, both increasing absolute pressure and increasing hydrogen partial pressure promote the subsequent hydrogenation to ethane, reducing selectivity.

A heat transfer model of the catalytic membrane reactor is derived, accounting for heat convection, heat conduction in gas and wall as well as heat transfer inside the catalytic membrane and between membrane and reactor module. All parameters are grouped into four dimensionless quantities Nu, Pe, Bi and Bi_0. If the ratio between Nu and Pe, which can be called internal Stanton number St, becomes larger than 1000, the temperature profiles

of gas phase and membrane wall coincide and the reactor can be regarded isothermal. The gas temperature immediately jumps from the lower feed temperature to the constant reactor temperature when entering the catalytic membrane pore. Due to the small reactor dimensions, in the anodized membrane reactor this requirement is fulfilled under any operating conditions. In this case, the heat transfer mechanisms inside the membrane prove to be irrelevant for the resulting membrane temperature, which is exclusively determined by a further dimensionless quantity, the external Stanton number St_0. This parameter results as a combination of the four initial dimensionless numbers and is proportional to the heat transfer coefficient between membrane and reactor module divided by the total flow rate.

Performed ethene hydrogenation experiments suggest that St_0 is nearly constant in the applied range of operating conditions. This implies that for increasing flow rate, the heat transfer coefficient increases proportionally. With this constant parameter characterizing the heat removal ratio from the reactor, the resulting reactor temperature can be predicted satisfactorily in the whole range of performed experiments.

Due to a potentially narrow residence time distribution, the flow-through catalytic membrane reactor is suitable for performing selective reactions. An isothermal reactor model for a multi-component reactant mixture and multiple reactions accounts for the residence time distribution caused by axial dispersion and the pore size distribution of the membrane by means of the effective Bodenstein number Bo_{eff}, derived in Chapter 4. The achievable selectivity for a desired conversion depends on reactor temperature and on Bo_{eff}. Reactor temperature directly influences reaction kinetics, either promoting the desired or the undesired reaction. For a specific temperature, low values of Bo_{eff} can additionally reduce the achievable selectivity significantly. Due to a presumed influence of nitrogen in the respective reaction rates, the performed selective ethyne hydrogenation experiments at different absolute pressures cannot be used to determine effective dispersion coefficients and to validate the reactor model. Nevertheless, simulation results suggest that for $Bo_{\text{eff}} > 20$ the difference between achieved selectivity and potential selectivity in an ideal PFTR is negligible.

The performance of the flow-through catalytic membrane reactor can successfully be predicted by means of the derived reactor models if appropriate reaction kinetics are available. The isothermal operation even of highly exothermic reactions is beneficial for kinetic studies. If operated in a low-dispersion regime by providing sufficient absolute pressure and flow-through velocity, the reactor behavior can be regarded ideal, signifying that the achievable selectivities are only limited kinetically.

A comparison between the reactor performance of anodized membranes with regular microchannels and catalytic sintered membranes suggests a more efficient use of catalyst in the anodized membranes, which possess smaller pore diameters. Regarding selectivity, the performed ethyne hydrogenation experiments cannot prove superiority of anodized membrane reactors compared to sintered membrane reactors or even to fixed beds of ground catalytic membranes. This can be attributed to a limitation of the operating pressure induced by the application of ethyne. To prevent decomposition, the reactor is operated below the pressure regime identified as ideal, allowing for maximum values of $Bo = 6$ for the anodized membrane reactor. As in this regime the microstructure impact is small, the increased reactor length of the sintered membrane and of the fixed bed can even lead to reduced effective dispersion compared to the anodized membrane, which can be measured in terms of higher selectivities.

Chapter 6

Conclusions

Flow-through membrane reactors represent a promising approach to intensify heterogeneous catalysis in both gas and liquid phase. Considering their function, the term microreactor applies better (in case of anodized alumina membranes also micro monolithic reactor), as no separative function is performed. The concept promises high catalytic activity and very short contact times combined with a narrow residence time distribution. In contrast to other reactor types, the performance of flow-through membrane reactors regarding diffusion limitation even improves for higher flow-through velocities. Compared to fixed bed reactors, mass and heat transfer limitations can effectively be avoided, the pressure drop reduced and the specific surface area increased. The drawbacks of moving bed or slurry reactors, such as catalyst attrition, equipment erosion and catalyst separation do not apply either.

The choice of the appropriate pore size for a catalytic membrane reactor always represents a trade-off between intensive contact and low pressure drop. Comparing published investigations, the mean pore size of the applied membranes varies by several orders of magnitude. The anodic alumina membranes applied in the work at hand are made up of uniform cylindrical channels with a mean pore size around 0.2 µm and narrow pore size distribution. Applied sintered alumina membranes on the other hand show a non-uniform structure with remarkable tortuosity.

Palladium as hydrogenation catalyst is deposited in the membrane pores

by a wet impregnation method applying $Pd(acac)_2$ solved in toluene. The obtained catalyst loading is a function of the concentration of the precursor solution, rather than the impregnation time. The catalytic activity of the membranes increases with the catalyst loading, whereas the porosity decreases. The resulting lower hydrodynamic residence times may lead to decreased conversions compared to moderate catalyst loading, if the catalytically active surface does not grow proportionally, for example due to formation of larger catalyst particles.

For the investigated reactor concept, direct measurement of the residence time distribution is hardly possible. A fluid dynamic reactor model taking into account pore size distribution and axial dispersion allows to quantify deviations from ideal PFTR behavior. Both influences can be combined into an effective dispersion model with the single parameter Bo_{eff}, which can be calculated for known membrane geometry and operating conditions. For strong dispersion caused by low axial velocities and absolute pressures, the influence of the pore size distribution is negligible. Increasing velocity and/or pressure reduces axial dispersion, producing a narrower RTD. At the same time the influence of the pore size distribution grows, limiting the minimum achievable effective dispersion. For the anodic alumina membranes a limit of $Bo_{\mathrm{max}} = 58$ is determined. Flowing through several membranes in sequence additionally reduces the width of the RTD at the cost of increased pressure drop.

For gas phase reactions in pore structures below the micrometer scale the flow processes and microeffects in Knudsen and transition regime can severely influence the reactor behavior. Especially at low absolute pressures a correction factor is required to quantify the reduced pressure drop compared to continuum theory. Axial dispersion is also influenced by rarefaction for gas flows at pressures below 10^6 Pa. Although the effect is generally positive, it cannot compensate for the high diffusivity present at low pressures. For optimum reactor performance, increased pressures are recommended, in which case microeffects are rather insignificant. The same applies for liquid phase reactions.

Reaction experiments are performed, applying ethene hydrogenation as

model reaction for catalytic activity and heat transfer and partial ethyne hydrogenation for selectivity measurements. A heat transfer model reveals that due to the small characteristic lengths heat convection is always small compared to the internal heat transfer ($\mathit{St} \geq 1000$), leading to an isothermal reactor behavior with identical gas phase and membrane temperature. When entering the catalytic membrane pore, the reactants are immediately heated from feed temperature to a constant reactor temperature. Consequently, heat transfer mechanisms inside the membrane are irrelevant for the resulting membrane temperature, which is exclusively determined by the external Stanton number St_0. This dimensionless quantity characterizes the heat removal ratio from the reactor. For the performed ethene hydrogenation experiments in the anodized catalytic membrane reactor setup a constant value of $\mathit{St}_0 = 4.3$ leads to a good agreement with the observed reactor temperatures, independent from the operating conditions. The parameter allows for satisfactory prediction of the resulting reactor temperature in the whole range of performed experiments.

The potentially narrow residence time distribution makes the catalytic membrane reactor in flow-through mode suitable for performing selective reactions. Inversely, high selectivities are an indirect proof for the predicted narrow residence time distribution. Completely comparable reaction conditions, varying only $\mathit{Bo}_{\mathrm{eff}}$, are difficult to create. Thus, the experimental analysis is supported by an isothermal dispersion model. The achievable selectivity for a desired conversion is a function of reactor temperature and $\mathit{Bo}_{\mathrm{eff}}$. The temperature directly influences reaction kinetics, either promoting the desired or the undesired reaction. For a specific temperature, low values of $\mathit{Bo}_{\mathrm{eff}}$ can additionally reduce the achievable selectivity significantly. For values of $\mathit{Bo}_{\mathrm{eff}} > 20$ the difference between achieved selectivity and potential selectivity in an ideal PFTR becomes negligible.

The predicted high catalytic activity of the investigated catalytic membrane microchannel reactor compared to catalytic fixed beds can be proven experimentally. Experimental evidence for the supposed narrow residence time distribution on the other hand is impeded by several factors. The selected model reaction is not suitable for performing experiments at high

pressures due to danger of spontaneous decomposition of ethyne. At realized pressures of up to $6 \cdot 10^5$ Pa, maximum Bodenstein numbers of $Bo \approx 6$ are achieved in the anodized membrane reactor. In this regime, the impact of axial molecular diffusion is more pronounced than the influence of regular microstructure. Even though the flat and thin geometry of membranes is advantageous in terms of high throughput at minimum contact time, it is unfavorable regarding axial dispersion. This prevents application in consecutive low pressure gas phase reactions, where a fixed bed reactor might reach higher selectivities due to increased reactor length.

The isothermal operation even of highly exothermic reactions is beneficial for kinetic studies. If operated in a low-dispersion regime by providing sufficient absolute pressure and flow-through velocity, the reactor behavior can be regarded ideal, which means that only reaction kinetics limit the achievable selectivities. Potential applications of flow-through catalytic membrane reactors are fast gas phase reactions at high pressures and potentially high temperatures, which call for short contact times. Compared to a gas at ambient pressure, the molecular diffusion coefficient in liquids is about four orders of magnitude lower, allowing for high values of Bo even for very low flow-through velocities, which cause maintainable pressure drop. Radial diffusion on the other hand is reduced, but due to the small pore diameters not to an amount that would cause significant deviation from plug-flow behavior.

An interesting parameter for tailoring catalytic membranes to their application is the pore geometry. A small pore size promotes intensive contact between reactants and catalyst, but may generate significant pressure drop. An optimum pore size might be determined for specific applications, which causes the lowest flow resistance but is still not limited by heat and mass transfer resistances. In many cases a sintered membrane might be the more economic choice, but the advantages of anodized membranes, such as low tortuosity, narrow pore size distribution and very low thickness, should be considered carefully. Their thin symmetric structure also allows for complete catalytic coating without need to limit the catalytic region to a certain layer, as would be favorable in asymmetric membranes. A more detailed examination of the pore structure influence on the reactor performance promises

to be an interesting topic for future investigations. For a significant comparison between a regularly structured catalytic membrane reactor and an equivalent unstructured or fixed bed reactor a thorough design of the reactor setup is essential. The extremely short reactor length of the catalytic membrane can hardly be realized with a fixed bed without causing by-pass flows. Increased reactor length on the other hand reduces axial dispersion. A reactor concept consisting of several catalytic layers interrupted by non-catalytic regions might be realized with both reactor types, allowing for comparable reactor length, fluid dynamics and catalyst loading.

Other potential research topics could result in further improvement of the reactor concept: In the applied reactor module, part of the catalytic membrane is not accessible from the feed side due to the graphite gasket, which is essential to prevent by-pass flows. Nevertheless, from the permeate side, these region can be accessed by radial diffusion in the porous support, allowing for undesired sequential reactions and increasing the width of the actual residence time distribution. This contact could be prevented by sealing either the inaccessible pores of the membrane or the corresponding region of the porous support for example by gluing. Finally, the distribution of the incoming flow along the membrane surface might cause radial depletion of reactants due to reaction and back-diffusion, which can be especially unfavorable in case of competing reactions. A non-catalytic layer acting as diffusion barrier could improve the performance, if this depletion turns out to be significant.

Bibliography

R. Adler. Stand der Simulation von heterogen-gaskatalytischen Reaktionsabläufen in Festbettrohrreaktoren - Teil 1. *Chemie Ingenieur Technik*, 72 (6):555–564, 2000.

S. K. Ajmera, C. Delattre, M. A. Schmidt, and K. F. Jensen. Microfabricated differential reactor for heterogeneous gas phase catalyst testing. *Journal of Catalysis*, 209(2):401–412, July 2002. DOI: 10.1006/jcat.2002.3584.

S. E. Albo, L. J. Broadbelt, and R. Q. Snurr. Multiscale modeling of transport and residence times in nanostructured membranes. *AIChE Journal*, 52(11): 3679–3687, 2006. DOI: 10.1002/aic.10998.

S. E. Albo, L. J. Broadbelt, and R. Q. Snurr. Transmission probabilities and particle-wall contact for Knudsen diffusion in pores of variable diameter. *Chemical Engineering Science*, 62(23):6843–6850, Dec. 2007. DOI: 10.1016/j.ces.2007.08.041.

M. Alfonso, M. Menendez, and J. Santamaria. Coupling of consecutive reactions in a two-layer, flow-through catalytic membrane. *Industrial & Engineering Chemistry Research*, 40(4):1058–1064, 2001. DOI: 10.1021/ie000643n.

J. N. Armor. Membrane catalysis: Where is it now, what needs to be done? *Catalysis Today*, 25(3-4):199–207, Aug. 1995. DOI: 10.1016/0920-5861(95)00073-O.

M. Baerns, H. Hofmann, and A. Renken. *Chemische Reaktionstechnik*, volume 1 of *Lehrbuch der Technischen Chemie*. Wiley-VCH, Stuttgart, 3 edition, 1999. ISBN 978-3-527-30841-5.

S.-Y. Bai, Z.-A. Tang, Z.-X. Huang, J. Yu, and J.-Q. Wang. Thermal conductivity measurement of submicron-thick aluminium oxide thin films by a transient thermo-reflectance technique. *Chinese Physics Letters*, 25(2): 593–596, 2008. DOI: 10.1088/0256-307X/25/2/065.

T. Bayer, M. Matlosz, and J. Jenck. IMPULSE - Ein neuartiger Ansatz für die Prozessentwicklung. *Chemie Ingenieur Technik*, 76(5):528–533, 2004. DOI: 10.1002/cite.200403397.

G. Bengough and H. Sutton. The protection of aluminum and its alloys against corrosion by anodic oxidation. *Engineering: An Illustrated Weekly Journal*, 122:274–277, 1926.

R. R. Bhave. *Inorganic membranes: Synthesis, characteristics, and applications*. Van Nostrand Reinhold New York, 1991. ISBN 978-0-442-31876-6.

R. B. Bird, W. E. Stewart, and E. N. Lightfoot. *Transport Phenomena*. Wiley & Sons, 2 edition, 2001. ISBN 978-0-470-11539-8.

J. P. Boitiaux, J. Cosyns, and S. Vasudevan. Preparation and characterisation of highly dispersed palladium catalysts on low surface alumina. Their notable effects in hydrogenation. In G. Poncelet, P. Grange, and P. A. Jacobs, editors, *Preparation of Catalysts III, Scientific Bases for the Preparation of Heterogeneous Catalysts. Proceedings of the Third International Symposium, Louvain-la-Neuve, September 6-9, 1982.*, number 16 in Studies in Surface Science and Catalysis, pages 123–134. Elsevier, 1983. ISBN 978-0-444-42184-5.

A. Borodzinski. Hydrogenation of acetylene-ethylene mixtures on a commercial palladium catalyst. *Catalysis Letters*, 63(1):35–42, Nov. 1999. DOI: 10.1023/A:1019052618049.

A. N. R. Bos and K. R. Westerterp. Mechanism and kinetics of the selective hydrogenation of ethyne and ethene. *Chemical Engineering and Processing*, 32(1):1–7, Feb. 1993. DOI: 10.1016/0255-2701(93)87001-B.

A. N. R. Bos, E. S. Botsma, F. Foeth, H. W. J. Sleyster, and K. R. Westerterp. A kinetic study of the hydrogenation of ethyne and ethene on a commercial Pd/Al2O3 catalyst. *Chemical Engineering and Processing*, 32 (1):53–63, Feb. 1993. DOI: 10.1016/0255-2701(93)87006-G.

J. Bravo, A. Karim, T. Conant, G. P. Lopez, and A. Datye. Wall coating of a CuO/ZnO/Al2O3 methanol steam reforming catalyst for micro-channel reformers. *Chemical Engineering Journal*, 101(1-3):113–121, Aug. 2004. DOI: 10.1016/j.cej.2004.01.011.

S. Brunauer, P. H. Emmett, and E. Teller. Adsorption of gases in multimolecular layers. *Journal of the American Chemical Society*, 60(2):309–319, 1938. DOI: 10.1021/ja01269a023.

J. Caro, K. Caspary, C. Hamel, B. Hoting, P. Kölsch, B. Langanke, K. Nassauer, T. Schiestel, A. Schmidt, R. Schomäcker, A. Seidel-Morgenstern, E. Tsotsas, I. Voigt, H. Wang, R. Warsitz, S. Werth, and A. Wolf. Catalytic membrane reactors for partial oxidation using perovskite hollow fiber membranes and for partial hydrogenation using a catalytic membrane contactor. *Industrial & Engineering Chemistry Research*, 46(8):2286–2294, 2007. DOI: 10.1021/ie0609620.

J. Coronas and J. Santamaria. Catalytic reactors based on porous ceramic membranes. *Catalysis Today*, 51(3-4):377–389, July 1999. DOI: 10.1016/S0920-5861(99)00090-5.

P. V. Danckwerts. Continuous flow systems: Distribution of residence times. *Chemical Engineering Science*, 2(1):1–13, Feb. 1953. DOI: 10.1016/0009-2509(53)80001-1.

DECHEMA. Geschäftsordnung der Fachsektion Prozessintensivierung, Aug. 2006.

R. Dittmeyer, V. Höllein, and K. Daub. Membrane reactors for hydrogenation and dehydrogenation processes based on supported palladium. *Journal of Molecular Catalysis A: Chemical*, 173(1-2):135–184, Sept. 2001. DOI: 10.1016/S1381-1169(01)00149-2.

R. Dittmeyer, K. Svajda, and M. Reif. A review of catalytic membrane layers for gas/liquid reactions. *Topics in Catalysis*, 29(1):3–27, May 2004. DOI: 10.1023/B:TOCA.0000024925.30020.a1.

A. G. Dixon. Innovations in catalytic inorganic membrane reactors. In J. J. Spivey, editor, *Catalysis*, volume 14 of *Specialist Periodical Reports*, chapter 2, pages 40–92. RSC Publishing, 1999. ISBN 978-1-84755-326-3. DOI: 10.1039/9781847553263.

A. G. Dixon. Recent research in catalytic inorganic membrane reactors. *International Journal of Chemical Reactor Engineering*, 1(R6):1–35, 2003. URL `http://www.bepress.com/ijcre/vol1/R6`.

W. Ehrfeld, V. Hessel, and H. Löwe. *Microreactors - New technology for modern chemistry*. Wiley-VCH, Weinheim, 2000. ISBN 978-3-527-29590-6.

R. Espinoza, E. du Toit, J. Santamaria, M. Menendez, J. Coronas, and S. Irusta. Use of membranes in Fischer-Tropsch reactors. In S. M.

Avelino Corma, Francisco V. Melo and J. L. G. Fierro, editors, *12th International Congress on Catalysis, Proceedings of the 12th ICC*, volume Volume 130, Part 1, pages 389–394. Elsevier, 2000. DOI: 10.1016/S0167-2991(00)80988-X.

D. Fritsch and G. Bengtson. Catalytic polymer membranes for high temperature hydrogenation of viscous liquids. *Advanced Engineering Materials*, 8 (5):386–389, 2006a. DOI: 10.1002/adem.200600019.

D. Fritsch and G. Bengtson. Development of catalytically reactive porous membranes for the selective hydrogenation of sunflower oil. *Catalysis Today*, 118(1-2):121–127, Oct. 2006b. DOI: 10.1016/j.cattod.2006.01.039.

D. Fritsch, I. Randjelovic, and F. Keil. Application of a forced-flow catalytic membrane reactor for the dimerisation of isobutene. *Catalysis Today*, 98 (1-2):295–308, Nov. 2004. DOI: 10.1016/j.cattod.2004.07.043.

L. Giorno and E. Drioli. Biocatalytic membrane reactors: Applications and perspectives. *Trends in Biotechnology*, 18(8):339–349, Aug. 2000. DOI: 10.1016/S0167-7799(00)01472-4.

V. Gnielinski. *VDI-Wärmeatlas*, chapter Wärmeübertragung bei der Strömung durch Rohre, page Ga 3.1.1. Springer-Verlag Berlin Heidelberg, 2006. ISBN 978-3-540-29646-1.

J. Goetz, M. A. Volpe, A. M. Sica, C. E. Gigola, and R. Touroude. Low-loaded palladium on [alpha]-alumina catalysts: Characterization by chemisorption, electron-microscopy, and photoelectron spectroscopy. *Journal of Catalysis*, 153(1):86–93, Apr. 1995. DOI: 10.1006/jcat.1995.1110.

S. V. Gokhale, R. K. Tayal, V. K. Jayaraman, and B. D. Kulkarni. Microchannel reactors: Applications and use in process development. *International Journal of Chemical Reactor Engineering*, 3(R2):1–51, 2005. URL `http://www.bepress.com/ijcre/vol3/R2`.

L. Gröschel, R. Haidar, A. Beyer, H. Colfen, B. Frank, and R. Schomäcker. Hydrogenation of propyne in palladium-containing polyacrylic acid membranes and its characterization. *Industrial & Engineering Chemistry Research*, 44(24):9064–9070, 2005. DOI: 10.1021/ie050426s.

V. Gryaznov and N. Orekhova. Reactors with metal and metal-containing membranes. In A. Cybulski and J. A. Moulijn, editors, *Structured Catalysts and Reactors*, chapter 16, pages 435–462. Marcel Dekker Ltd, 1998. ISBN 978-0-82472-343-9.

D. A. Hickman and L. D. Schmidt. Production of syngas by direct catalytic oxidation of methane. *Science*, 259(5093):343–346, Jan. 1993. DOI: 10.1126/science.259.5093.343.

M. Huff and L. D. Schmidt. Ethylene formation by oxidative dehydrogenation of ethane over monoliths at very short contact times. *Journal of Physical Chemistry*, 97(45):11815–11822, 1993. DOI: 10.1021/j100147a040.

O. M. Ilinich, E. N. Gribov, and P. A. Simonov. Water denitrification over catalytic membranes: Hydrogen spillover and catalytic activity of macroporous membranes loaded with Pd and Cu. *Catalysis Today*, 82(1-4):49–56, July 2003. DOI: 10.1016/S0920-5861(03)00201-3.

O. M. Ilinitch, F. P. Cuperus, L. V. Nosova, and E. N. Gribov. Catalytic membrane in reduction of aqueous nitrates: Operational principles and catalytic performance. *Catalysis Today*, 56(1-3):137–145, Feb. 2000. DOI: 10.1016/S0920-5861(99)00270-9.

O. Jessensky, F. Müller, and U. Gosele. Self-organized formation of hexagonal pore arrays in anodic alumina. *Applied Physics Letters*, 72(10):1173–1175, Mar. 1998. DOI: 10.1063/1.121004.

K. Jähnisch, V. Hessel, H. Löwe, and M. Baerns. Chemistry in microstructured reactors. *Angewandte Chemie, International Edition*, 43(4):406–446, 2004. DOI: 10.1002/anie.200300577.

A. Julbe, D. Farrusseng, and C. Guizard. Porous ceramic membranes for catalytic reactors - Overview and new ideas. *Journal of Membrane Science*, 181(1):3–20, Jan. 2001. DOI: 10.1016/S0376-7388(00)00375-6.

A. Karim, J. Bravo, D. Gorm, T. Conant, and A. Datye. Comparison of wall-coated and packed-bed reactors for steam reforming of methanol. *Catalysis Today*, 110(1-2):86–91, Dec. 2005. DOI: 10.1016/j.cattod.2005.09.010.

G. Karniadakis, A. Beskok, and N. Aluru. *Microflows and nanoflows - Fundamentals and simulation*. Number 29 in Interdisciplinary Applied Mathematics. Springer, New York, 2005. ISBN 978-0-387-22197-7.

R. Kato, A. Maesono, and R. P. Tye. Thermal conductivity measurement of submicron-thick films deposited on substrates by modified ac calorimetry (laser-heating Ångstrom method). *International Journal of Thermophysics*, 22(2):617–629, Mar. 2001. DOI: 10.1023/A:1010745603645.

F. Keller, M. S. Hunter, and D. L. Robinson. Structural features of oxide coatings on aluminum. *Journal of the Electrochemical Society*, 100(9):411–419, Sept. 1953. DOI: 10.1149/1.2781142.

A. Khassin, A. Sipatrov, T. Yurieva, G. Chermashentseva, N. Rudina, and V. Parmon. Performance of a catalytic membrane reactor for the Fischer-Tropsch synthesis. *Catalysis Today*, 105(3-4):362–366, Aug. 2005a. DOI: 10.1016/j.cattod.2005.06.031.

A. A. Khassin. Catalytic membrane reactor for conversion of syngas to liquid hydrocarbons. *Energeia*, 16(6):1–3, July 2005.

A. A. Khassin, A. G. Sipatrov, G. K. Chermashetseva, T. M. Yurieva, and V. N. Parmon. Fischer-Tropsch synthesis using plug-through contactor membranes based on permeable composite monoliths. Selectivity control by porous structure parameters and membrane geometry. *Topics in Catalysis*, 32(1):39–46, Feb. 2005b. DOI: 10.1007/s11244-005-9258-z.

A. Kölbl, P. Pfeifer, M. Fichtner, M. Kraut, K. Schubert, M. Liauw, and G. Emig. Examination of external mass transport in a microchannel reactor by pressure variation. *Chemical Engineering & Technology*, 27(6): 671–675, 2004. DOI: 10.1002/ceat.200401962.

C. Knösche. Wärmeabfuhr und Rückvermischung in mikrostrukturierten Apparaten. *Chemie Ingenieur Technik*, 77(11):1715–1722, 2005. DOI: 10.1002/cite.200500123.

M. Kobayashi, J. Togawa, T. Kanno, J.-i. Horiuchi, and K. Tada. Dramatic innovation of propene epoxidation efficiency derived from a forced flow membrane reactor. *Journal of Chemical Technology and Biotechnology*, 78 (2-3):303–307, 2003. DOI: 10.1002/jctb.775.

W. Koros, Y. Ma, and T. Shimidzu. Terminology for membranes and membrane processes (IUPAC Recommendations 1996). *Journal of Membrane Science*, 120:149–159(11), Nov. 1996. DOI: 10.1016/0376-7388(96)82861-4.

U. Kragl and T. Dwars. The development of new methods for the recycling of chiral catalysts. *Trends in Biotechnology*, 19(11):442–449, Nov. 2001. DOI: 10.1016/S0167-7799(01)01766-8.

M. Kreutzer, J. Bakker, F. Kapteijn, J. Moulijn, and P. Verheijen. Scaling-up multiphase monolith reactors: Linking residence time distribution and feed maldistribution. *Industrial & Engineering Chemistry Research*, 44 (14):4898–4913, July 2005. DOI: 10.1021/ie0492350.

C. Lambert and R. Gonzalez. Activity and selectivity of a Pd/gamma-Al2O3 catalytic membrane in the partial hydrogenation reactions of acetylene and 1,3-butadiene. *Catalysis Letters*, 57(1):1–7, Feb. 1999. DOI: 10.1023/A:1019027027792.

C. Lange, S. Storck, B. Tesche, and W. F. Maier. Selective hydrogenation reactions with a microporous membrane catalyst, prepared by sol-gel dip coating. *Journal of Catalysis*, 175(2):280–293, Apr. 1998. DOI: 10.1006/jcat.1998.1994.

K. Lüdtke, K.-V. Peinemann, V. Kasche, and R.-D. Behling. Nitrate removal of drinking water by means of catalytically active membranes. *Journal of Membrane Science*, 151(1):3–11, Dec. 1998. DOI: 10.1016/S0376-7388(98)00227-0.

S.-Y. Lee and R. Aris. The distribution of active ingredients in supported catalysts prepared by impregnation. *Catal. Rev. - Sci. Eng.*, 27(2):207–340, 1985. DOI: 10.1080/01614948508064737.

A. Lekhal, B. J. Glasser, and J. G. Khinast. Impact of drying on the catalyst profile in supported impregnation catalysts. *Chemical Engineering Science*, 56(15):4473–4487, Aug. 2001. DOI: 10.1016/S0009-2509(01)00120-8.

O. Levenspiel. *Chemical Reaction Engineering*. Wiley & Sons, 3 edition, 1999. ISBN 978-0-471-25424-9.

A. P. Li, F. Müller, A. Birner, K. Nielsch, and U. Gösele. Hexagonal pore arrays with a 50–420 nm interpore distance formed by self-organization in anodic alumina. *Journal of Applied Physics*, 84(11):6023–6026, Dec. 1998. DOI: 10.1063/1.368911.

Y.-S. Lin and A. J. Burggraaf. Preparation and characterization of high-temperature thermally stable alumina composite membrane. *Journal of the American Ceramic Society*, 74(1):219–224, 1991. DOI: 10.1111/j.1151-2916.1991.tb07320.x.

F. Lipnizki, R. W. Field, and P.-K. Ten. Pervaporation-based hybrid process: a review of process design, applications and economics. *Journal of Membrane Science*, 153(2):183–210, Feb. 1999. DOI: 10.1016/S0376-7388(98)00253-1.

Q. Liu, J. Rogut, B. Chen, J. L. Falconer, and R. D. Noble. Improved methanol yield from methane oxidation in a non-isothermal reactor. *Fuel*, 75(15):1748–1754, Nov. 1996. DOI: 10.1016/S0016-2361(96)00112-3.

X. Liu, J. G. Khinast, and B. J. Glasser. A parametric investigation of impregnation and drying of supported catalysts. *Chemical Engineering Science*, 63(18):4517–4530, Sept. 2008. DOI: 10.1016/j.ces.2008.06.013.

Y. Ma, W. Moser, A. Dixon, A. Ramachandra, Y. Lu, and C. Binkerd. Oxidative coupling of methane using inorganic membrane reactors. Technical report, Worcester Polytechnic Institute, Worcester, MA., United States, 1998.

A. J. Maira, W. N. Lau, C. Y. Lee, P. L. Yue, C. K. Chan, and K. L. Yeung. Performance of a membrane-catalyst for photocatalytic oxidation of volatile organic compounds. *Chemical Engineering Science*, 58(3-6): 959–962, 2003. DOI: 10.1016/S0009-2509(02)00634-6.

H. Masuda, H. Yamada, M. Satoh, H. Asoh, M. Nakao, and T. Tamamura. Highly ordered nanochannel-array architecture in anodic alumina. *Applied Physics Letters*, 71(19):2770–2772, Nov. 1997. DOI: 10.1063/1.120128.

T. Melin and R. Rautenbach. *Membranverfahren - Grundlagen der Modul- und Anlagenauslegung*. VDI-Buch Chemische Technik / Verfahrenstechnik. Springer, 3 edition, 2007. ISBN 978-3-540-34327-1.

Merck-Schuchardt. Safety data sheet palladium(II)acetylacetonate for synthesis, 2006.

N. Mostoufi, A. Ghoorchian, and R. Sotudeh-Gharebagh. Hydrogenation of acetylene: Kinetic studies and reactor modeling. *International Journal of Chemical Reactor Engineering*, 3(A14):1–18, 2005. URL `http://www.bepress.com/ijcre/vol3/A14`.

S. Mucherie, H.-S. Kim, C. L. Marshall, J. A. Libera, J. W. Elam, and P. C. Stair. Oxidative dehydrogenation of propane over nanostructured membrane catalyst. In *North American Catalysis Society 20th North American Meeting (20NAM)*, 2007.

R. G. Munro. Evaluated material properties for a sintered [alpha]-alumina. *Journal of the American Ceramic Society*, 80(8):1919–1928, 1997. DOI: 10.1111/j.1151-2916.1997.tb03074.x.

A. V. Neimark, L. I. Kheifets, and V. B. Fenelonov. Theory of preparation of supported catalysts. *Industrial & Engineering Chemistry Product Research and Development*, 20(3):439–450, 1981. DOI: 10.1021/i300003a006.

U. Pallaske. Kritik an zwei bekannten Verweilzeitformeln für das Diffusionsströmungsrohr. *Chemie Ingenieur Technik*, 56(1):46–47, 1984. DOI: 10.1002/cite.330560112.

I. Papautsky, T. Ameel, and A. Frazier. A review of laminar single-phase flow in microchannels. In *Proceedings of ASME International Mechanical Engineering Congress and Exposition (IMECE)*, pages 3067–3075, 2001.

M. A. Peña, D. M. Carr, K. L. Yeung, and A. Varma. Ethylene epoxidation in a catalytic packed-bed membrane reactor. *Chemical Engineering Science*, 53(22):3821–3834, Nov. 1998. DOI: 10.1016/S0009-2509(98)00189-4.

M. Pellin, P. Stair, G. Xiong, J. Elam, J. Birrell, L. Curtiss, S. George, C. Han, L. Iton, H. Kung, M. Kung, and H.-H. Wang. Mesoporous catalytic membranes: Synthetic control of pore size and wall composition. *Catalysis Letters*, 102(3):127–130, Aug. 2005. DOI: 10.1007/s10562-005-5843-9.

R. Peters. *Schaumstrukturanalyse mit digitalen Bildverarbeitungsmethoden.* PhD thesis, RWTH Aachen University, 2004.

M. Pina, M. Menendez, and J. Santamaria. The Knudsen-diffusion catalytic membrane reactor: An efficient contactor for the combustion of volatile organic compounds. *Applied Catalysis, B: Environmental*, 11(1):L19–L27, Dec. 1996. DOI: 10.1016/S0926-3373(96)00081-1.

H. Purnama, P. Kurr, A. Schmidt, R. Schomäcker, I. Voigt, A. Wolf, and R. Warsitz. [alpha]-methylstyrene hydrogenation in a flow-through membrane reactor. *AIChE Journal*, 52(8):2805–2811, 2006. DOI: 10.1002/aic.10893.

C. Ramshaw. Process intensification and green chemistry. *Green Chemistry*, 1:G15 – G17, 1999. DOI: 10.1039/gc990g15.

M. Reif and R. Dittmeyer. Porous, catalytically active ceramic membranes for gas-liquid reactions: A comparison between catalytic diffuser and forced through flow concept. *Catalysis Today*, 82(1-4):3–14, July 2003. DOI: 10.1016/S0920-5861(03)00197-4.

M. G. Reif. *Herstellung, Charakterisierung und Einsatz katalytisch aktiver Membranen für Dreiphasenreaktionen - Katalytischer Diffusor und durchströmter, mikrostrukturierter Membrankatalysator im Vergleich.* PhD thesis, Universität Erlangen-Nürnberg, 2004.

W. Rigby, D. Cowieson, N. Davies, and R. Furneaux. Anodizing process for the production of inorganic microfiltration membranes. *Transactions of the Institute of Metal Finishing*, 68(3):95–98, Aug. 1990.

G. M. Rios, M. P. Belleville, D. Paolucci, and J. Sanchez. Progress in enzymatic membrane reactors - a review. *Journal of Membrane Science*, 242 (1-2):189–196, Oct. 2004. DOI: 10.1016/j.memsci.2003.06.004.

A. A. Rostami, A. S. Mujumdar, and N. Saniei. Flow and heat transfer for gas flowing in microchannels: A review. *Heat and Mass Transfer*, 38(4): 359–367, Apr. 2002. DOI: 10.1007/s002310100247.

A. Rouge, B. Spoetzl, K. Gebauer, R. Schenk, and A. Renken. Microchannel reactors for fast periodic operation: the catalytic dehydration of isopropanol. *Chemical Engineering Science*, 56(4):1419–1427, Feb. 2001. DOI: 10.1016/S0009-2509(00)00366-3.

S. Roy, R. Raju, H. F. Chuang, B. A. Cruden, and M. Meyyappan. Modeling gas flow through microchannels and nanopores. *Journal of Applied Physics*, 93(8):4870–4879, Apr. 2003. DOI: 10.1063/1.1559936.

M.-N. Sabry. Scale effects on fluid flow and heat transfer in microchannels. *IEEE Transactions on Components and Packaging Technologies*, 23(3): 562–567, 2000. DOI: 10.1109/6144.868859.

J. G. Sanchez Marcano and T. T. Tsotsis. *Catalytic membranes and membrane reactors*. Wiley-VCH, Weinheim, 2002. ISBN 978-3-527-30277-2.

G. Saracco and L. Montanaro. Catalytic ceramic filters for flue gas cleaning. 1. Preparation and characterization. *Industrial & Engineering Chemistry Research*, 34(4):1471–1479, 1995. DOI: 10.1021/ie00043a056.

G. Saracco and V. Specchia. Catalytic inorganic-membrane reactors - Present experience and future opportunities. *Catalysis Reviews - Science and Engineering*, 36(2):305–384, 1994. DOI: 10.1080/01614949408013927.

G. Saracco and V. Specchia. Catalytic ceramic filters for flue gas cleaning. 2. Catalytic performance and modeling thereof. *Industrial & Engineering Chemistry Research*, 34(4):1480–1487, Apr. 1995. DOI: 10.1021/ie00043a057.

G. Saracco and V. Specchia. Inorganic-membrane reactors. In A. Cybulski and J. A. Moulijn, editors, *Structured Catalysts and Reactors*, chapter 17, pages 463–500. Marcel Dekker Ltd, 1998. ISBN 978-0-82472-343-9.

G. Saracco, H. W. J. P. Neomagus, G. F. Versteeg, and W. P. M. van Swaaij. High-temperature membrane reactors: Potential and problems. *Chemical Engineering Science*, 54(13-14):1997–2017, July 1999. DOI: 10.1016/S0009-2509(99)00009-3.

A. Schmidt. *A pore-flow-through membrane reactor for selective hydrogenation reactions*. PhD thesis, Technische Universität Berlin, 2007.

A. Schmidt and R. Schomäcker. Partial hydrogenation of sunflower oil in a membrane reactor. *Journal of Molecular Catalysis A: Chemical*, 271(1-2): 192–199, June 2007. DOI: 10.1016/j.molcata.2007.02.052.

A. Schmidt, R. Haidar, and R. Schomäcker. Selectivity of partial hydrogenation reactions performed in a pore-through-flow catalytic membrane reactor. *Catalysis Today*, 104(2-4):305–312, June 2005. DOI: 10.1016/j.cattod.2005.03.073.

A. Schmidt, A. Wolf, R. Warsitz, R. Dittmeyer, D. Urbanczyk, I. Voigt, G. Fischer, and R. Schomäcker. A pore-flow-through membrane reactor for partial hydrogenation of 1,5-cyclooctadiene. *AIChE Journal*, 54(1): 258–268, 2008. DOI: 10.1002/aic.11379.

R. Schomäcker, A. Schmidt, B. Frank, R. Haidar, and A. Seidel-Morgenstern. Membranen als Katalysatorträger. *Chemie Ingenieur Technik*, 77(5):549–558, 2005. DOI: 10.1002/cite.200500043.

O. Schramm and A. Seidel-Morgenstern. Comparing porous and dense membranes for the application in membrane reactors. *Chemical Engineering Science*, 54(10):1447–1453, May 1999. DOI: 10.1016/S0009-2509(99)00062-7.

M. Schuessler, O. Lamla, T. Stefanovski, C. Klein, and D. zur Megede. Autothermal reforming of methanol in an isothermal reactor - Concept and realisation. *Chemical Engineering & Technology*, 24(11):1141–1145, 2001. DOI: 10.1002/1521-4125(200111)24:11<1141::AID-CEAT1141>3.0.CO;2-8.

K. Sirkar, P. Shanbhag, and A. Kovvali. Membrane in a reactor: A functional perspective. *Industrial & Engineering Chemistry Research*, 38(10):3715–3737, 1999. DOI: 10.1021/ie990069j.

A. W. Smith. Porous anodic aluminum oxide membrane. *Journal of the Electrochemical Society*, 120(8):1068–1069, Aug. 1973. DOI: 10.1149/1.2403630.

A. Splinter, J. Sturmann, O. Bartels, and W. Benecke. Micro membrane reactor: A flow-through membrane for gas pre-combustion. *Sensors and Actuators, B: Chemical*, 83(1-3):169–174, Mar. 2002. DOI: 10.1016/S0925-4005(01)01036-X.

P. Stair, C. Marshall, G. Xiong, H. Feng, M. Pellin, J. Elam, L. Curtiss, L. Iton, H. Kung, M. Kung, and H.-H. Wang. Novel, uniform nanostructured catalytic membranes. *Topics in Catalysis*, 39(3):181–186, Oct. 2006. DOI: 10.1007/s11244-006-0055-0.

A. Stankiewicz. Process intensification in in-line monolithic reactor. *Chemical Engineering Science*, 56(2):359–364, Jan. 2001. DOI: 10.1016/S0009-2509(00)00236-0.

A. Stankiewicz. *Re-Engineering the Chemical Processing Plant: Process Intensification*. Number 98 in Chemical Industries. Marcel Dekker, Inc., 1 edition, 2004.

A. Stankiewicz and J. Moulijn. Process intensification: Transforming chemical engineering. *Chemical Engineering Progress*, 96(1):22–34, 2000.

T. Stief, O.-U. Langer, and K. Schubert. Numerische Untersuchungen zur optimalen Wärmeleitfähigkeit in Mikrowärmeübertragerstrukturen. *Chemie Ingenieur Technik*, 70(12):1539–1544, 1998. DOI: 10.1002/cite.330701209.

M. Torres, L. Lopez, J. M. Dominguez, A. Mantilla, G. Ferrat, M. Gutierrez, and M. Maubert. Olefins catalytic oligomerization on new composites of beta-zeolite films supported on [alpha]-Al2O3 membranes. *Chemical Engineering Journal*, 92(1-3):1–6, Apr. 2003. DOI: 10.1016/S1385-8947(02)00011-6.

T. Tsuru, T. Kan-no, T. Yoshioka, and M. Asaeda. A photocatalytic membrane reactor for gas-phase reactions using porous titanium oxide membranes. *Catalysis Today*, 82(1-4):41–48, July 2003. DOI: 10.1016/S0920-5861(03)00200-1.

M. J. Vincent and R. D. Gonzalez. Selective hydrogenation of acetylene through a short contact time reactor. *AIChE Journal*, 48(6):1257–1267, 2002. DOI: 10.1002/aic.690480612.

T. Westermann and T. Melin. Membranreaktoren. *Chemie Ingenieur Technik*, 77(11):1655–1668, 2005. DOI: 10.1002/cite.200500129.

G. Wießmeier and D. Hönicke. Microfabricated components for heterogeneously catalysed reactions. *Journal of Micromechanics and Microengineering*, 6(2):285–289, June 1996. DOI: 10.1088/0960-1317/6/2/012.

J. Wöltinger, K. Drauz, and A. S. Bommarius. The membrane reactor in the fine chemicals industry. *Applied Catalysis, A: General*, 221(1-2):171–185, Nov. 2001. DOI: 10.1016/S0926-860X(01)00812-2.

O. Wörz, K. P. Jäckel, T. Richter, and A. Wolf. Microreactors, a new efficient tool for optimum reactor design. *Chemical Engineering Science*, 56(3): 1029–1033, Feb. 2001. DOI: 10.1016/S0009-2509(00)00318-3.

Y. Xu and B. Platzer. Konzepte zur Simulation katalysierter Reaktionen in Mikroreaktoren mit Mesoporen im Wandbereich. *Chemie Ingenieur Technik*, 73(1-2):27–39, 2001. DOI: 10.1002/1522-2640(200101)73:1/2<27::AID-CITE27>3.0.CO;2-N.

M. Yamada, K. Fugii, H. Haru, and K. Itabashi. Preparation and catalytic properties of special alumina membrane formed by anodic oxidation of aluminum. Technical report, The Light Metal Educational Foundation, Inc. Research Group for Functionalizing of Aluminum and Its Surface Films, 1988.

S. Zalamea, M. Pina, A. Villellas, M. Menéndez, and J. Santamaría. Combustion of volatile organic compounds over mixed-regime catalytic membranes. *Reaction Kinetics and Catalysis Letters*, 67(1):13–19, May 1999. DOI: 10.1007/BF02475821.

J. Zaman and A. Chakma. Inorganic membrane reactors. *Journal of Membrane Science*, 92(1):1–28, June 1994. DOI: 10.1016/0376-7388(94)80010-3.

V. T. Zaspalis, W. van Praag, K. Keizer, J. G. van Ommen, J. R. H. Ross, and A. J. Burggraaf. Reaction of methanol over catalytically active alumina membranes. *Applied Catalysis*, 74(2):205–222, 1991.

B. Zhu, H. Li, and W. Yang. AgBiVMo oxide catalytic membrane for selective oxidation of propane to acrolein. *Catalysis Today*, 82(1-4):91–98, July 2003. DOI: 10.1016/S0920-5861(03)00206-2.

Symbols and Abbreviations

Abbreviations

Abbreviation	Meaning
CMR	Catalytic Membrane Reactor
CSTR	Continuous Stirred Tank Reactor
EDX	Energy Dispersive X-ray analysis
FBR	Fixed Bed Reactor
FTCMR	Flow-Through Catalytic Membrane Reactor
FTIR	Fourier Transform Infrared Spectroscopy
GTL	Gas To Liquid
HC	Hydrocarbons
ICP-OES	Inductively Coupled Plasma Optical Emission Spectroscopy
MF	Microfiltration
NF	Nanofiltration
OCM	Oxidative Coupling of Methane
PFTR	Plug Flow Tubular Reactor
PI	Process intensification
PSD	Pore Size Distribution
PVMR	Pervaporation Membrane Reactor
RTD	Residence Time Distribution
SEM	Scanning Electron Microscopy
UV-vis	Ultraviolet-visible Spectroscopy
VOC	Volatile Organic Compounds
WGS	Water-Gas-Shift
XRD	X-Ray Diffractometry

Mathematical symbols latin

Symbol	Unit	Meaning
$a_{\mathrm{rel},i}$	-	Relative absorption
A	m^2	Cross-sectional pore area
A_{int}	m^2	Internal membrane surface area
A_{wall}	m^2	Cross-sectional wall area allocated to a single pore
A_{mem}	m^2	Accessible membrane area
c	$\mathrm{mol/m}^3$	Concentration
c_p	J/(mol K)	Molar heat capacity
d	m	Pore diameter
D_{ax}	m^2/s	Axial dispersion coefficient
D_{mem}	m	Open membrane diameter
D_{mol}	m^2/s	Molecular diffusion coefficient
E_{A}	J/mol	Arrhenius activation energy
$E(t)$	1/s	Residence time distribution pulse response
$F(t)$	-	Residence time distribution step response
h	$\mathrm{W/(m^2K)}$	Heat transfer coefficient
k_i	variable	Kinetic rate constant of reaction i
k	W/(m K)	Thermal conductivity
L	m	Channel length = membrane thickness
m	-	Number of pore size classes per membrane
n	-	Number of membranes in series
$\dot{n}_i$	mol/s	Molar flow rate in pore size class i
$\dot{n}_{\mathrm{tot}}$	mol/s	Total molar flow rate
M	kg/mol	Molecular weight
N	-	Number of pores
p	Pa	Absolute pressure
p_i	Pa	Partial pressure of component i
P	$\mathrm{mol/(m^2\,s\,Pa)}$	Permeance = pressure normalized flux
Q	$\mathrm{m}^3_{\mathrm{N}}/\mathrm{s}$	Standard volumetric flow rate
$\dot{Q}$	W	Heat transfer rate
R	8.314 J/(mol K)	Ideal gas constant
r	$\mathrm{mol/(kg_{cat}s)}$	Reaction rate
R	-	Dimensionless reaction rate
S	-	Selectivity towards intermediate product
S_{V}	$\mathrm{m}^2/\mathrm{m}^3$	Volume-specific surface
t	s	Time
t_{cat}	μm	Thickness of catalytic layer
T	K	Temperature

Mathematical symbols latin (continued)

Symbol	Unit	Meaning
u	m/s	Axial velocity
$\bar{u}$	m/s	Mean molecular velocity
V	m^3	Volume
x	-	Mole fraction of reactant i
x^*	-	Reduced mole fraction (only HC)
X	-	Conversion
z	m	Axial coordinate
Z	-	Dimensionless axial coordinate $Z = z/L$

Mathematical symbols greek

Symbol	Unit	Meaning
α	°	Contact angle
ϵ	-	Porosity
η	Pa s	Dynamic viscosity
λ	m	Mean free path
σ	N/m	Surface tension
τ	s	Mean residence time
τ_i	s	Mean residence time in pore size class i
θ	-	Normalized residence time
Θ	-	Normalized temperature
ζ_{cat}	-	Catalyst volume fraction

Subscripts

Subscript	Meaning
av	Average (regarding length of channel)
ax	Axial
eff	Effective
i	Pore size class
m	Pore size class with mean pore diameter
mem	Membrane
p	Pore
r	Reactor
ref	Reference (reference pore diameter)
tot	Total

Dimensionless quantities

Definition	Name	Meaning
$Bi = \frac{A_{\text{int}} h L}{(1-\epsilon) A_{\text{mem}} k_{\text{wall}}}$	Biot	Internal heat transfer to heat conduction in solid
$Bi_0 = \frac{h_0 L}{k_{\text{wall}}}$	Biot Feed	External heat transfer to heat conduction in solid
$Bo = \frac{uL}{D_{\text{ax}}}$	Bodenstein	Convective to diffusive transport in axial direction
$Kn = \frac{\lambda}{d}$	Knudsen	Mean free path of gas to pore diameter
$Nu = \frac{A_{\text{int}} h L}{\epsilon A_{\text{mem}} k_{\text{gas}}}$	Nusselt	Internal heat transfer to heat conduction in fluid
$Pe = \frac{\dot{n}_{\text{tot}} c_p L}{\epsilon A_{\text{mem}} k_{\text{gas}}}$	Péclet	Heat convection to heat conduction in fluid
$Pr = \frac{\eta c_p}{M k_{\text{gas}}}$	Prandtl	Kinematic viscosity to thermal diffusivity
$Re = \frac{\rho u d}{\eta}$	Reynolds	Ratio of inertial forces to viscous forces
$St = \frac{h A_{\text{int}}}{\dot{n}_{\text{tot}} c_p}$	Stanton	Internal heat transfer to heat convection
$St_0 = \frac{h_0 (1-\epsilon) A_{\text{mem}}}{\dot{n}_{\text{tot}} c_p}$	Stanton Feed	External heat transfer to heat convection

Curriculum Vitae

Name:	Thomas Westermann
Date of birth:	April 6th, 1978
Place of birth:	Issum, Germany
08.1988–06.1997	School Education:
	Städtisches Gymnasium Kamp-Lintfort, Germany
	Degree: Abitur
10.1998–04.2004	Undergraduate Studies:
	Verfahrenstechnik (Process Engineering)
	Technical University Clausthal (TUC), Germany
09.2000	Degree: Vordiplom
09.2001	ERASMUS exchange program
	Universidad Politécnica de Valencia (UPV), Spain
02.2002	Studienarbeit (mini thesis)
	Study of the acoustic behavior of silencers with two chambers in series
	Departamento de Máquinas y Motores Térmicos, UPV
04.2004	Diplomarbeit (diploma thesis)
	Coprocessing of crude oil vacuum residues with used cooking fat on pilot plant scale
	Clausthaler Umwelttechnik Institut, TUC
04.2004	Degree: Diplom (Dipl.-Ing.)
05.2004–03.2009	Postgraduate Studies:
	Research assistant at
	RWTH Aachen University, Germany
	Aachener Verfahrenstechnik
	Prof. Dr.-Ing. T. Melin
	Chair of Chemical Process Engineering